ISSN ONLINE 2582-2020
ISSN PRINT 0970-3268

The Journal of the Indian Association of Sedimentologists

Volume 36 No. 2 2019

Sediment plume triggered by Elwha Dam demolition in the State of Washington

ISSN Print 0970 – 3268
ISSN online 2582 - 2020

The journal of the Indian Association of Sedimentologists

Managing Editors:

G. M. Bhat
Bashir Ahmad Lone

The Journal of the Indian Association of Sedimentologists (IAS) is both an international open access online journal and print journal and is leader in its field and publishes ground-breaking research from across the spectrum of sedimentology, sedimentary geology, sedimentary geochemistry, experimental and theoretical sediment transport, mass movement fluxes, modern and ancient sedimentary environments, sequence-, cyclo-, chrono- and chemostratigraphy, sediment-biological interaction, palaeosols, diagenesis, stable isotope geochemistry, environmental sedimentology, neotectonics, geohazards, stratigraphy, palynology, sedimentary mineral resources and hydrocarbons, and allied branches of sedimentary - stratigraphic research. It also publishes review articles, editorials, conference reports, tributes, announcements, advertisements, etc. It is currently distributed to universities and research laboratories in India and abroad. Access to the complete electronic journal archive over the past eight years comes free of cost. Subscribers also have the option to buy the printed journal at subsidized cost.

Indian Association of Sedimentologists

TABLE OF CONTENTS

Jour. Indian Association of Sedimentologists, Vol. 36, No. 2 (2019), pp.1-37
ISSN Online 2582 – 2020
ISSN Print 0970 – 3268

Global significance of wind forcing on deflecting sediment plumes at river mouths: Implications for hyperpycnal flows, sediment transport, and provenance

G. Shanmugam
Department of Earth and Environmental Sciences, The University of Texas at Arlington
Arlington, TX 76019, USA
Email: shanshanmugam@aol.com

Abstract: This review, based on sediment plumes at the mouths of 29 rivers worldwide, has revealed that sediment (density) plumes are commonly deflected away from the normal downslope direction in 18 out of 29 cases. These deflected sediment plumes have been documented at the mouths of Brisbane, Congo, Connecticut, Dart, Ebro, Eel, Elwha, Fonissa, Guadalquivir, Krishna-Godavari, Mississippi, Monros, Rio de la Plata, Pearl, Rhone, Tiber, Yellow, and Yangtze rivers. As a consequence, current directions change drastically and sediment distribution occurs on only one side of river mouths. In these cases, sediment transport is diverted by a plethora of 22 oceanographic, meteorological, and other external factors. Empirical data show that wind forcing is the most dominant factor. Other influencing factors are tidal currents, ocean currents, and coastal upwelling. Deflection of sediment plumes defies the conventional use of paleocurrent directions in determining sediment transport and provenance in the ancient sedimentary record. Failure to recognize deflected sediment plumes in the rock record could result in construction of erroneous depositional models with economic implications for reservoir prediction in petroleum exploration.

Keywords: Deflecting sediment plume, Elwha River, Hyperpycnal flows, Paleocurrents, Sediment transport, Tropical cyclone, Wind forcing

Introduction

Density plumes and their various configurations seen on satellite images have been a source of curiosity to the geologic community as well as to the general public. The U.S. National Aeronautics and Space Administration (NASA, 2019) has archived satellite images on density plumes in its online publishing outlet "Earth Observatory" since 1999. NASA has used a variety of satellites, such as Aqua, Terra and Topex/Poseidon. However, there has not been a systematic attempt to compile

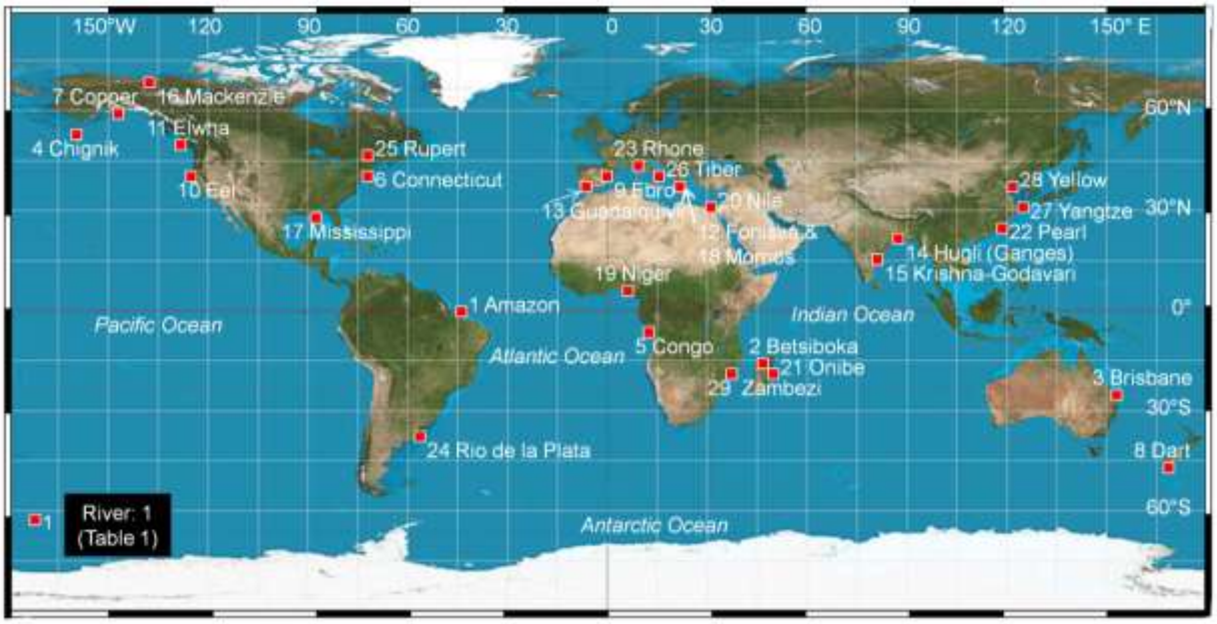

Fig. 1. Location map of 29 rivers used in this study. See Table 1 for details.

variations in natural configurations of density plumes in the world's oceans and lakes (Shanmugam, 2018a, b). This article is an attempt to report common occurrence of density plumes that are deflected at river mouths worldwide due to various external controlling factors (Fig. 1, Table 1).

Serial Number (Fig. 1)	**Case study and Location**	**Coalescing**	**Environment**	**External control**	**Comments**
1	Amazon River, Brazil, Equatorial Atlantic	Deflecting	Open marine	Ocean currents and phytoplankton	Natural sediment plume
2	Betsiboka River, NW Madagascar	Massive	Bay	Tides	Natural sediment plume
3	Brisbane River, Australia, Moreton Bay	Deflecting (Fig. 17)	Bay	Tides	Anthropogenic, due to Port of Brisbane
4	Chignik River, Alaska, Pacific Ocean	Linear	Braid delta in a lagoon, Pacific Ocean	Coarse-grained braid delta (McPherson et al., 1987)	Natural sediment plume
5	Congo (Zaire) River, W. Africa	Deflecting (Fig. 12)	Marine	Tidal currents (Shanmugam, 2003)	Natural sediment plume
6	Connecticut River, New England region, USA	Deflecting (Fig. 5A)	Long Island Sound	Wind forcing (Hurricane Irene, August 21-30, 2011)	Natural sediment plume
7	Copper River, USA, Gulf of Alaska	Coalescing	Braid delta, Marine	Eolian	Natural sediment plume

8	Dart River, South Island, New Zealand, Lake Wakatipu	Deflecting (Fig. 18C)	Braid delta, lacustrine	Tidal? (Heath, 1975)	Natural sediment plume
9	Ebro Delta, Iberian Peninsula, Mediterranean Sea	Deflecting (Fig. 8B)	River-dominated delta	Wind forcing, Cyclonic events and Ocean currents (Arnau et al., 2004)	Natural sediment plume
10	Eel River, California, USA	Deflecting (Fig. 5B)	Shelf	Wind forcing and Shelf currents (Geyer et al., 2000; Imran and Syvitski, 2000)	Natural sediment plume
11	Elwha River, Washington, USA, Strait of Juan de Fuca	Deflecting (Fig. 3C)	Strait	Tidal currents (Cannon, 1978; Thomson et al., 2007), and upwelling wind currents (Foreman et al., 2008)	Anthropogenic plume caused by dam demolition
12	Fonissa River, Greece, Gulf of Corinth	Deflecting (Fig. 11C)	Delta	Bottom currents (Beckers et al., 2016)	Natural sediment plume
13	Guadalquivir River, Southern Spain, Gulf of Cádiz	U-Turn (Deflecting) (Fig. 9C)	River-dominated delta	Surface and slope currents (Peliz et al., 2009)	Natural sediment plume
14	Hugli River, a tributary of the Ganges River, India, Bay of Bengal	Anastomosing	Tide-dominated estuary (Balasubramanian and Ajmal Khan, 2002)	Tidal currents	Natural sediment plume
15	Krishna-Godavari Rivers, India, Bay of Bengal	Deflecting (Fig. 15 & 16)	Estuary	Tidal currents (Shanmugam et al., 2009)' Monsoonal currents (Jagadeesan et al., 2013), and geostrophic currents (Sridhar et al., 2008)	Natural sediment plume
16	Mackenzie River Delta, Canada, Beaufort Sea	Swirly	River-dominated delta	Arctic ocean currents	Natural sediment plume
17	Mississippi River, USA, Gulf of Mexico	Deflating (Fig. 2D & 6B)	River-dominated delta	Wind forcing, **shelf currents** (Walker and Rouse, 1993)	Natural sediment plume
18	Mornos River, Greece, Gulf of Corinth	Deflecting (Fig. 11B)	Delta	Bottom currents (Beckers et al., 2016)	Natural sediment plume
19	Niger River, W. Arica	Linear	Wave-dominated delta	Wind forcing, wave currents	Natural sediment plume
20	Nile Delta, Egypt, Mediterranean Sea	Lobate	River-dominated delta	Wind forcing	Natural sediment plume

21	Onibe River, Eastern Madagascar	Dissipating with sharp front	Marine	Wind forcing, Cyclone (Giovanna, February 7-24, 2012) and ocean currents	Natural sediment plume
22	Pearl River, henna, South China Sea	Deflecting (Fig. 14C)	Marine	Upwelling jets (Chen et al., 2017)	Natural sediment plume
23	Rhone Delta, France, Gulf of Lions, Mediterranean Sea	Deflecting (Fig. 8A)	River-dominated delta	Ocean currents (Arnau et al., 2004)	Natural sediment plume
24	Rio de la Plata Estuary, Argentina and Uruguay, South Atlantic Ocean	Dissipating and deflecting (Fig. 7C)	Marine	Ocean currents (Gonzalez-Silvera et al. 2006; Matano et al., 2010)	Natural sediment plume
25	Rupert Bay, Quebec	Swirly	Bay	Mixing of river and seawater combined with churn of tides	Natural sediment plume
26	Tiber River, Italy, Tyrrhenian Sea	Deflecting (Fig. 10B)	Marine	Wind forcing, Longshore currents (Mikhailova et al., 1998).	Natural sediment plume
27	Yangtze River; China, East China Sea	Deflecting (Fig. 13A)	Tide-dominated estuary	Shelf currents (Liu et al., 2006), Vertical mixing by tides in winter months (Luo et al., 2017)	Natural sediment plume
28	Yellow River, China, Bohai Bay	Horse's tail (Deflecting) (Fig. 2E), Lobate (Fig. 2F)	River-dominated delta	Tidal shear front (Wang et al., 2010)	Natural sediment plume
29	Zambezi River, Central Mozambique, India Ocean	Coalescing lobate, associated with multiple river mouths	Wave-dominated delta	Wind forcing, Longshore currents (Mikhailov et al., 2015)	Natural sediment plume

Table 1. Case studies of 29 rivers, their sediment plumes, and external controls.

Bates (1953) suggested three types of density plumes at river-mouth deltaic environments: 1) hypopycnal plume for floating river water that has lower density than basin water (Fig. 2A); 2) homopycnal plume for mixing river water that has equal density as basin water (Fig. 2B); and 3) hyperpycnal plume for sinking river water that has higher density than basin water (Fig. 2C). Although river-mouth hyperpycnal plumes have received much attention (Bates, 1953), plumes in other environments (e.g., lakes) are equally important.

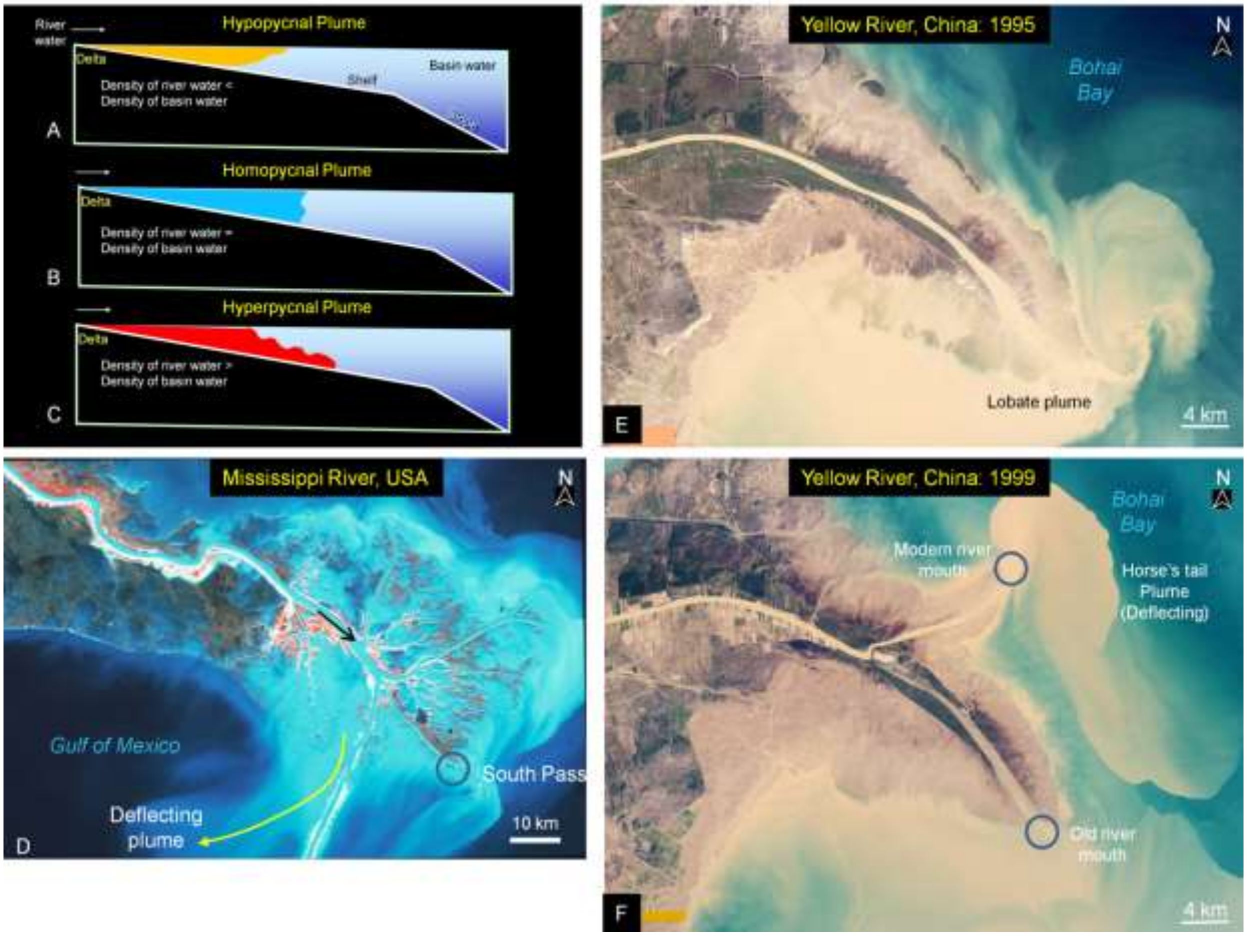

Fig. 2. A. B. C. Schematic diagrams showing three types of density plumes at river mouths in deltaic environments based on concepts of Bates (1953). Figure from Shanmugam (2012) with permission from Elsevier. D. Image of the Mississippi River showing well-developed deflecting plume (yellow arrow). Circle shows river mouth. E. Satellite image of the Yellow River showing well-developed lobate plume at the old river mouth. F. Satellite image of the Yellow River showing horse's tail (deflecting) plume at the modern river mouth that was initiated in 1996. Two circles show old and modern river mouths. From Shanmugam (2018a).

River mouths constitute an important intersectional setting between terrestrial and marine or lacustrine environments. In terms of processes that influence river-mouth sedimentation are waves (Komar, 1976), tides (Klein (1970), gravity-driven downslope processes (Middleton and Hampton, 1973), cyclones (Shanmugam, 2008), tsunamis (Shanmugam, 2008), and shelf-edge related currents (Southard and Stanley, 1976). In addition to longshore currents (Komar, 1976), there are cross-shelf currents (Brink, 2016) and upwelling currents (Milliff et al. 2004; Foreman et al., 2008) that affect the river-mouth and shelf environments.

The primary purpose of this is to document the common occurrence of deflected sediment plumes at river mouths. The second objective is to document the types of external controls involved in deflecting sediment plumes. The third objective is to discuss implications of sediment deflections in understanding paleocurrents, paleogeography, provenance, and reservoir distribution in the ancient sedimentary record. Although the primary dataset for this study is from NASA's satellite images, other published photographic and other images are also used.

Dataset

The term 'sediment plume' is used here for plumes in which the primary cause of density is sediment, although salinity and temperature are important in some cases. A plume is defined a fluid enriched in sediment, ash, biological or chemical matter that enters another fluid. NOAA Fisheries Glossary (2006, p. 42) defines a *River Plume* as "*Turbid freshwater flowing from land and generally in the distal part of a river (mouth) outside the bounds of an estuary or river channel*." Because the original concept of hyperpycnal flows is closely tied to river floods, density plumes at river mouths are considered using the following 29 rivers in this study (Fig. 1):

1) Amazon River, Equatorial Atlantic, Brazil.
2) Betsiboka River, Bombetoka Bay, NW Madagascar.
3) Brisbane River, Moreton Bay, Australia.
4) Chignik River, Alaska, Pacific Ocean, USA.
5) Congo (Zaire) River, South Atlantic Ocean, West Africa.
6) Connecticut River, New England region, USA, Long Island Sound, USA.
7) Copper River, Gulf of Alaska, USA.
8) Dart River, South Island, Lake Wakatipu, New Zealand.
9) Ebro River, Mediterranean Sea, Iberian Peninsula.
10) Eel River, California, Pacific Ocean, USA.
11) Elwha River, Strait of Juan de Fuca, USA.
12) Fonissa River, Gulf of Corinth, Greece.
13) Guadalquivir River, Gulf of Cádiz, Southern Spain.
14) Hugli River (a distributary of the Ganges River), Bay of Bengal, India.

15) Krishna-Godavari Rivers, Bay of Bengal, India.
16) Mackenzie River, Beaufort Sea, Canada.
17) Mississippi River, Gulf of Mexico, USA.
18) Mornos River, Gulf of Corinth, Greece.
19) Niger River, North Atlantic Ocean, West Africa.
20) Nile River Delta, Mediterranean Sea, Egypt.
21) Onibe River, Indian Ocean, Eastern Madagascar.
22) Pearl River, South China Sea, China.
23) Rhone River, Gulf of Lions, Mediterranean Sea, France.
24) Rio de la Plata Estuary, South Atlantic Ocean, Argentina and Uruguay.
25) Rupert River, Quebec, Rupert Bay, Canada.
26) Tiber River, Tyrrhenian Sea, Italy.
27) Yangtze River, East China Sea, China.
28) Yellow River, Bohai Bay, Bohai Sea, China.
29) Zambezi River, Indian Ocean, Central Mozambique.

External control of deflected sediment plumes

External controls are allogenic in nature, which are external to the depositional system, such as uplift, subsidence, climate, eustacy, etc. However, external controls of density plumes are much more variable and include some common depositional processes (e.g., tidal currents, wind forcing, cyclones, etc.). In addition, local physiographic elements, such as seafloor-ridges, channels, etc. could influence the path of plumes. Anthropogenic structures are also known to control deflection of plumes. In this study, the deflection of sediment transport away from the normal downslope transport, by mechanisms, such as longshore currents, is emphasized.

Elwha sediment plume, Strait of Juan de Fuca

The Elwha River is 72 km long in the Olympic Peninsula in the U.S. state of Washington. From its source at Elwha snowfinger in the Olympic Mountains, it flows generally north to the Strait of Juan de Fuca at the U.S.- Canada border (Fig. 3A). A spectacular example of an anthropogenic Elwha sediment plume was triggered by the demolition of Elwha Dam in the Olympic Peninsula, State of Washington (Fig. 3AB). This sediment plume (Fig. 3C)

Fig. 3. Sediment plume triggered by Elwha Dam demolition in the State of Washington (USA). A. Index map showing Elwha Dam (arrow). The 108-foot dam, built in 1910 and demolished in 2012, is located approximately 7.9 km upstream from the river mouth. Credit: U.S. Geological Survey Public Domain map. B. Aerial photograph of the Olympic Peninsula and the Strait of Juan de Fuca. Filled yellow circle = Elwha River mouth. From Duda et al. (2011) with additional labels by G. Shanmugam. C. Elwha sediment plume triggered by the demolition of Elwha Dam in 2012. Red arrow shows easterly deflecting plume, away from the Pacific Ocean. This deflection could be attributed to tidal currents in this estuarine environment. Also, the Strait of Juan de Fuca is subjected to easterly upwelling winds (see Fig. 4). Photo credit: Tom Roorda. Aerial photo was taken on March 30, 2012. D. Aerial photo of Elwha River mouth showing absence of sediment plume in 2019 (compare with Fig. 3C). Aerial photo was taken on February 28, 2019. Photo courtesy of Tom Roorda, Roorda Aerial, Port Angeles, WA.

was the result of sediment released from the world's largest dam demolition (Ritchie et al., 2018). The University of Washington (Seattle, WA) first reported this phenomenal event and its oceanographic and sedimentologic implications in the UW News (Hickey, 2013). According to USGS (2018), this demolition event flushed out 20 million tons of sediment into the Strait of Juan de Fuca. One could classify these Elwha sediment plumes (Fig. 3C) as modern hyperpycnal flows based on visual

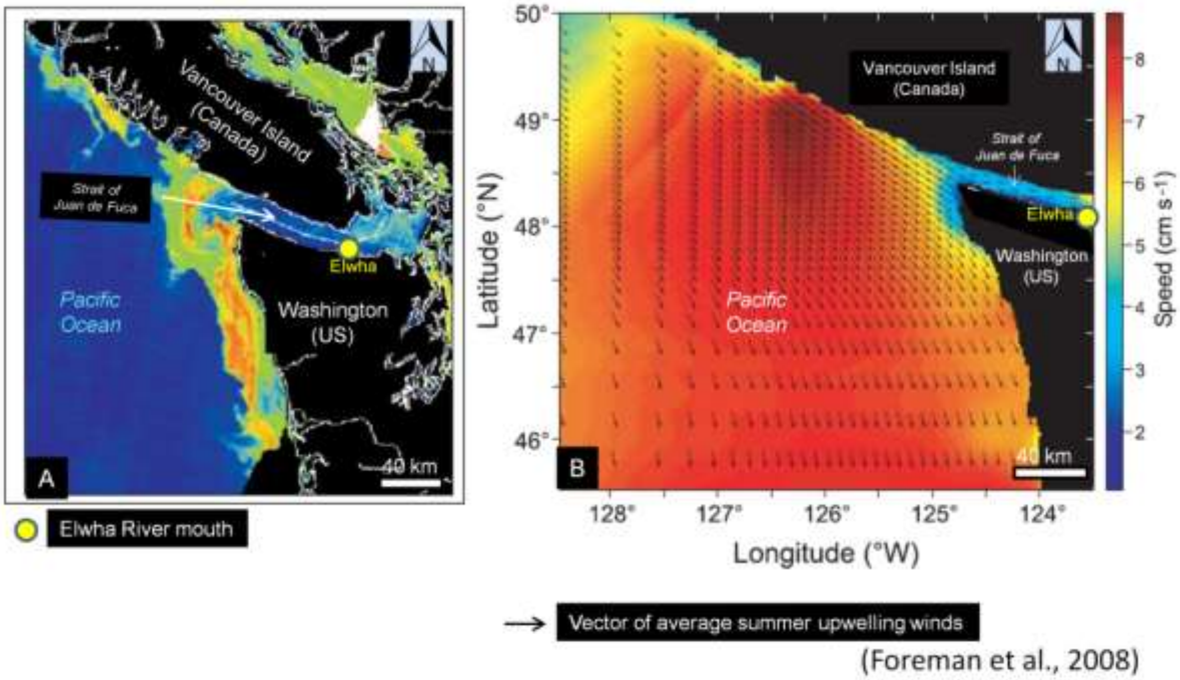

Fig. 4. External control of sediment plumes in the Strait of Juan de Fuca. A. MERIS (MEdium Resolution Imaging Spectrometer) satellite image showing oceanographic setting of the Strait of Juan de Fuca. Filled yellow circle = Elwha River mouth. Satellite image courtesy of the European Space Agency. B. Average summer Upwelling winds, which move easterly in the strait could explain deflecting plumes observed at the Elwha River mouth (see Fig. 3C). According to Foreman et al. (2008), winds reach a maximum speed of 8 m s^{-1} off Vancouver Island with increasing magnitudes eastward in the Strait of Juan de Fuca. Filled yellow circle = Elwha River mouth. Both images are from Foreman et al. (2008) with additional labels by G. Shanmugam.

observation alone. However, without measurements of fluid theology, flow state, and flow density, any classification of these Elwha plumes either as hyperpycnal flows, or as turbidity currents, or as sandy debris flows, is problematic.

Despite the uncertain nature of flow types, an important lesson learned from the Elwha sediment plume is that external factors are critical in redirecting sediment transport. The deflection of Elwha plume to the east (Fig. 3C) could be attributed to tidal currents in this estuarine environment (Cannon, 1978; Thomson et al., 2007; Warrick et al., 2011). Also, summer upwelling winds move easterly into the Strait of Juan de Fuca Fig. 4B). Such summer winds could also explain deflecting sediment plume to the east of the Elwha River mouth (Fig. 3C). The reason is that winds reach a maximum speed of 8 m s^{-1} off Vancouver Island with increasing magnitudes eastward in the Strait of Juan de Fuca (Foreman et al., 2008).

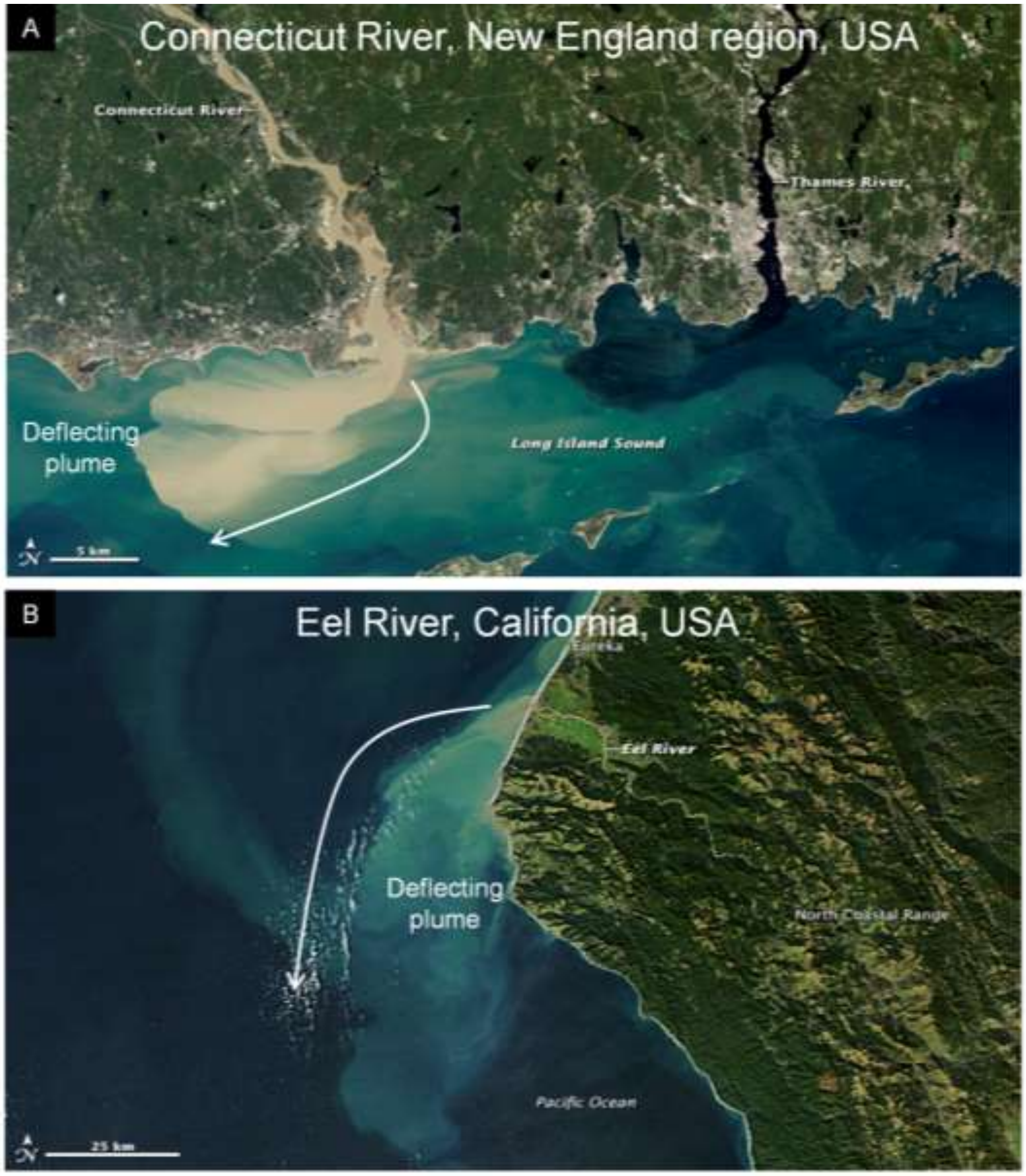

Fig. 5. A. Satellite image showing the Connecticut River entering the Long Island Sound with a deflected lobate plume. NASA Earth Observatory image by Robert Simmon. Image acquired on September 2, 2011. B. Satellite image showing the Eel River in California with a deflected lobate plume. NASA image courtesy Jeff Schmaltz, LANCE MODIS Rapid Response. Caption by Adam Voiland. Image acquired on December 9, 2012.

Connecticut River, New England region, USA, Long Island Sound

The Connecticut River is the longest river in the New England region of the United States. It flows roughly southward for 653 km through four states. It originates at the U.S. border with Quebec, Canada, and empties into Long Island Sound. After Hurricane Irene drenched New England with rainfall in late August 21-30, 2011, the Connecticut River was spewing muddy sediment into Long Island Sound.

Satellite image showed the Connecticut River entering the Long Island Sound deflected lobate plumes (Fig. 5A). The image was acquired on September 2, 2011, two days after the storm dissipated. However, the storm became extratropical cyclone on August 28 and lingered on for a few days. Therefore, the cause of plume deflection could still be the post-hurricane winds associated with the extratropical cyclone.

Eel River, California, USA, Pacific Ocean

The Eel River about 315 km long in northern California where it empties into the Pacific Ocean. A satellite image of the Eel River shows a southerly deflection of sediment plume (Fig. 5B). Imran and Syvitski (2000) studied the Northern California Margin near the mouth of the Eel River and suggested that hyperpycnal flows may be influenced by the along-shelf currents and be deflected northward. Geyer et al. (2000) reported both southerly and northerly winds in the area, and thus the southerly deflection of plume shown in the NASA image (Fig. 5B) can be attributed to wind-forcing.

Mississippi River, USA, Gulf of Mexico

The Mississippi River is the second-largest drainage system on the North

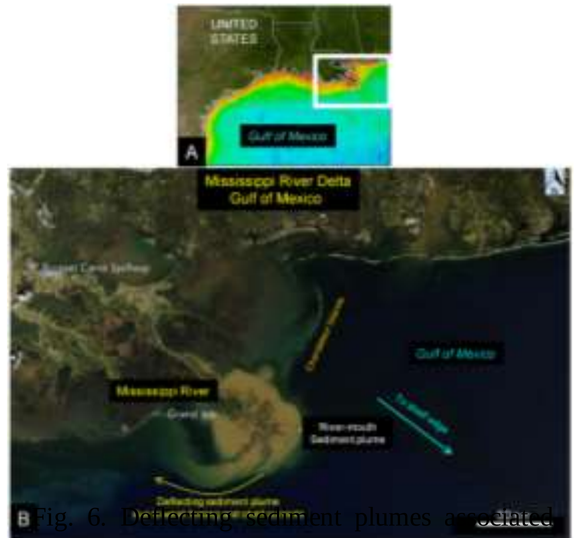

Fig. 6. Deflecting sediment plumes associated with the Mississippi River Delta in the U.S. Gulf of Mexico. A. Index map showing position of the Mississippi River Delta (Box). Image Credit: NASA. B. NASA satellite image of the Mississippi River (USA) showing deflecting (yellow arrow) sediment plumes (i.e., hyperpycnal plumes) away from the shelf edge due to external factors, such as wind forcing and shelf currents (Walker and Rouse, 1993). Image credit: *NASA Earth Observatory image by Joshua Stevens, using MODIS data from LANCE/EOSDIS Rapid Response*. Image acquired on March 4, 2018. Additional labels and interpretation by G. Shanmugam.

American continent, second only to the Hudson Bay drainage system. Its source is Lake Itasca in northern Minnesota and it flows generally south for 2,320 miles (3,730 km)[15] to the Mississippi River Delta in the Gulf of Mexico. A convincing example of deflecting sediment plume is revealed by the Mississippi River Delta in a

Fig. 7. A. Index map of the Río de la Plata Estuary. a Location of the Río de la Plata Estuary (white circle). Image credit: ETOPO1 Global Relief Model, C. Amante and B.W. Eakins, ETOPO1 Arc-Minute Global Relief Model: Procedures, Data Sources and Analysis, NOAA Technical Memorandum NESDIS NGDC-24, March 2009; B. Satellite image showing the Río de la Plata Estuary. C.Satellite image showing the Río de la Plata Estuary with hyperpycnal plumes that tend to deflect towards the Argentinian shelf to the south. Framiňan and Brown (1996) used the term "turbidity front" for this hyperpycnal plume. Note that the entire, 220-km wide, plume gets diluted and dissipated with an irregular front, which fails to advance into the South Atlantic. This dilution of plume is attributed to external controls, such as ocean currents operating on the shelf. The Paraná River, the second longest river in South America after the Amazon, supplies three-quarters of the fresh water that enters the estuary, with the remainder arriving from the Uruguay River. See Fossati and Piedra-Cueva (2013). Figure from Shanmugam (2018a, b).

recent NASA satellite image (Fig. 6). These deflecting (Fig. 6B, yellow arrow) sediment plumes (i.e., hyperpycnal plumes) away from the shelf edge due to external factors, such as wind forcing and shelf currents (Walker et al., 1993) are clear evidence that hyperpycnal flows do not transport sediment across the shelf into deep-water environments.

Río de la Plata estuary, Argentina and Uruguay, South Atlantic Ocean

The Río de la Plata Estuary is located on the east coast of South America, bordering Argentina and Uruguay. It is 280 km long and

220 km wide at its mouth, and its water depth does not exceed 10 m (Fig. 7B). It receives water and sediment from both the Paraná and Uruguay rivers with an annual mean discharge of 22,000 m^3 s^{-1}. Satellite images show dissipating in the north and deflecting in the south plume with an irregular front (Fig. 7C).

The dissipating and deflecting functions of the plume can be attributed to ocean currents that are active at the mouth of the estuary in the South Atlantic ((Gonzalez-Silvera et al. 2006; Matano et al., 2010; Shanmugam, 2018a).

Rhone River, France, Gulf of Lions, Mediterranean Sea

The Rhone River is one of the major rivers of Europe. It originates in the Rhone Glacier in the Swiss Alps and empties into the Mediterranean Sea. In understanding river mouth plume-dispersion patterns in the Mediterranean Sea, Arnau et al. (2004) have utilized satellite imagery products, including various types of thermal and visible images (Advanced Very High Resolution Radiometer [AVHRR], Sea-viewing Wide Field-of-view Sensor [SeaWiFS], and Moderate Resolution Imaging Spectroradiometer [MODIS]). These images were used to describe plume-formation events, their association with coastal oceanography, and their dispersal in the northwestern Mediterranean Sea. At this location, two of the largest Mediterranean rivers (Rhone and Ebro) open into this virtually land-locked sea. Arnau et al. (2004) discussed whether flood events in the study area, as conditioned by riverine,

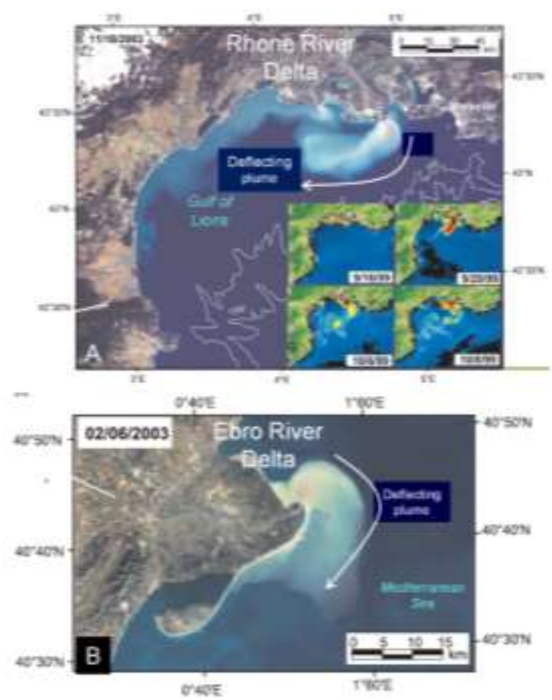

Fig. 8. Rivers flowing into the northern Mediterranean Sea. A. Satellite image showing deflected plume of the Rhone River. B. Satellite image showing deflected plume of the Ebro River. Both images from Arnau et al. (2004) with additional labels by G. Shanmuagm.

oceanographic, and climatic factors. In this study, we are concerned with the spectacular images of the Rhone River and its deflecting plume. (Fig. 8A). Ocean currents are considered an important factor in deflecting these plumes.

Ebro Delta, Iberian Peninsula, Mediterranean Sea

The Ebro River is the second longest river in the Iberian peninsula after the Tagus. Arnau et al. (2004) discussed various aspects of Ebro River. A deflecting plume at the mouth of the Ebro River is striking (Fig. 8B). Cyclonic events and ocean currents are considered an important factor in deflecting these plumes.

Guadalquivir River, Southern Spain, Gulf of Cádiz

The Guadalquivir River is a major river the Iberian Peninsula with its entire length of 657 km in Spain . It empties into the Gulf of Cadiz to the south. The Gulf of Cádiz is located in the northeastern Atlantic Ocean (Fig. 9A). It is enclosed by the southern Iberian and northern Moroccan margins, west of the Gibraltar Strait. Two major rivers, the Guadalquivir and the Guadiana, as well as smaller rivers, like the Odiel, the Tinto, and the Guadalete, reach the ocean here. In terms of ocean currents (Peliz *et al*., 2009), it is one of the most complex oceanographic settings (Fig. 9B). Mimicking the current patterns, sediments that are emptied into the gulf by the Guadalquivir River exhibit a U-Turn shape for the plume (Fig. 9C). In cases like this, one must consider the influence of ocean currents on the dispersal of hyperpycnite sediments. The problem is that how these hyperpycnite sediments would differ from those hyperpycnites unaffected by ocean currents. In other words, do plume configurations (*i.e.*, U-Turn *versus* lobate) matter in the depositional record? No one has addressed this issue.

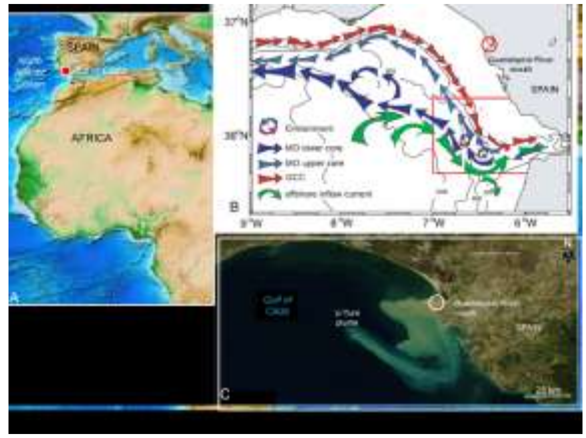

Fig. 9. A. Location map of the Gulf of Cádiz (red filled circle). B. Circulation patterns of ocean currents in the Gulf of Cádiz (Peliz et al. 2009). MO = Mediterranean outflow; GCC = Gulf of Cádiz slope current. C. Satellite image showing sediment plumes with an U-Turn pattern (white arrow). Note that the U-Turn pattern is mimicking the circulation of ocean currents (Fig. 9B). White open circle = Guadalquivir River mouth. NASA. Additional symbols and labels all by G. Shanmugam

Tiber River, Italy, Tyrrhenian Sea

The Tiber River originates in the Apennine Mountains in Emilia-Romagna and flowing 406 kilometers (252 mi)through Tuscany, Umbria and Lazio

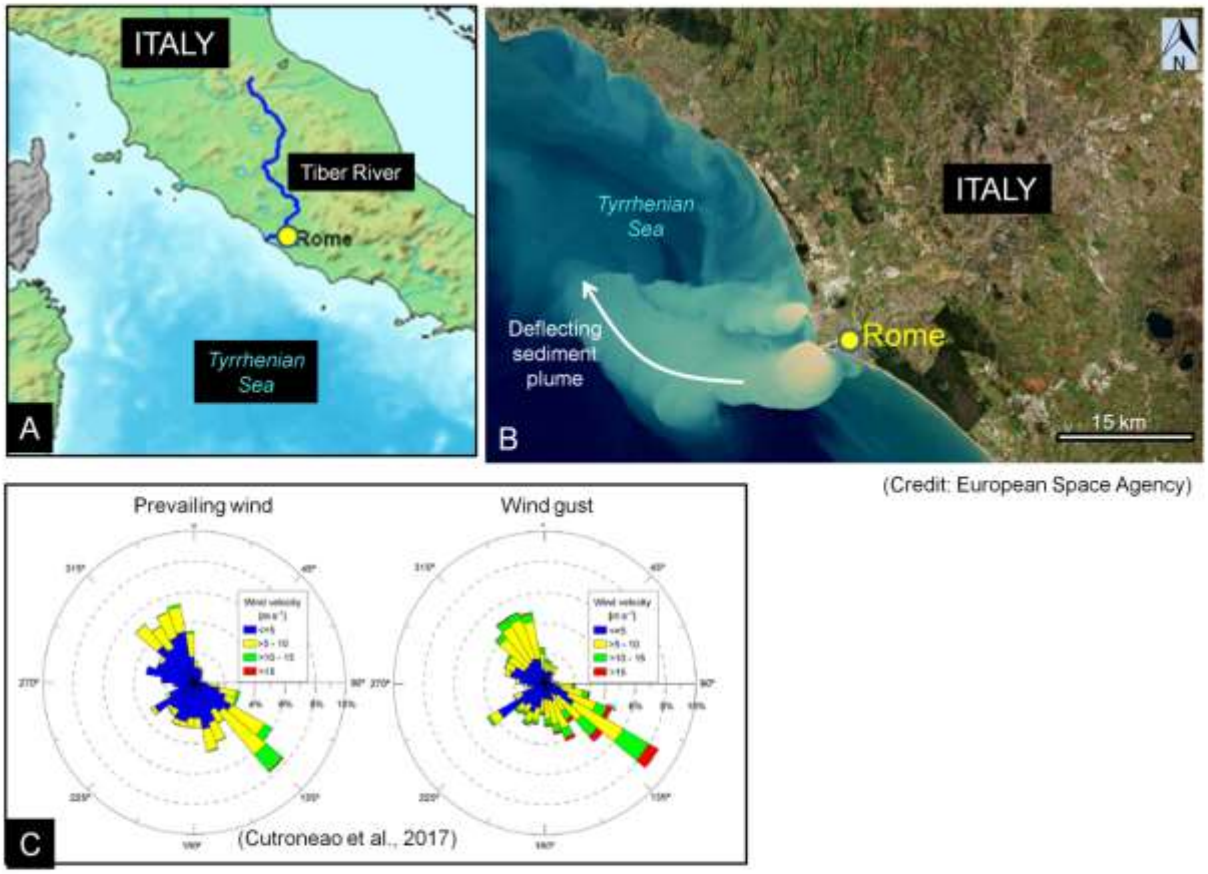

Fig. 10. Deflecting sediment plumes associated with the Tiber River, Tyrrhenian Sea. A. Index map of Tiber River Delta near Rome, Italy. Map modified after Wikipedia. B. The Copernicus Sentinel-2B satellite true-color image showing deflecting sediment plume at the mouth of the Tiber River. Note northwest trending plume (arrow) controlled by northwesterly wind (Manca et al., 2014) and by northwesterly flowing longshore currents at the river mouth (Mikhailova et al., 1998). Credit: Copernicus Sentinel data (2019), processed by ESA, CC BY-SA 3.0 IGO. Image captured on February 5, 2019. C. Rose diagrams showing the velocity and the direction of prevailing wind (left panel) and the maximum velocity and direction of gusts (right panel) in the Giglio Island, which is located northwest of the Tiber delta. Measurements were made every 10 minutes at the weather station of Giglio Porto during the study period 2012-2013. Giglio Porto is located 185 km northwest of Rome. Note that wind is trending from SSE to NNW direction (compare with northwest-trending plume direction in Fig. 10B). From Cutroneao et al. (2017) with permission from Elsevier.

, and empties into the Tyrrhenian Sea, near Rome. A satellite image of sediment plumes associated with the Tiber River in Italy also shows deflected plumes due to northwesterly wind and longshore currents along the Tyrrhenian coast (Fig. 10). The northwest-trending plume (arrow in Fig. 10B) controlled by northwesterly wind (Manca et al., 2014) and by northwesterly flowing longshore currents at the river mouth (Mikhailova et al., 1998). This is a wave-dominated delta (Milli et al., 2013).

Monros and Fonissa Rivers, Greece, Gulf of Corinth

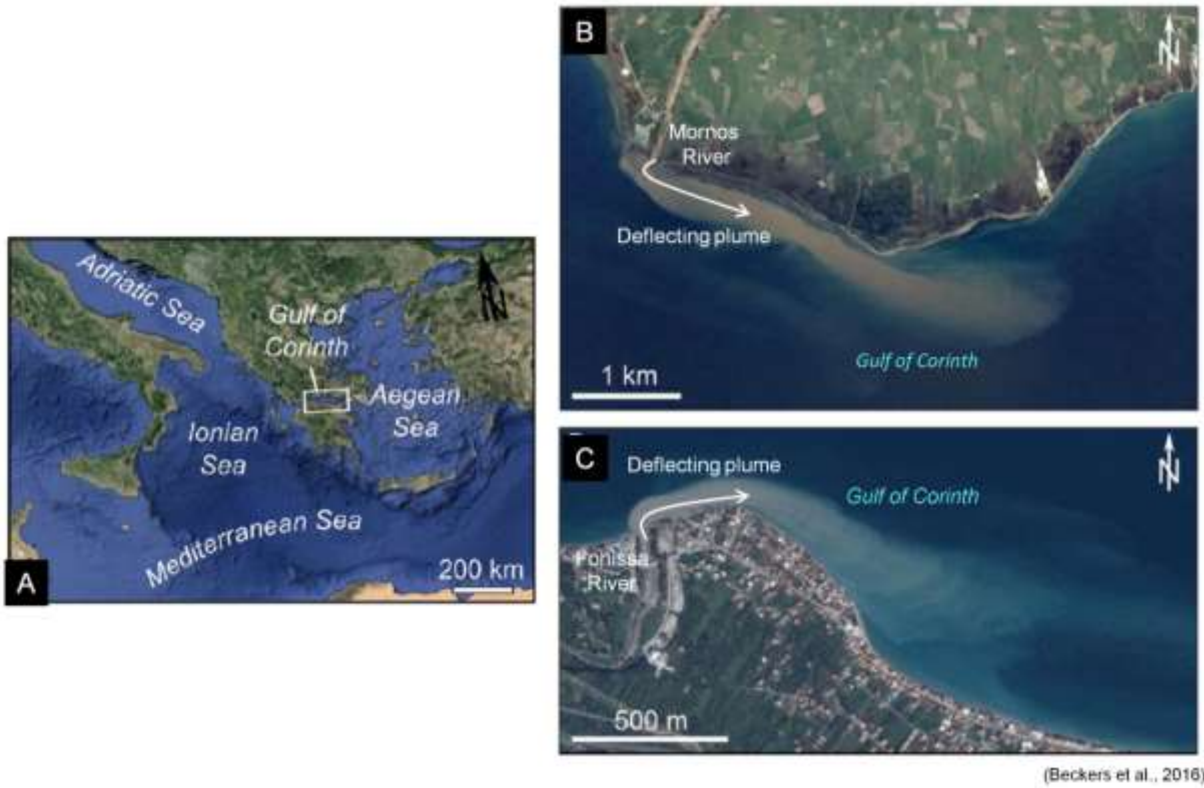

Fig. 11. A. Index map showing Gulf of Corinth, Greece. B. Deflected plume associated with Mornos River. C. (Deflected plume associated with Fonissa River. From Beckers et al. (2016) with additional labels by G. Shanmugam.

The Gulf of Corinth is a 120 km long, up to 30 km wide, and 867 m deep water body connected to the Ionian Sea, in Greece (Fig. 11A). The Gulf is connected at its western tip to the Mediterranean Sea through three shallow sills. Beckers et al. (2016) discussed the influence of bottom currents on deflecting sediment plumes in two rivers, namely the south-flowing Monros River (Fig. 11B) and the north-flowing Fonissa River (Fig. 11C) into the Gulf of Corinth. Twelve cores from0.4 to 2.2 m long were retrieved in 2011 and 2014 with UWITEC® and BENTOS® gravity corers. The cores are located at various depths and various distances from the Rion straits. These cores indicate that drifts are composed of homogenous bioturbated mud in their upper part. This core study is one of the rare cases in which the authors attempt to relate deflection of sediment plumes at river mouths to bottom currents and to link the shallow-water drift deposit to bottom currents. Types of bottom currents, including contour currents, are discussed by Shanmugam (2016).

Congo (Zaire) River, West Africa, Atlantic Ocean

The Congo (Zaire) River is the second longest (4,700 km in length) river in Africa, next to Nile. A Landsat 8 image collected on March 2, 2015 by NASA shows a distinct northerly deflection of sediment plume at the river mouth (Fig. 12). This setting is highly influenced by tidal currents (Shanmugam, 2003). In a numerical modeling of sediment plumes at Congo River mouth, Denamiel et al. (2013) considered tides, wind stress, surface heat flux, and ocean boundary conditions. Hopkins et al. (2013) traced Congo plumes for hundreds of

Fig. 12. Deflected plume associated with Congo (Zaire) River. West Africa. Landsat 8 image was collected on March 2, 2015 by NASA.

kilometers and attributed plumes' deflection to winds and the Angola Current.

Yangtze River; China, East China Sea

The Yangtze River is the longest river (about 6300 km) in Asia. Satellite images show that the Yangtze River generates both hyperpycnal and deflected hypopycnal

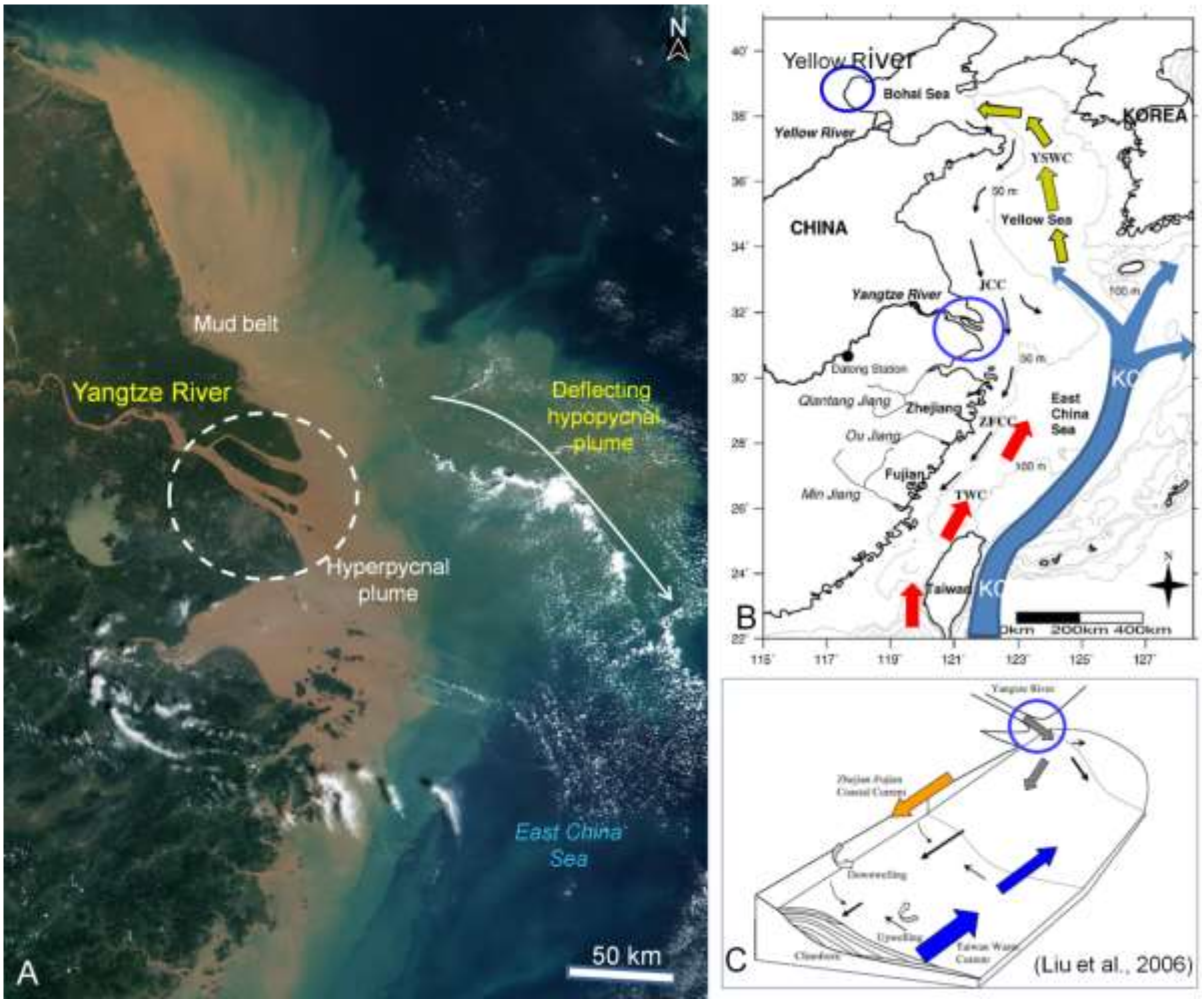

Fig. 13. Data from the Yangtze River, China. A. Satellite image showing the Yangtze River plunging into the East China Sea. Note development of both hyperpycnal plume (yellow color due to high sediment concentration) near the river mouth and hypopycnal plume (blue color due to low sediment concentration) on the seaward side. Note deflected hypopycnal flows that move southward (white arrow), possibly due to modulation by south-flowing shelf currents. In a recent study, Luo et al. (2017) recognized that extended and deflected density plumes (white arrow) tend to develop during winter months, which are absent during the summer months. Note sheet-like mud belt developed along the inner shelf due to contour-following shelf currents. White dashed circle = Yangtze River mouth. NASA. B. Map showing warm Kuroshio Current (KC) in the East China Sea and Yellow Sea. TWC = Taiwan Warm Current; YSWC = Yellow Sea Warm Current; ZFCC = Zhejiang−Fujian Coastal Current; JCC = Jiangsu Coastal Current. Blue circles: Yangtze and Yellow River mouths. From Liu et al. (2006) with additional labels by G. Shanmugam; C. Conceptual model of sedimentary and oceanographic processes affecting the sediment dispersal at both subaqueous river mouth and alongshore deposits associated with the Yangtze River. Blue circle = Yangtze River mouth.From Liu et al. (2006) with additional labels by G. Shanmuagm. Both B and C figures are used with permission from Elsevier.

plumes (Fig. 13A). The Yangtze River mouth is a complex setting in which both ocean currents and tidal currents are affecting sediment dispersal.

Unlike the Yellow River that enters a protected Bohai Bay from major ocean currents, the Yangtze River enters the East China Sea affected by the warm, north-flowing Kuroshio Current (Fig. 13B). As a consequence, muddy sediments brought by the Yangtze River are redistributed and deposited as a mud belt on the inner shelf (Wu *et al*., 2016). This mud belt is evident on the satellite images (Fig. 13A).

Yellow River, China, Bohai Bay

The Yellow River is the second longest river in China, after the Yangtze River, and at the estimated length of 5,464 km. It originates in the Bayan Har Mountains in Qinghai province of Western China, and lows through nine provinces before emptying into the Bohai Bay to the east. It is regarded as the world's largest contributor of fluvial sediment load to the ocean (Yu et al. 2011). Both lobate (Fig. 2E) and deflecting (Fig. 2F) plumes have been documented.

Wang *et al*. (2010) documented the position of the tidal front about 5 km seaward off the Yellow River mouth and explained the tide-induced density flows on the shelf (Wang et al., 2010). The importance of these numerical experiments is that the topography with a strong slope off the Yellow River mouth was a determining factor on the generation of a shear front.

The sedimentologic implication of the shear front is that it limits seaward transport of sediments (Li *et al.*, 2001; Wang *et al.*, 2010). If so, the extent of sediment transport into the deep sea by hyperpycnal flows comes into question. In other words, the entire concept of hyperpycnal flows transporting sediment into the deep sea (Mulder *et al.*, 2002, 2003; Steel *et al.*, 2016; Warrick *et al.*, 2013; Zavala and Arcuri, 2016) is unsupported by the Yellow River, which is considered to be a classic river for hyperpycnal flows.

Pearl River, China, South China Sea

The Pearl River system is China's third-longest river, 2,400 kilometers (1,500 mi), after the Yangtze River and the Yellow River. Satellite sea surface temperature (SST) (°C) in the northern South China Sea on 9 July 2009 (Fig. 14A) and on 24 July 2011 (Fig. 14B) show the trend of sediment plumes associated with the Pearl River. Chen et al. (2017) proposed a model for upwelling water and pathway of the Pearl

River plume in the northern South China Sea (Fig. 14C). There is clear evidence for deflecting flume and that the current direction is parallel to plume direction. Satellite images show that there was a belt of turbid water appearing along an upwelling front near the Chinese coast of Guangdong, a strong jet exists at the upwelling front with a speed as high as 0.8 m s^{-1}, which acts as a pathway for transporting the high-turbidity plume water. The dynamical analysis of Chen et al. (2017) suggests that geostrophic equilibrium dominates in the upwelling front and plume areas, and the baroclinicity of the

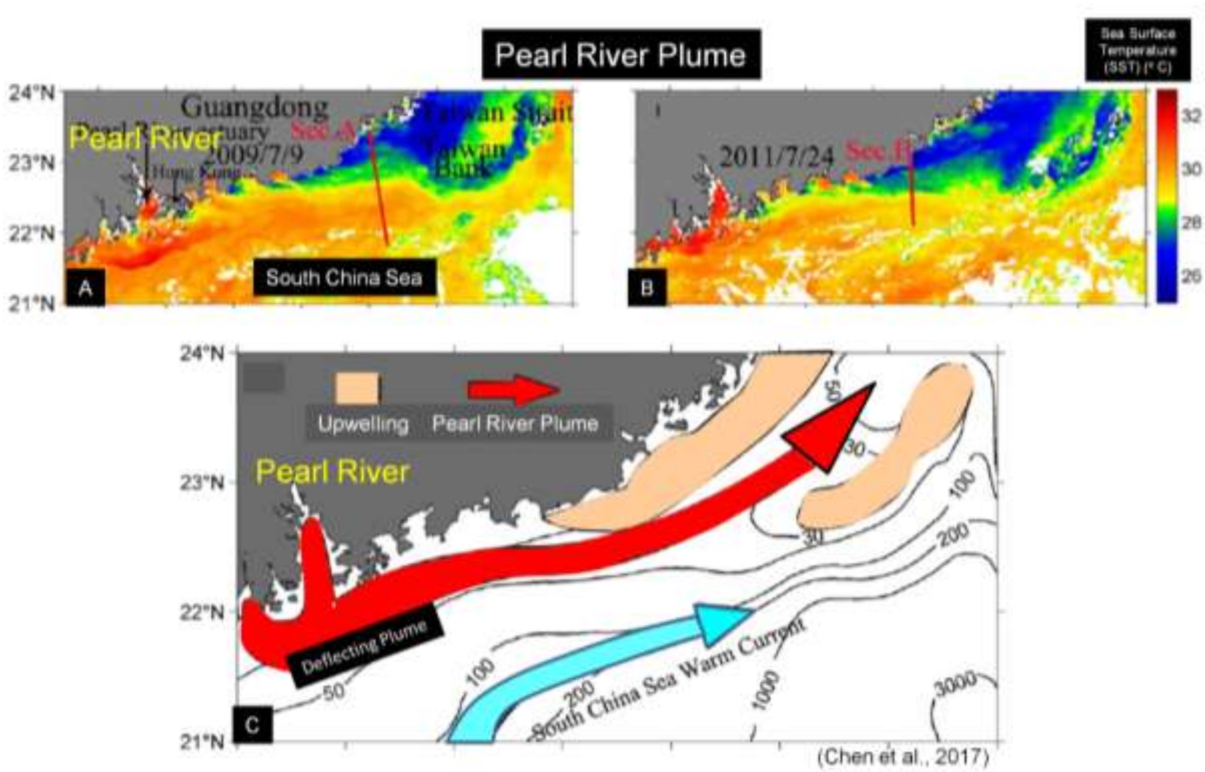

Fig. 14. Data from the Pearl River, China. Satellite sea surface temperature (SST) (°C) in the northern South China Sea on 9 July 2009 (A) and on 24 July 2011 (B) showing the Pearl River mouth and associated plumes. C. Schematics of upwelling water and pathway of the Pearl River plume in the northern South China Sea. Note that the deflecting flume (red arrow) direction is parallel to the South China Sea Warm Current (blue arrow) direction. Compiled from Chen et al. (2017) with additional color labels by G. Shanmugam. Contours show the bathymetry in meters.

and indicate that the turbid water of the Pearl River plume water could be transported to a far-reaching area east of the Taiwan Bank. Numerical modeling results are consistent with the satellite observations, and reveal that upwelling front resulting from the horizontal density gradient is responsible for the generation of the strong jet, which enhances the far-reaching transport of the terrigenous nutrient- rich water of the Pearl River plume.

Model sensitivity analyses also confirm that this jet persists as long as the upwelling front exists, even when the wind subsides and becomes insignificant.

Krishna-Godavari Rivers, India, Bay of Bengal

Both Krishna and Godavari Rivers originate in the Western Ghats and flow across the Deccan Plateau and empty their sediments into the Bay of Bengal. Well-developed deflecting plumes are evident in NASA images of the Godavari River mouth (Fig. 15). The KG Basin is a tide-influenced setting (Shanmugam et al., (2009). In this setting, monsoonal currents play an important role in southerly deflection of sediment plume (Fig. 15B).

Sridhar et al. (2008) studied the influence of seasonal geostrophic currents on sediment plumes in the Krishna-Godavari Basin. Based on the data from Indian remote sensing satellite, Oceansat-1, carries ocean color monitor [OCM] sensor, Sridhar et al. (2008) documented the suspended sediment concentrations [SSC] during 1999-2006 and illustrated a unique plume off Krishna-

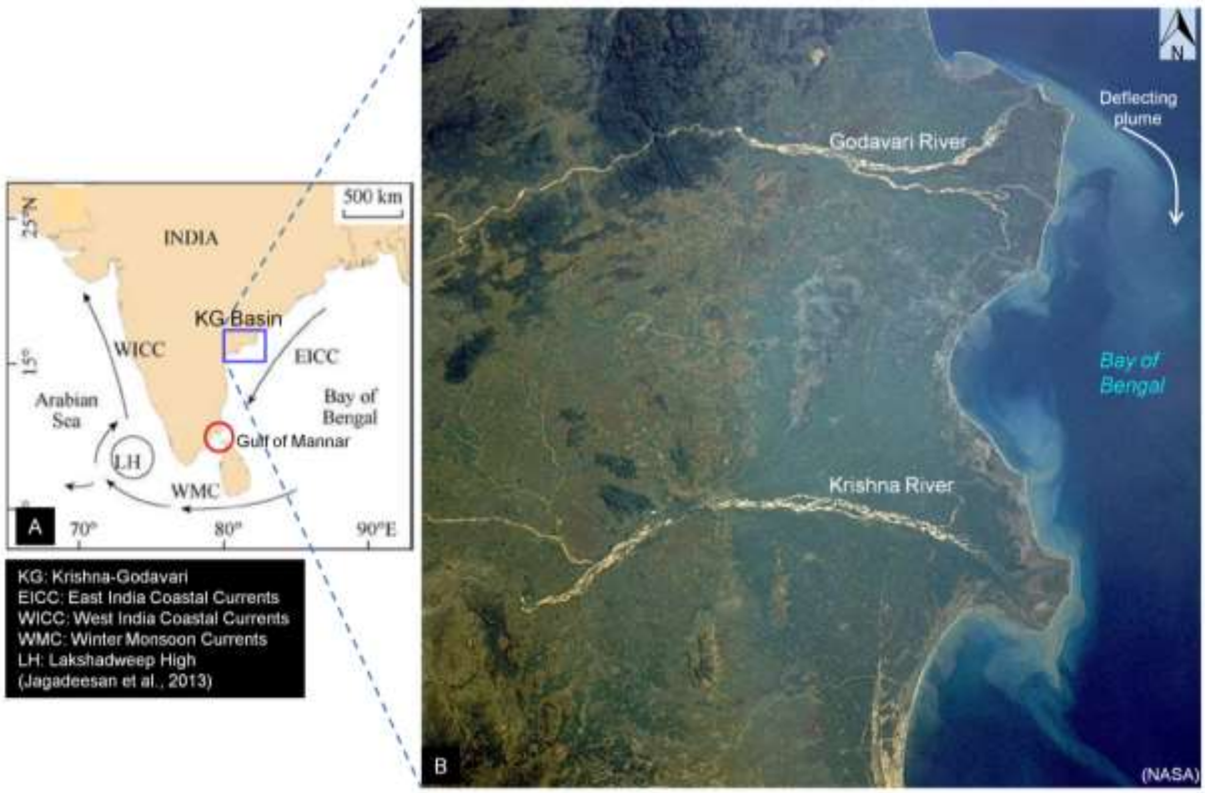

Fig. 15. Data from the Krishna-Godavari Rivers, India. A. Index map of India showing location of the Krishna-Godavari (KG) Basin and northeast monsoonal currents. Modified after Jagadeesan et al. (2013). B. image showing southerly deflecting plume at the mouth of the Godavari River. Image credit: NASA.

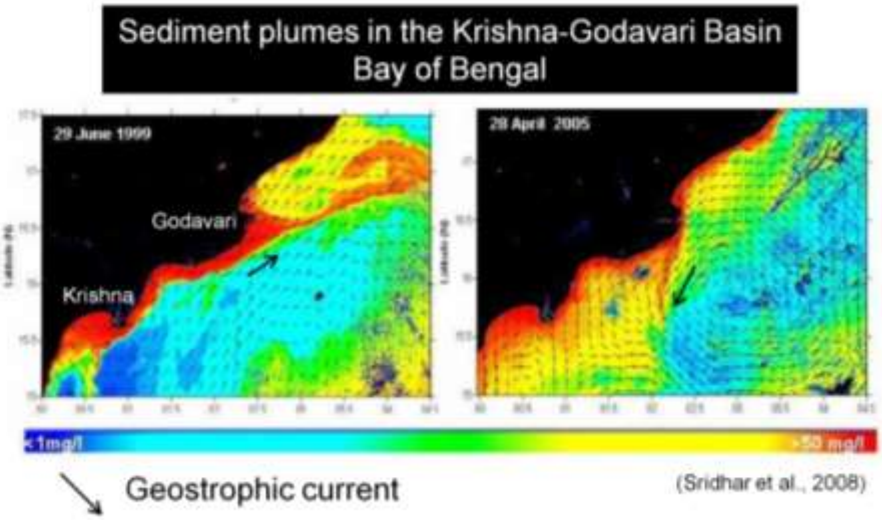

Fig. 16. Sediment plumes and geostrophic currents in the Krishna-Godavari Basin. From Sridhar et al. (2008) with additional labels by G. Shanmugam

Godavari river Basin (Fig. 16). Though high sediment concentration is present all along the east coast of India, the offshoot of the plume is present only at Krishna-Godavari Basin. The presence, extent, orientation and intensity of this plume have both seasonal and inter annual variations. Sridhar et al. (2008) superimposed the geostrophic currents over the OCM observations and documented a convincing influence of geostrophic currents on the deflection of sediment plumes (Fig. 16).

Brisbane River, Australia, Moreton Bay

The Brisbane River is located on the east coast of Australia (Fig. 17A). A storm on May 1, 2015, dropped more than 360 millimeters (14 inches) of rain within about three hours in southeast Queensland. As a result of the rainfall, flash flooding caused distinct river plumes to form along the coastline. On May 3, after the storm had passed, the Operational Land Imager (OLI) on Landsat 8 of NASA acquired a good view of a deflected plume from the Brisbane River entering Moreton Bay (Fig. 17B). In this case, the deflection was caused by the anthropogenic structure of the Port of Brisbane (Fig. 17B).

Fig. 17. Data from the Brisbane River, Australia A. Index map of Australia showing location of city of Brisbane. B. Satellite image showing deflection of the Brisbane River Plume. Note the location of Port o Brisbane and its influence on the plume direction. NASA.

Dart River, South Island, New Zealand, Lake Wakatipu

Fig. 18. Data from the Dart River, New Zealand. A. Index map showing New Zealand and position of Dart braid delta in the South Island of New Zealand. B. Aerial photograph showing Southern Alps and related fluvial setting. Note steep gradient that is typical of braid deltas (McPherson et al., 1987). C. Aerial photograph taken from a helicopter showing a well-developed braid delta with deflecting density plumes (i.e., hyperpycnal plumes) at the mouths of the Dart and Rees Rivers flowing into Lake Wakatipu at Glenorchy near Queenstown, South Island, New Zealand. The Dart River originates from the Dart Glacier in the heart of the Southern Alps to the north (i.e., left of image). Approximate width of braid delta in the image is 1.5 km. Photo by John G. McPherson, Melbourne, Australia

The Dart River originates from the Dart Glacier in the heart of the Southern Alps in the South Island of New Zealand (Fig. 18A). A photograph taken from a helicopter showing a well-developed braid delta with linear density plumes (i.e., hyperpycnal plumes) at the mouths of the Dart and Rees Rivers flowing into Lake Wakatipu at Glenorchy near Queenstown, South Island, New Zealand (Fig. 18C). High gradients of this setting (Fig. 18B) are typical of coarse-grained braid deltas (McPherson et al., 1987). The cause of plume deflection is unclear, although the area is subjected to tidal influence (Heath, 1975).

Global significance of wind forcing on sediment plumes

A review of sediment plumes suggests that there are 22 external controls (Fig. 19). Although there are 22 external factors, wind forcing is the most significant worldwide (Table 1). Wind forcing refers to wind tress exerted by the wind on bodies of water. Wind forcing is the umbrella term for various wind-related phenomena, such as wind waves, longshore currents, cyclonic currents, monsoonal currents, upwelling currents, and seiche. Milliff et al. (2004, their Fig. 5) discussed aspects of wind stress curl and wind stress divergence in illustrating the storm tracks of the Northern Hemisphere (e.g., 35º –50ºN, emanating from western boundaries in both ocean basins), storm tracks in the Southern Hemisphere [e.g., 35º–50ºS, the intertropical convergence zone in the eastern tropical Pacific (0º –10 ºN)], and tropical cyclone regions of the Indian and western Pacific Oceans. Although tropical cyclones occur worldwide, they tend to concentrate on certain key locations, namely the Gulf of Mexico and the Bay of Bengal

Environment	Composition	Provenance	External Control	Type
1. Marine	1. Siliciclastic	1. River flood	1. Wind forcing	1. Simple lobe
2. Lacustrine	2. Calciclastic	2. Common delta	2. Wind waves	2. Horse's tail
3. Estuarine	3. Volcaniclastic	3. Braid delta	3. Longshore curr.	3. Deflecting
4. Lagoon	4. Planktonic	4.Tidal estuary	4. Cyclonic curr.	4. Dissipating
5. Bay	5. Hydrogen sulfide	5. Subglacial	5. Monsoonal curr.	5. U-Turn
6. Reef	6. Gas hydrate	6. Eolian	6. Upwelling curr.	6. Swirly
		7. Volcanic	7. Seiche	7. Cloudy
		8. Planktonic	8. Tidal shear front	8. Massive
		9. Carbonate platform/Reef	9. Tidal current	9.Tidal lobe
		10. Hydrogen sulfide	10. Internal waves and tides	10. Cascading
		11. Gas hydrate	11. Ocean curr.	11. Backwash
			12. Tsunami	12. Meltwater
			13. Braid delta	13. Coalescing irreg.
			14. Volcanism	14. Blanketing
			15. Glacial melt	15. Linear
			16. Coral reef	16. Anastomosing
			17. Fish activity	17. Coalescing lobe
			18. Pockmarks	18. Whitings
			19. Phytoplankton	19. Ring
			20. Hydrogen sulfide	20. Tendril
			21. Gas hydrate	21. Eolian dust
			22. Anthropogenic	22. Feathery
				23. Volcanic ash
				24. Gas hydrate

Fig. 19. Summary diagram showing 22 external controls. Updated after Shanmugam (2018a, b).

Shanmugam (2012) based on data from

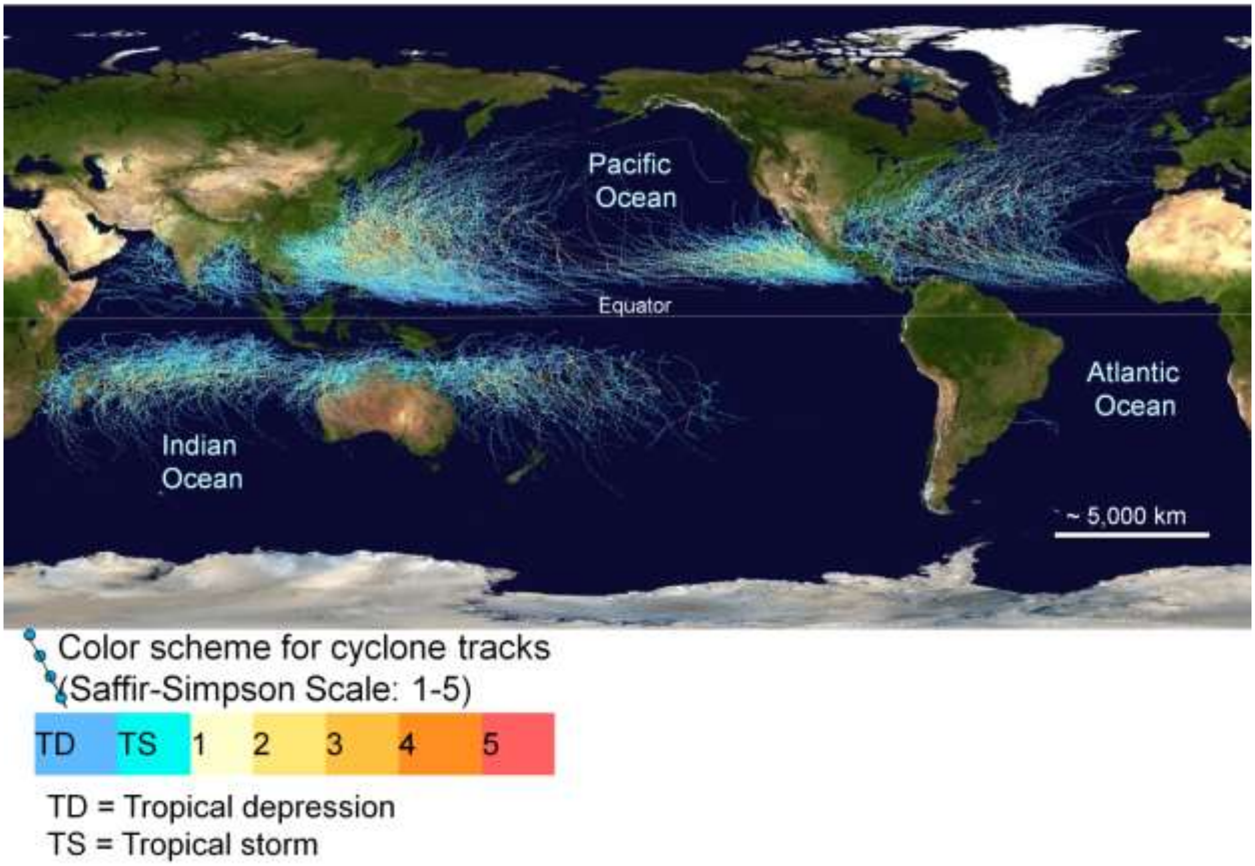

(Fig. 20). In the context of this article, the Hurricane Floyd generated 100-km wide sediment plumes on the U.S. Atlantic Margin (Fig. 21).

Fig. 20. Map showing the tracks of all tropical cyclones, which formed worldwide during the period 1985-2005. The points show the locations of the cyclones at six-hourly intervals. The color scheme represents tropical depression, tropical storm, and the Saffir-Simpson Hurricane Scale of 1-5. Note high concentration of cyclones in the Gulf of Mexico and Bay of Bengal. From NASA.

The Saffir-Simpson Hurricane Scale:

_ Category 1: 120-153 km h^{-1}

_ Category 2: 154-177 km h^{-1}

_ Category 3: 178-209 km h^{-1}

_ Category 4: 210-249 km h^{-1}

_ Category 5: >249 km h^{-1}

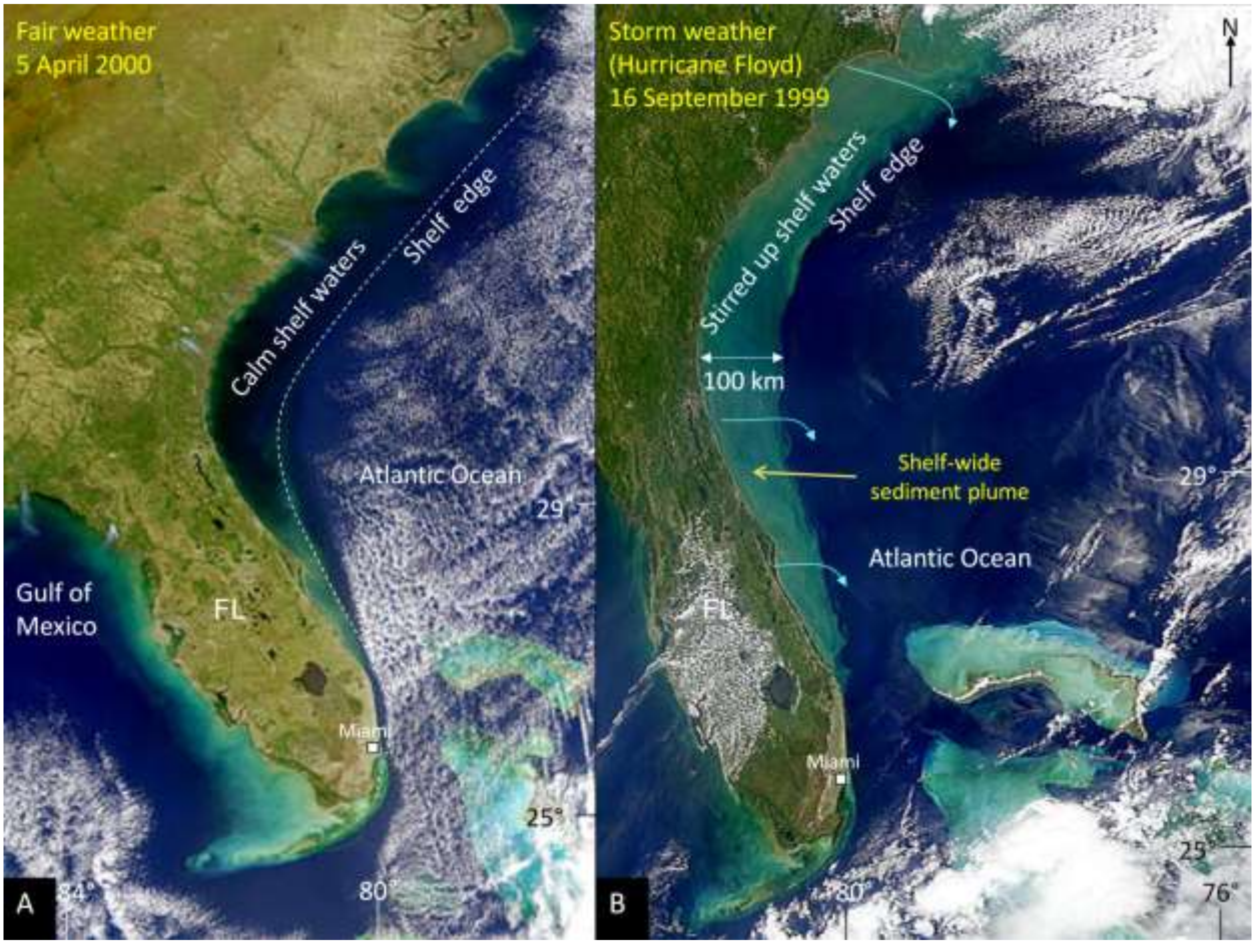

Fig. 21. Shelf-wide sediment plumes generated by Hurricane Floyd of 1999 on the U.S. Atlantic margin. (A) Satellite image showing calm shelf waters (dark blue) on a fair-weather day (April 5, 2000) along the Florida-Georgia-South Carolina-North Carolina coast. Note the influx of suspended sediments and organic matter (yellowish brown) from four rivers into the Atlantic Ocean along the coast. Dashed line indicates approximate position of the shelf edge. (B) Satellite image showing shelf-wide sediment plume (cyan color) as Hurricane Floyd (storm weather) passed over these waters on September 16, 1999. Note that the turbid zone (i.e., sediment plume) is occupying the entire shelf width, which is approximately 100 km (62 mi). Three bent arrows show trends of sediment transport into the deep Atlantic Ocean. FL = Florida. After Shanmugam (2008), reprinted by permission of the American Association of Petroleum Geologists whose permission is required for further use.

An understanding of wind forcing is critical on deflecting sediment plumes in the world's oceans at various depths. This issue can be demonstrated using empirical data from the Gulf of Mexico, which is an ideal location to study wind forcing. For example, the Loop Current in the Gulf of Mexico is a wind-driven current system (Mullins et al., 1980). Velocities in eddies that have detached from the Loop Current have been recorded as high as 200 cm s^{-1} at a depth of 100 m (Cooper et al., 1990). The Loop Current and related eddies pose significant problems for deepwater drilling (Koch et al., 1991). For example, drilling operations in the Green Canyon 166 area were temporarily suspended in August of 1989 because of high-current velocities that reached nearly 150 cm s^{-1} at a depth of 45 m, and 50 cm s^{-1} at a depth of 250 m. These intense bottom currents affect the ability of a drilling rig to hold station over a wellhead (Koch et al., 1991). Current-velocity measurements, bottom photographs, high-resolution seismic records, and GLORIA side-scan sonar records indicate that the Loop Current influences the seafloor at least periodically in the Gulf of Mexico (Pequegnat, 1972). Computed flow velocities of the Loop Current vary from nearly 100 cm s^{-1} at the sea surface to more than 25 s^{-1} at 500 m water depth (Nowlin and Hubert, 1972). This high surface velocity suggests a wind-driven origin for these currents. Flow velocities measured using a current meter reach up to 19 cm s^{-1} at a depth of 3,286 m (Pequegnat, 1972). Kenyon et al. (2002) reported 25 cm s^{-1} current velocity measured 25 m above the seafloor. Such currents are capable of reworking fine-grained sand on the seafloor. Current ripples, composed of sand at a depth of 3,091 m on the seafloor (Pequegnat, 1972), are the clear evidence of deep bottom-current activity in the Gulf of Mexico today (Pequegnat, 1972). Therefore, wind forcing is a powerful agent in deflecting sediment plumes at various depths varying from 10s of meters to 1000s of meters.

Implications for sediment transport

A summary diagram illustrates the differences between two depositional systems, namely the normal sediment transport versus the deflected sediment transport (Fig. 22). In the normal mode, the following conventional concepts are applicable:

- Normal downslope transport from source to sink is common.
- Paleocurrent directions are reliable.
- Depositional settings cover shelf, slope, and basin.
- Wind forcing and tidal currents are common in shelf environment.
- Mass transport and bottom currents are common in slope and basin.
- There is a general increase in grain size from sink to source.
- There is a reliable compositional trend from sink to source.
- There is a reliable inference to provenance.
- At river mouths, lobate plumes (deltas, Fig. 2E) develop with predictable sand distribution. In

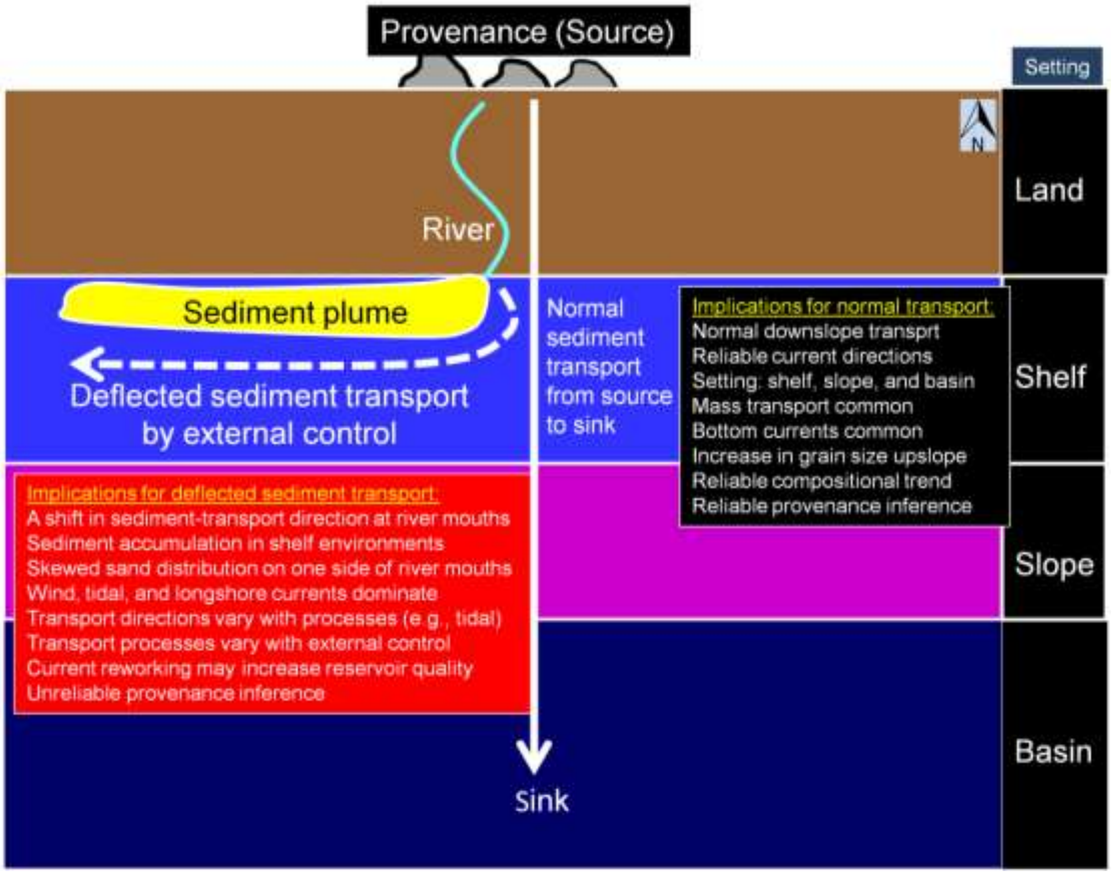

Fig. 22. Summary diagram showing the difference in sediment transport between normal mode and deflected mode with corresponding implications for paleocurrents and provenance. Compare with case study of the Elwha plume in the Strait of Juan de Fuca (Fig. 3C).

basinal environments, submarine fans tend to develop at canyon mouths with predictable sand distribution.

In the deflected mode, conventional concepts do not apply. For example (Fig. 22):

- A major shift occurs in sediment-transport direction occurs at river mouths.
- Sediment accumulation tends to occur in shelf environments, close to the shoreline.
- Sand distribution occurs on only one side of the river mouth.
- Wind, tidal, and longshore currents are dominant.
- Sediment-transport directions could vary with processes (e.g., bidirectional tidal currents).
- Transport processes may vary with external control, such as cyclones, upwelling, etc.

- Current reworking is common and therefore, traction structures are also common in sediment.
- Current reworking may increase reservoir quality.
- Because current directions are complex, it is unreliable to infer provenance accurately.
- Unlike normal sediment transport systems, sand distribution is quite different in deflected systems. For example, deflected sediment may develop tongue-like geometry (Fig. 3C), whereas normal mode develops lobate geometry at river mouths (Fig. 2E). Such a difference is important in petroleum exploration. In the case of the deflected mode, the sand abruptly ends at river mouths, and there is a total absence of sand on the western side of the river mouth in the Elwha River (Fig. 3C).

Provenance

Aspects of sediment provenance have been documented in thematic edited volumes (e.g., Zuffa, 1985; Mazumder, 2016). Principal data used in provenance studies are 1) paleocurrent directions, 2) grain size, 3) sediment composition, 4) diagenetic alteration, 5) stratigraphic framework, 6) depositional setting, and 7) tectonic deformation. Commonly, primary sedimentary structures and related current directions are used in deciphering sediment provenance (Pettijohn, 1975; Potter and Pettijohn, 1977; Zuffa, 1985; Ramos-Vázquez and Armstrong-Altrin, 2019). However, complex current directions associated with deep-water bottom currents pose immense challenges in inferring the primary sediment source (Shanmugam, 2016). This challenge is equally acute in shelf environments where sediment transport is diverted from the normal downslope mode due to external factors, such as wind forcing (Fig. 3C).

Concluding remarks

Empirical data based on satellite images and aerial photographs show that over 50% of the cases studied (i.e., 18 out of 29 cases) have been subjected to varying degrees of deflection of sediment transport, away from the normal course in a downslope direction, by external controls. These external controls include a plethora of oceanographic (e.g., ocean currents, upwelling, etc.), meteorological (e.g., wind forcing, cyclone, etc.), and gravitational (e.g., tides and tidal currents) phenomena. In particular, wind forcing is the most dominant external control of sediment plumes on the shelf and slope environments. The importance of these findings is that our failure to establish external controls on sediment plumes in the ancient sedimentary record could result in erroneous depositional models in terms of sediment transport, paleogeography, and provenance with implications for predicting unrealistic sand distribution and reservoir quality in petroleum exploration of both shallow- and deep-water settings.

Acknowledgements

I thank Prof. G. N. Nayak, CSIR Emeritus Scientist at School of Earth, Ocean and Atmospheric Sciences, Goa University, Goa, India, who is also the President of the Indian Association of Sedimentologists, for a thorough and helpful review of this paper. I also than the second reviewer Dr. Mayla Ramos-Vazquez for helpful review. I am grateful to Dr. John S. Armstrong-Altrin, National Autonomous University of Mexico, for handling my paper. I thank both Managing Editors of the journal, Prof. G. M. Bhat and Dr. Bashir Ahmad Lone, both of Jammu University, India, for their help with editorial matters. I am grateful to NASA (National Aeronautics and Space Administration) for their excellent collection of satellite and other images of density plumes triggered by river floods. I thank Mr. Tom Roorda, Port Angeles, Washington, USA, for giving permission to use aerial photograph of a spectacular sediment plume that was triggered by the demolition of Elwha Dam in 2012 (Fig. 3C) and the Elwha River mouth without sediment plume in 2019 (Fig. 3D). Tom Roorda also provided Meta Data for Elwha plume photographs. I also thank Dr. John G. McPherson, Melbourne, Australia, for proving aerial photographs taken from a helicopter of Dart River braid delta in New Zealand. As always, I am thankful to my wife Jean Shanmugam for her general comments.

References

Arnau, P., Liquete, C. and Canals, M. (2004). River mouth plume events and their dispersal in the northwestern Mediterranean Sea. Oceanography, 17 (3), 23–31

Balasubramanian, T., and Ajmal Khan, S. (2002). Estuaries of India. Environmental information system Centre, Centre of Advanced Study in marine biology, Annamalai University, Parangipettai-608 502, Tamil Nadu, India, sponsored by the Ministry of Environment & forests, government of India, 195. New Delhi: ENVIS Publication Series: 1/2002.

Bates, C.C., (1953). Rational theory of delta formation. AAPG Bulletin, 37, 2119-2162.

Beckers, A., Beck, C., Hubert-Ferrari, A., Tripsanas, E., Crouzet, C., Sakellariou, D., Papatheodorou. G., de Batist, M. (2016). Influence of bottom currents on the sedimentary processes at the western tip of the Gulf of Corinth, Greece. Marine Geology, 378, 312-332.

Brink, K.H. (2016}. Cross-shelf exchange. Annual Review of Marine Science, 8, 59-78.

Cannon, G. A. (1978). Circulation In the Strait of Juan De Fuca: Some Recent Oceanographic Observations. NOAA Technical Report ERL 399-PMEL 29, 55 p.

Chen, Z., Pan, J. Jiang, Y. and Lin, H. (2017). Far-reaching transport of Pearl River plume water by upwelling jet in the northeastern South China Sea. Journal of Marine Systems, 173, 60-69

Cooper, C., Forristall, G.Z., and Joyce, T.M., (1990). Velocity and hydrographic structure of two Gulf of Mexico warm-core rings. Journal of Geophysical Research, 95 (C2), 1663-1679.

Cutroneo, L., Ferretti, G., Scafidi, D., Ardizzone, G. D., Vagge, G., and Capello, M., (2017). Current observations from a looking down vertical V-ADCP: interaction with winds and tide? The case of Giglio Island (Tyrrhenian Sea, Italy). Oceanologia, 59 (2), 139-152.

Denamiel, C., Budgell, W. P., and Toumi, R. (2013). The Congo River plume: Impact of the forcing on the far-field and near-field dynamics, Journal of Geophysical Research: Oceans, 118, 964–989, doi:10.1002/jgrc.20062

Duda, J.J., Warrick, J.A., and Magirl, C.S., (2011). Coastal and Lower Elwha River, Washington, Prior to Dam Removal—History, Status, and Defining Characteristics. In: Duda, J.J., Warrick, J.A., Magirl, C.S., (Eds.), Coastal Habitats of the Elwha River: Biological and Physical Patterns and Processes Prior to Dam Removal. U.S. Geological Sand Survey Scientific Investigations Report 2011-5120. Chapter 1.

Foreman, M. G. G., Callendar, W., MacFadyen, A., Hickey, B. M., Thomson, R. E., and di Lorenzo, E., (2008). Modeling the generation of the Juan de Fuca Eddy. Journal of Geophysical Research: Oceans, 113, C3, CiteID C03006

Fossati, M. Cayocca, F., and Piedra-Cueva. I. (2014). Fine sediment dynamics in the Río de la Plata. Advances in Geosciences, 39, 75–80.

Fossati, M., and Piedra-Cueva. I. (2013). A 3D hydrodynamic numerical model of the Río de la Plata and Montevideos coastal zone. Applied Mathematical Modelling, 37, 1310–1332.

Framiňan, M.B., and Brown. O.B. (1996). Study of the Río de la Plata turbidity front, part I: spatial and temporal distribution. Continental Shelf Research, 16, 1259–1282.

Geyer, W. R., Hill, P., Milligan, T.G., and Traykovski, P. A. (2000). The structure of the Eel River plume during flood. Continental Shelf Research, 20(16), 2067-2093

Gonzalez-Silvera, A., Santamaria-del-Angel, E., and Millán-Núňez, R. (2006). Spatial and temporal variability of the Brazil–Malvinas Confluence and the La Plata Plume as seen by SeaWiFS and AVHRR imagery. Journal of Geophysical Research, 111, C06010.

Heath, R. A. (1975) Surface oscillations of lake Wakatipu, New Zealand, New Zealand Journal of Marine and Freshwater Research, 9:2, 223-238, DOI: 10.1080/00288330.1975.9515560

Hickey, H., (2013). Tracking sediments' fate in largest-ever dam removal. UW News (U. Washington), Seattle, WA, March 7, 2013. With technical information on sediment plumes from two UW oceanographers: Charles Nittrouer and Andrea Ogston. <http://www.washington.edu/news/2013/03/07/tracking-sediments-fate-in-largest-ever-dam-removal/> Accessed March 3, 2019

Hopkins, J., Lucas, M., Dufau, C., Sutton, M., and Lauret, O., (2013). Detection and variability of the Congo River plume from satellite derived sea surface temperature, salinity, ocean colour and sea level. EGU General Assembly 2013, held 7-12 April, 2013 in Vienna, Austria, id. EGU2013-3135

Imran, J., and J. Syvitski. (2000). Impact of extreme river events on coastal oceans. Oceanography, 13 (3), 85–92.

Jagadeesan, L., Jyothibabu, R., Anjusha, A., Mohan, A.P., Madhu, N.V., Muraleedharan, K.R., and Sudheesh, K., (2013). Ocean currents structuring the mesozooplankton in the Gulf of Mannar and the Palk Bay, southeast coast of India. Progress in oceanography, *110*, 27-48.

Kenyon, N.H., Akhmetzhanov, A.M., and Twichell, D.C., 2002. Sand wave fields beneath the Loop Current, Gulf of Mexico: reworking of fan sands. Marine Geology, 192, 297-307.

Klein, G. D. (1970). Depositional and dispersal dynamics of intertidal sand bars. Jour. Sedimentary Petrology, 40, 1095-1127.

Koch, S.P., Barker, J.W., Vermersch, J.A., 1991. The Gulf of Mexico Loop Current and deepwater drilling. Journal of Petroleum Technology, 43, 1046-1050 and 1118-1119.

Komar, P. D., 1976, Beach processes and sedimentation: Englewood Cliffs, New Jersey, Prentice-Hall, Inc., 429 p.

Li, G.X., Tang, Z.S., Yue, S.H., Zhuang, K.L., and Wei, H.L., (2001). Sedimentation in the shear front off the Yellow River mouth. *Continental Shelf Research*, 21 (6–7), 607–625.

Liu, J.P., Li, A.C. Xu, K.H. Velozzi, D.M. Yang, Z.S. Milliman, J.D. and DeMaster. D.J. (2006). Sedimentary features of the Yangtze River-derived along-shelf clinoform deposit in the East China Sea. Continental Shelf Research, 26, 2141–2156.

Luo, Z., Zhu, J. Wu, H. and Li. X. (2017). Dynamics of the sediment plume over the Yangtze Bank in the Yellow and East China Seas. Journal of Geophysical Research: Oceans 122: 10,073–10,090 https://doi.org/10.1002/2017JC013215.

Manca, F., Capelli, G., La Vigna, F., Mazza, R., and Pascarella, A., (2014). Wind-induced salt-wedge intrusion in the Tiber River mouth (Rome-Central Italy). Environmental Earth Sciences, 72 (4), 1083-1095

Matano, R.P., Palma, E.D. and Piola. A.R. (2010). The influence of the Brazil and Malvinas Currents on the southwestern Atlantic shelf circulation. Ocean Science, 6, 983–995.

Mazumder, R. (Ed.), (2016). Sediment Provenance: Influences on Compositional Change from Source to Sink. Elsevier, 614 p.

McPherson, J.G., Shanmugam, G. and Moiola. R.J. (1987). Fan-deltas and braid deltas: Varieties of coarse-grained deltas. GSA Bulletin, 99, 331–340.

Middleton, G.V., and Hampton, M.A., 1973. Sediment gravity flows: mechanics of flow and deposition. In: Middleton, G.V., Bouma, A.H. (Eds.), Turbidites and Deep-Water Sedimentation. SEPM, Anaheim, CA, pp. 1-38. SEPM Pacific section Short Course.

Mikhailova, M. V., Bellotti, P., Valeri, P., and Tortora, P., (1998). The Tiber River Delta and the Hydrological and Morphological Features of Its Formation. Water Resources. Vol. 25, Mo. 5, 572-582. Translated from Vodnye Resursy, 25 (5), 620-630.

Mikhailov, V.N., Kravtsova, V.I. and Isupova. M.V. (2015). Impact of reservoirs on the hydrological regime and morphology of the lower reaches and delta of the Zambezi River (Mozambique). Water Resources, 42 (2), 170–185.

Milli, S., et al. (2013). The transition from wave-dominated estuary to wave-dominated delta: The Late Quaternary stratigraphic architecture of Tiber River deltaic succession (Italy). Sedimentary Geology, 284, 159-180.

Milliff, R. F., Morzel, J., Chelton, D. B., and Freilich, M. H., (2004). Wind Stress Curl and Wind Stress Divergence Biases from Rain Effects on QSCAT Surface Wind Retrievals. Journal of Atmospheric and Oceanic Technology, 21, 8, 1216-1231.

Mulder, T., Migeon, S., Savoye, B. and Faugères, J.-C. (2002). Reply to discussion by Shanmugam on Mulder et al. (2001, Geo-Marine Letters, 21, 86–93) Inversely graded turbidite sequences in the deep Mediterranean. A record of deposits from flood-generated turbidity currents? Geo-Marine Letters, 22, 112–120.

Mulder, T., Syvitski, J.M., Migeon, S., Faugeres, J.-C., and Savoye, B., (2003). Marine hyperpycnal flows: initiation, behavior and related deposits: a review. Marine and Petroleum Geology, 20, 861-882.

Mullins, H.T., Neumann, A.C., Wilber, R.J., Hine, A.C., and Chinburg, S.J., 1980. Carbonate sediment drifts in the northern Straits of Florida. AAPG Bulletin, 64, 1701-1717.

NASA (National Aeronautics and Space Administration), (2019). Earth Observatory. <https://earthobservatory.nasa.gov/.> Accessed January 30, 2018.

NOAA (National Oceanic and Atmospheric Administration) Fisheries Glossary, (2006). River plume. NOAA Technical Memorandum NMFS-F/SPO-69. Revised Edition, U.S. Department of Commerce, 71 p.

Nowlin Jr., W.D., and Hubert, J.M., 1972. Contrasting summer circulation patterns for the eastern Gulf. In: Capurro, L.R.A., Reid, J.L. (Eds.), Contributions on the Physical Oceanography of the Gulf of Mexico, Texas A&M University Oceanographic Studies 2. Gulf Publishing, Houston, TX, pp. 119-137.

Peliz, A., Marchchesiello, P., Santos, A.M.P., Dubert, J., A. Teles-Machado, A. and Marta-Almeida. M. (2009). Surface circulation in the Gulf of Cadiz: 2. Inflowoutflow coupling and the Gulf of Cadiz slope current. Journal of Geophysical Research: Oceans, 114, C03011.

Pequegnat, W.E., (1972). A deep bottom-current on the Mississippi Cone. In: Capurro, L.R.A., Reid, J.L. (Eds.), Contribution on the Physical Oceanography of the Gulf of Mexico, Texas A&M University Oceanographic Studies 2. Gulf Publishing, Houston, TX, pp. 65-87.

Pettijohn, F.J., (1975). Sedimentary Rocks, third ed. Harper & Row, Publishers, New York, 628 p.

Potter, P.E., and Pettijohn, F.J., (1977). Paleocurrents and Basin Analysis. Springer, 425 p.

Ramos-Vázquez, M.A., Armstrong-Altrin, J.S. (2019). Sediment chemistry and detrital zircon record in the Bosque and Paseo del Mar coastal areas from the southwestern Gulf of Mexico. Marine and Petroleum Geology, 110, 650-675.

Ritchie, A.C., Warrick, J.A., East, A., et al. (2018). Morphodynamic evolution following sediment release from the world's largest dam removal. Scientific Reports | *(2018) 8:13279* + DOI:10.1038/s41598-018-30817-8 1, 13 p.

Shanmugam, G. (2003). Deep-marine tidal bottom currents and their reworked sands in modern and ancient submarine canyons. Marine and Petroleum Geology, 20, 471–491

Shanmugam, G., (2008).The constructive functions of tropical cyclones and tsunamis on deepwater sand deposition during sea level highstand: implications for petroleum exploration. *AAPG Bulletin*, 92, 443-471

Shanmugam, G., (2012). New Perspectives on Deep-water Sandstones, Origin, Recognition, Initiation, and Reservoir Quality. Handbook of Petroleum Exploration and Production, vol. 9. Elsevier, Amsterdam, 524 p.

Shanmugam, G., (2016). The contourite problem. In: Mazumder, R. (Ed.), Sediment Provenance. Elsevier, pp. 183–254.

Shanmugam, G. (2018a). The hyperpycnite problem. Journal of Palaeogeography, 7 (3), 197-238.

Shanmugam, G.. (2018b). A global satellite survey of density plumes at river mouths and at other environments: Plume configurations, external controls, and implications for deep-water sedimentation. Petroleum Exploration and development, 45 (4), 640-661.

Shanmugam, G., Shrivastava, S. K., and Das, B. (2009). Sandy debrites and tidalites of Pliocene reservoir sands in upper-slopecanyon environments, offshore Krishna- Godavari Basin (India), implications. Journal of Sedimentary Research, 79, 736-756.

Southard, J.B., and Stanley, D.J., (1976}. Shelf-break processes and sedimentation. In: Stanley, D.J., Swift, J.P. (Eds.), Marine Sediment Transport and Environmental Management. John Wiley & Sons, New York, pp. 351-377.

Sridhar, P. N., Ali, M. M., Vethamony, P., Babu, M. T., Ramana, V., and Jayakumar, S. (2008). Seasonal occurrence of unique sediment plume in the Bay of Bengal. Eos Transactions American Geophysical Union, 89(3), 22-23.

Steel, E., Simms, A.R., Warrick, J., and Yokoyama, Y., (2016). Highstand shelf fans: The role of buoyancy reversal in the deposition of a new type of shelf sand body. *GSA Bulletin*, 128, 1717–1724.

Thomson, R. E., MiháLy, S. F.,and Kulikov, E. A ., (2007). Estuarine versus transient flow regimes in Juan de Fuca Strait. Journal of Geophysical Research: Oceans, 112, C9, CiteID C09022

USGS (U.S. Geological Survey) (2018). Moving Mountains: Elwha River Still Changing Five Years After World’s Largest Dam-Removal Project: More than 20 million tons of sediment flushed to the sea. USGS News. September 5, 2018.

<https://www.usgs.gov/news/moving-mountains-elwha-river-still-changing-five-years-after-world-s-largest-dam-removal> Accessed March 3, 2019.

Walker, N.D. and Rouse, Jr. L.J. (1993). Satellite assessment of Mississippi River discharge plume variability. OCS Study MMS 93–0044. U.S. Dept. of the Interior, Minerals Management Service, Gulf of Mexico OCS Regional Office, New Orleans, La. 50 p.

Wang, H., Bi, N. Wang, Y. Saito, Y. and Yang. Z. (2010). Tide-modulated hyperpycnal flows off the Huanghe (Yellow River) Mouth, China. Earth Surface Processes and Landforms, 35 (11), 1315–1329.

Warrick, J. A., Stevens, A. W. Miller, J. M., and Gelfenbaum, G., (2011). Coastal Processes of the Elwha River Delta. In: Duda, J.J., Warrick, J.A., Magirl, C.S., (Eds.), Coastal Habitats of the Elwha River: Biological and Physical Patterns and Processes Prior to Dam Removal. Chapter: 1. U.S. Geological Survey Scientific Investigations Report 2011-5120. Chapter 5.

Warrick, J.A., Simms, A.R., Ritchie, A., Steel, E., Dartnell, P., Conrad, J.E., and Finlayson, D.P., (2013). Hyperpycnal plumederived fans in the Santa Barbara Channel, California. *Geophysical Research Letters*, 40, 2081–2086.

Wu, J., Ren, J., Liu, H., Qiu, C., Cui, Y., and Zhang, Q., (2016). Trapping and escaping processes of Yangtze River-derived sediments to the East China Sea. In: Clift, P.D., Harff, J., Wu, J., Qui, Y., (Eds.), *River-Dominated Shelf Sediments of East Asian Seas*. *Geological Society, London, Special Publications*, 429, 153–169.

Yu, J., Fu, Y. Li, Y., Han, G., Wang, Y., Zhou, D., Sun, W., Gao, Y., and Meixner, F.X. 2011. Effects of water discharge and sediment load on evolution of modern Yellow River Delta, China, over the period from 1976 to 2009. Biogeosciences, 8 (9), 2427–2435.

Zavala, C. and Arcuri, M. (2016). Intrabasinal and extrabasinal turbidites: Origin and distinctive characteristics. Sedimentary Geology, 337, 36–54.

Zuffa, G.G. (Ed.), (1985). Provenance of Arenites. D. Reidel Publishing Company, Dordrecht, 408 p.

Jour. Indian Association of Sedimentologists, Vol. 36, No. 2 (2019), pp.38-63
ISSN Online 2582 – 2020
ISSN Print 0970 – 3268

Gaps in studies and future perspective of research on the Lameta Formation and Bagh Group, central and western India

Ashok K. Srivastava, Neelam K. Kandwal
Department of Geology, SGB Amravati University, Amravati- 444602, India
ashokamt2000@hotmail.com

Abstract: Both Lameta Formation and Bagh Group of central and western India manifest many geological evidences which are helpful for reconstructions of paleoclimate, paleogeography and biotic community including dinosaur's inhabitation and survival. These stratigraphic units are under investigation from last 5-6 decades for their lithological settings and environments of deposition, dinosaurian remains, fossil biota, marine incursions etc. In the present work, an attempt has been made to synthesize the work done on various aspects of the Lameta and Bagh sediments. Based on the same, gaps in the studies have been identified which need the attention of researches to elucidate existing controversies about environment of deposition, palaeogeographic limits, marine incursion, dinosaur inhabitation for the Lametas and, to establish precise stratigraphic set up, time connotation of floral and faunal contents including their palaeoclimatic and palaeoecological implications for the Bagh Group of rocks.

Key words: Lameta Formation, Bagh Group, Dinosaur, Maastrichtian, Cenomanian-Coniacian, Palaeoecology.

Introduction

The Lameta Formation and the Bagh Group of rocks are significant stratigraphic units as they preserve multiple evidences to reconstruct palaeoecological, palaeobiological and palaeogeographical conditions during Upper Cretaceous period. Both these stratigraphic units are addressed for their sedimentological and palaeobiological aspects. The Lameta Formation of the Maastrichtian age, traditionally considered to be fluvial in nature, is now revealing the evidences of short lived marine incursion as manifested by mineralogical constituents of the rocks, occurrence of calcareous algae and trace fossils. Similarly, its geographical extent of deposition, dinosaur inhabitation including its nesting site is now modified due to addition of one more inland basin of sedimentation in Central India.

The Bagh Group of rocks ranging from Cenomanian to Coniacian is of immense significance because of having records of fluvial to marine environments with good preservations of related sedimentological attributes, sea level fluctuation, fauna and flora. This group is also explored extensively for its floral and faunal contents, lithological variations and temporal changes in conditions of depositional environments.

In the present paper, authors have attempted to present the changing scenario of work on these two stratigraphic units. New evidences are discussed to update the status of Lameta Formation and Bagh Group research.

The Lameta Formation

The Lameta sediments, restricted to central and western India, are exposed as scattered patches in widespread Deccan Trap area due to Satpura and other faults. These patches, resting disconformably over the Gondwanas or unconformably above the Precambrian rocks, are reported from Jabalpur, Sagar, Amarkantak and Betul districts of Madhya Pradesh; Nagpur, Chandrapur and Amravati districts of Maharashtra and Balasinor of Gujarat. Beside, good development of areno-argillaceous and characteristic calcareous lithounits, these exposures also preserve dinosaurian remains including eggs and coprolites, which aid in reconstruction of palaeoclimatic and palaeoecological conditions.

Mohabey (1996a),on the basis of surface exposures of these sediments has identified five inland basins of Lameta sedimentation namely, i) Nand-Dongargaon basin, ii) Jabalpur basin, iii) Sagar basin, iv) Ambikapur-Amarkantak basin and, v) Balasionor-Jhabua basin. Recently, a new inland basin viz., Salbardi-Belkher has been added which has a separate geographic identity, however, lithological architecture and dinosaurian remains are same as of other inland basins (Mankar and Srivastava, 2015) (Fig.1a). Similarly, scientific contributions have been added in last decade i.e., trace fossils of marine affinity (Saha et al., 2010), report of marine calcareous algae and possibility of sea incursion (Srivastava et al., 2018), dinosaur skeletal remains including eggs and nests (Srivastava and Mankar, 2013, 2015a; Aglawe and Bhadran, 2014; 2018; Bhadran and Aglawe, 2015; Fernández and Khosla, 2015), review of faunal elements from infra- and Intertrappean sequences (Kapur and Khosla, 2018); reappraisal of glauconite (Bansal et al., 2018) and revised palaeogeographic limits of Lameta sedimentation (Mankar and Srivastava, 2019). In the present attempt, these aspects are being discussed and synthesized for

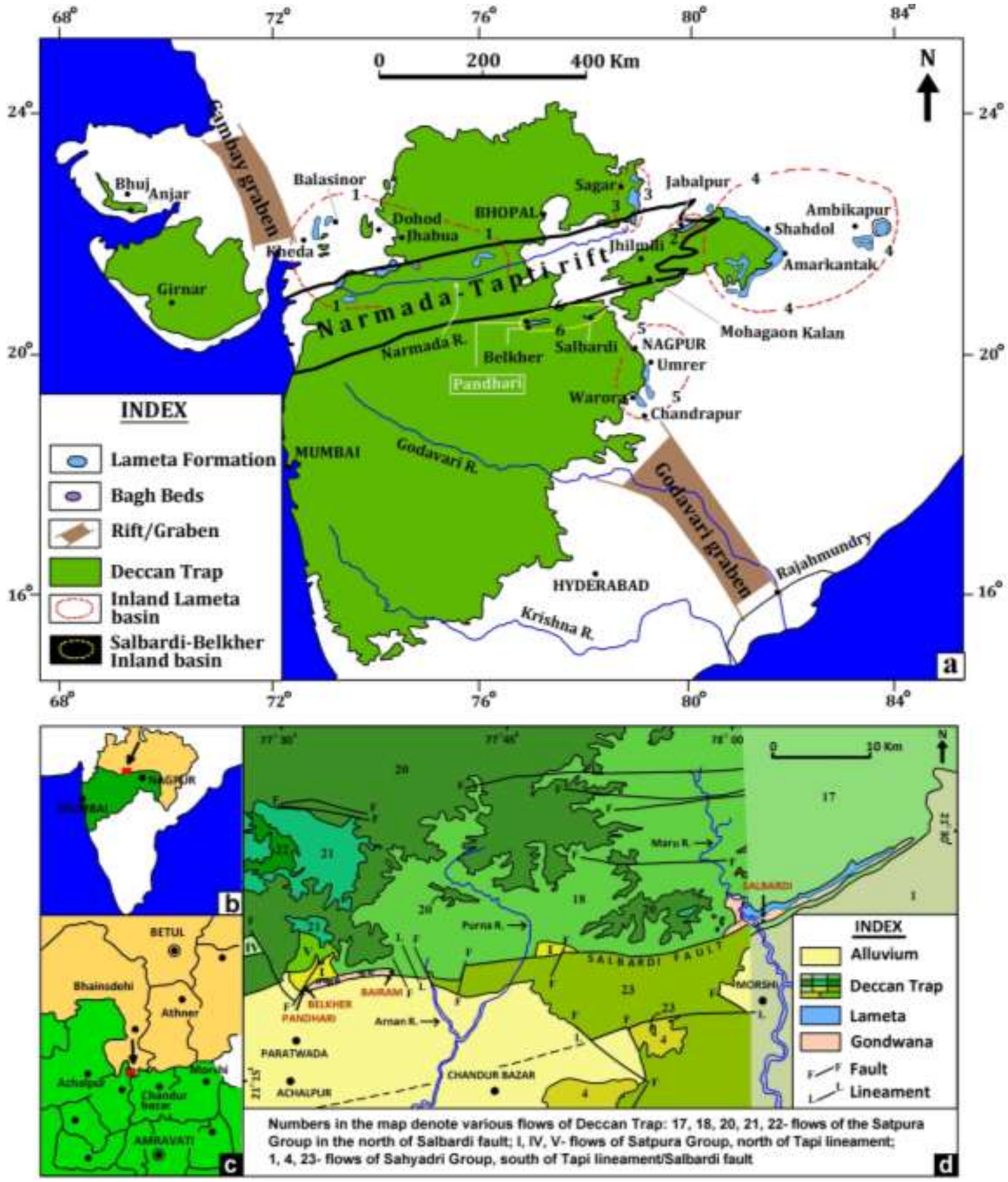

Fig. 1. Geological map proposed by Mankar and Srivastava (2019) showing: a) locations of various inland basins for Lameta sedimentation viz., 1) Nand-Dongargaon, 2) Jabalpur, 3) Sagar, 4) Ambikapur-Amarkantak, 5) Balasinor-Jhabua and 6) Salbardi-Belkher inland basin (Mohabey, 1996a; Bajpai, 2009; Keller et. al., 2009; Mankar and Srivastava, 2015); b,c) study area in regional and local set-up, d) locations of Pandhari, Bairam, Belkher and Salbardi areas in Salbardi-Belkher inland basin (GSI 2001, 2002).

comprehensive information on the Lameta sediments of India.

Recent studies in the Lameta Formation

Inception of Salbardi-Belkher inland basin

The Salbardi-Belkher inland basin in central India is a recent addition for Lameta sedimentation including dinosaur inhabitation (Mankar and Srivastava, 2015; 2019). It is located in the west of Nand-Dongargaon basin (Mohabey, 1996a) having almost same geographic extent as of the adjacent basin. The basin is established on the basis of four large and a few small Lameta exposures confined to its geographical area. The large exposures with good development of rocks ranging from 35 to 45m thickness are exposed at Bairam ($21^0$22'25" N: $77^0$37'23" E), Belkher ($21^0$21'48" N: $77^0$31'23" E), Pandhari ($21^0$22'02" N: $77^0$32'54" E) and Salbardi ($21^0$25'15" N: $78^0$00'00" E) (Fig. 1b).

In basinal set-up, the Lameta sediments along with disconformably overlying upper Gondwana rocks (~Jabalpur Group) are exposed in scattered manner in basaltic county of Deccan Trap. The basement rock is quartz-feldspathic gneiss of Archaean age, however, exposed at only Salbardi area. Alluvium and soil form the top of succession. The Lameta successions exposed at various areas have more or less similar lithological settings; however, lateral variations including thickness of various beds are frequent. The lithocolumn at Bairam locality (35m) is marked with brownish-yellowish-greenish clays with interbeddings of thin siliceous limestone at the base. It is overlain by medium to coarse grained arenaceous succession, followed by clay-marl with intercalations of siliceous limestone and further medium to coarse grained, bioturbated sandstone along with abundant arenaceous concretions. Overlying column is dominantly calcareous in nature i.e., nodular limestone having clasts of chert, jasper and, indurated, flat bedded chertified limestone. At Belkher area, the succession is comparatively thick and its lower arenaceous part is yellowish orange to grayish brown, medium to fine grained sandstone having preservations of parallel and cross beddings. Trace fossils namely, *Planolites, Planolites montanus, Thalassinoides* and stuff burrows are also reported showing polychaetes and crustaceans as benthonic community. The middle lithounit is calc-marl with abundant concretions and the upper part consists of nodular and chertified limestones. The Pandhari area succession can be considered as an eastward extension of the Belkher and lies barely at a distance of about one-kilometre in the east. Its lower part is dominantly represented by clays of greenish gray to yellowish brown shades having sandy concretions and interbeddings of siliceous and micritic limestones. The middle part is brownish-grayish-yellowish coloured, medium to fine grained, friable to hard sandstones with scattered occurrences of abundant irregular concretions. The upper calcareous column consists of brecciated, nodular and chertified limestones. The lower part of the succession at Salbardi area is dominantly arenaceous consisting of thinly bedded sandstones having intercalations of clayey beds. The middle part is calc-siliceous in nature with frequent lithological variations as recorded by preservations of by calcareous, calcretized beds, clayey horizons etc. The upper part is similar as the other localities and represented by nodular and chertified limestones. The top of succession is marked by intraformational brecciated limestone which is restricted to this locality only. Comparison of the lithological architecture of these successions with the Lameta successions of other basins shows almost similar set-up, however, variations in thickness of various lithounits are prominent (Fig. 2).

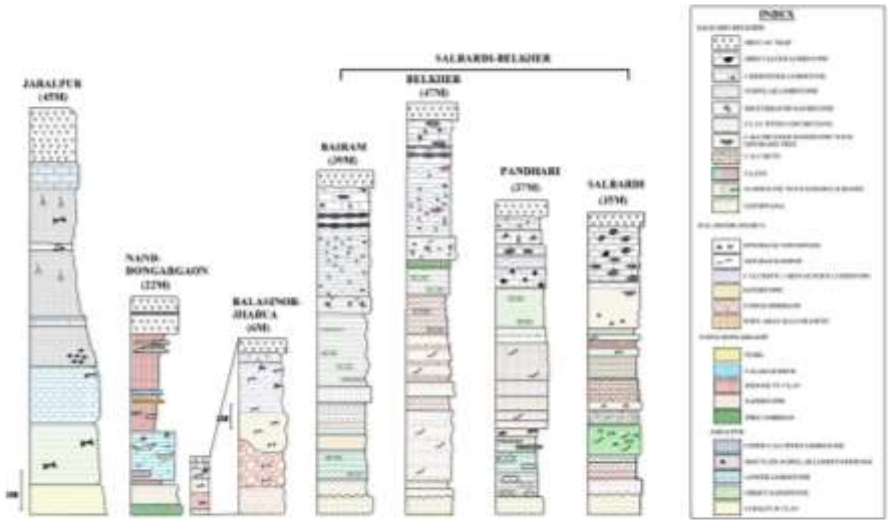

Fig. 2. Comparative lithologs of Lameta sediments in various inland basins of deposition (revised after Mankar and Srivastava, 2019).

Depositional environment and basin configuration

The newly added basin has also been investigated in detail for petrography, lithofacies and depositional environments (Srivastava and Mankar 2015b; Mankar and Srivastava, 2019). They have identified three different lithofacies associations i.e., a) arenaceous lithofacies, b) argillaceous lithofacies and, c) calcareous lithofacies. The arenaceous association includes, i) massive sandstone lithofacies, ii) green sandstone lithofacies, iii) thinly bedded, yellowish orange and grayish brown sandstone lithofacies, iv) coarse grained sandstone lithofacies, v) dark brown bioturbated sandstone lithofacies. The argillaceous association consists of, i) yellowish-brownish-greenish clay-siltstone lithofacies, ii) light gray silty clay with concretions lithofacies, whereas, the calcareous association includes, i) calcrete lithofacies, ii) nodular limestone lithofacies, iii) chertified limestone lithofacies and, iv) intraformational breccia lithofacies.

Based on lithofacies identified, their characteristic features and lithological architecture, the detailed depositional environments along with a model for temporal change in the environmental set-up have been proposed (Srivastava and Mankar, 2015b; Mankar and Srivastava, 2019). They interpreted fluvial-lacustrine set-up for the deposition of Lameta sediments in Salbardi-Belkher inland basin. Energy conditions of depositing medium and basin configuration have a control over the nature and pattern of sedimentation. The lower part of the succession at Salbardi area, associated disconformably with Gondwana succession, is represented together by medium to fine grained, thinly laminated sandstones having abundant rounded to subrounded pebbles of quartz and feldspar. It indicates low energy condition of deposition having common source of sediments as evident by the occurrence of pebbles of same nature in both the lithounits. However, the energy condition of the depositing medium was fluctuating, as represented by alternations of thin, fine grained argillaceous beds with cross to parallel bedded sandstones. Climate shows its influence during the deposition of the middle part of Salbardi succession as this lithounit is marked by pedogenic calcretes indicating prevalence of semiarid to arid climate (Wright, 1992; Wright and Tucker, 1991). During this period, the deposition has taken place in detached lakes and small water bodies having low water condition. This phase was followed by over flooding and high water condition of the river channel that favoured the deposition of medium to coarse, flat bedded sandstones. Preservation of about one-meter thick bioturbated sandstone at Belkher section suggests calm and quite water condition for a short duration indicating flourished but restricted diversity of benthonic fauna causing complete churning and intermixing of the sediments (Srivastava and Mankar, 2015b). They have also reported *Thalassinoides, Planolites, P. montanus* and stuffed burrows of crustaceans and polychaetes.

Nature of medium during the deposition of the upper calcareous columns shows a completely changed scenario from the previous. Dominance of various types of carbonate indicates an alkaline nature of depositing medium. A sheet flood environment of deposition as of type area succession (Tandon et al., 1995) has been interpreted for the contributing nodular and chertified limestones. Termination of the Lameta sedimentation took place due to changed climatic and geomorphic set-ups because of Deccan volcanic activity. The additional lithounit of intraformational breccia, forming the top of the Salbardi succession having clasts of pre-existing Lameta rocks in the micritic matrix exhibits a short phase of sediment transport by gravity flow mode.

The nature and configuration of the new basin is similar as of other inland basins identified by Mohabey (1996a) viz., Jabalpur, Nand-Dongargaon and Balasinor-Jhabua having fluvio-lacustrine set-up and also inhabitation of dinosaur. The size of the basin is almost equal to Nand-Dongargaon (Mohabey, 1996a), however, extended in east-west directions. The basin was comparatively shallow in the east as revealed by the calcrete horizons and calcretized sandstones in the lower part of Salbardi succession. In contrast, the Pandhari and Belkher exposures in extreme west are dominantly argillaceous in nature. These fine grained sediments are massive to laminated in nature showing suspension mode of deposition in low energy or, calm water condition depicting relatively deeper condition of the basin (Srivastava and Mankar, 2015b; Mankar and Srivastava, 2019).

Trace fossils

Singh (1981) reported vertical to inclined cylindrical burrows of *Thalassinoides* affinity from the Mottled Nodular Sandstone and the Upper Sandstone members of the type area succession at Jabalpur and interpreted coastal complex setting of the deposition. Recently, Shah et al. (2010) reported certain trace fossils from various members of Lameta Ghat and Chui Hill sections of Jabalpur area viz., *Arenicolites, Calycraterion, Fucusopsis, Laevicyclus, Macanopsis, Ophiomorpha, Paleomeandron, Rhizocorallium, Stipsellus, Thalassinoides* and *Zoophycos* together from Lower Limestone, Mottled Nodular Sandstone and Upper Sandstone. They interpreted that the trace fossil assemblage, including sedimentlogical attributes of lithounits, indicate coastal marine setting of deposition under sub aerial condition. Srivastava and Mankar (2012) reported *Thalassinoides, Planolites, P. montanus* and stuffed burrows from Belkher section of Salbardi-Belkher basin. They have not commented on the environment specifically as all the ichnofossils are facies crossing, however, placed them into fluvial-lacustrine environment on the basis of general agreement on same environment for most of the Lameta basins.

Dinosaurian remains including eggs

Dinosaur skeletal remains belonging to sauropod and theropod are reported mainly from Jabalpur, Balasinor-Jhabua, Nand-Dongargaon and Salbardi-Belkher inland basins. These remains from Jabalpur basin includes *Titanosaurus indicus* (Lydekker, 1877) and *Antarctosaurus septentrionalis* (Huene and

Matley, 1993) belonging to sauropod which were later validated to *Titanosaurus colberti* (*Isisaurus colberti*) (Wilson and Upchurch, 2003) and *Jainosaurus septentrionalis* (Hunt et al., 1994). The theropod includes *Indosuchus raptorius* (Huene and Matley, 1993), *I. matleyi* (Huene and Matley, 1993), *Lametasauru sindicus* (Matley, 1924), *Composuchus solus* (Huene and Matley, 1993), *Laevisuchus indicus* (Huene and Matley, 1993), *Jubbalppuria tenuis* (Huene and Matley, 1993), *Dryptosauroides (?)grandis* (Huene and Matley, 1993), *Ornithomimoides mobilis* (Huene and Matley, 1993), *O. barasimlensis* (Huene and Matley, 1993), *Ornithogoniosaurus matleyi* (Das-Gupta, 1930), *Coeluroides largus* (Huene and Matley, 1993) and *Brachypodosaurus gravis* (Huene and Matley, 1993). However, all these reported species were later validated to *Indosuchus raptorius* (Huene and Matley, 1993), *I. matleyi* (Huene and Matley, 1993) and *Laevishuchus indicus* (Huene and Matley, 1993). Similarly, Sauropod viz., *Antarctosaurus septentrionalis* (Mathur and Pant, 1986) and *Titanosaurus rahioliensis* (Mathur and Srivastava, 1987) reported earlier from Balasinor-Jhabuabasin were later redefined as *Jainosaurus septentrionalis*(Wilson et al., 2003). From Nand-Dongargaonbasin,sauropod remains belong to *Titanosaurus indicus* (Lydekker, 1877), *T. Blandfordi* (Lydekker,1879), *T.colberti* (Jain and Bandyopadhyay, 1997) and *Laplatasurus madagascariensis* (Huene and Matley, 1933) were later confined to *Titanosauru scolberti* (*Isisaurus colberti*) (Wilson and Upchurch, 2003). Matthew et al. (2010) discussed the history of collection of dinosaurian remains in central India during 1828-1947. They described early findings which are significant to understand the evolution, extinction and biogeography of dinosaurs. Recently, sauropod remains from Salbardi area belonging to *Titanosaurus colberti* (*Isisaurus colberti*) (Wilson and Upchurch, 2003) has been added by Srivastava and Mankar (2013). Fragmentary bones of turtle (Aglawe and Bhadran, 2014) and theropod (Bhadran and Aglawe, 2015) have also been reported from the same area. Apart from this, huge collection made from Salbardi and Pandhari area is under investigation by the authors group.

Similarly, the dinosaurian eggs and egg-nests are also reported from this basin for and were subjected for detailing and proper identification by subsequent researchers. The Jabalpur basin bears the report of *Megalolithus horidungriensi, M. cylindricus, M. jabalpurensis, M. Matleyi* (Junior synonym of *jabalpurensis*), *M. Phensaniensis* (Junior synonym of *matleyi*), *M. mohabeyi, M. baghensis, M.*

dholiyaensis, M. padiyalensis (Junior synonym of *Mohabeyi*) and *M. Dhoridungriensis* (Khosla and Sahni, 1995; Mohabey, 1996b; Vianey-Liaud et al., 2003) which have been later validated as *M. cylindricus, M. jabalpurensis, M. megadermus* and *Fusioolithus. baghensis* by Fernández and Khosla (2015). Shukla and Srivastava (2008) reported lizard eggs-nest of eleven eggs represented by nine partially preserved and two complete eggs from the Lower Limestone member of Jabalpur area and also commented that the deposition of host lithounit has taken place in alkaline lagoon that was connected to a marine embayment by channels. Later, on the basis of shape, pattern and ultra structure of the eggs, these were reassigned to be of crocodilian nest by Srivastava et al. (2015). They also suggested near shore, lagoonal and supratidal settings of deposition for this lithounit. The reported oospecies from Balasinor-Jhabua basin includes *M. rahioliensis (=cylindricus), M. phensaniesis, M. khempurensis (=megadermu), M. kachchhensis, M. dhoridungriensis, M. megadermusM. Balasinorensis* (junior synonym of *baghensis*), *Phensaniensis* (junior synonym of *mohabeyi*) and *Problematica* (?) (Mohabey, 1996b; Khosla and Sahni, 1995; Vianey-Liaud et al., 2003) were later redefined and restricted to only *M. cylindricus, M. jabalpurensis, M. megadermus, Fusioolithus baghensis* by Fernández and Khosla (2015). *M. matleyi* and *M. megadermus* (Mohabey, 1996b) from Nand-Dongargaon basin were later identified as *M. megadermus* and *M. jabalpurensis* by Fernández and Khosla (2015). Oogenus *Megaloolithus* is a recent addition from Salbardi area by Srivastava and Mankar (2015a) which is based on one complete and 3 incomplete eggs/ egg shell fragments. Recently, Aglawe and Lakra (2018) added *Megaloolithus cylindricus* from the Salbardi-Belkher inland basin.

Four types of coprolites from the Pisdura area of Nand-Dongargaon basin have already been reported by Matley (1939). Samant and Mohabey (2014) have studied palynomorphs from coprolites from the same basin and reported *Lecaniella* sp. *Oedogonium* sp. *Azolla* sp. *Araucariacites australis, Cycadopites* sp. *Classopollis* sp. *Podocarpidites* sp. *Cretacaeiporites* sp. *Compositoipollenites* sp. *Graminidites annulatus, Graminidites assamicus, Longapertites* sp. *Multiareolites* sp. *Palmaepollenites* sp. *Palmaepollenites* sp. *Periporopollenites* sp. *Retimonosulcites* sp. Alongwith *tetracolporate* pollens, *Tricolporate* pollen and fungal spores. Khosla et al. (2015) reported microbiota and plant remains from Type A coprolites of Nand-Dongargaon basin and interpreted that the faecal produces were intentional and inadvertent omnivorous that used to consume appreciable portion of animal tissues. Sonkusare et al. (2016) also reported assemblage of diverse spores and pollen, phytoliths, fungal remains etc. from sauropod coprolites of Nand-Dongargaon basin and interpreted that the sauropod ate soft tissues of angiosperms and gymnosperms.

Marine incursions and revised palaeogeography

Depositional environment for the Lameta succession is a matter of debate from last four decades that still continues. Traditionally, the formation is considered to be fluvio-lacustrine in nature, however, with restrictions for certain parts of the succession. Initially, the exposures of Jabalpur area have attracted the controversy about its fluvial-lacustrine or coastal complex setting of environment of deposition. The previous is advocated mainly on the basis of non marine floral and faunal remains along with dinosaurian skeletal remains, eggs, eggs-nest and coprolites (Mately, 1921; Pascoe, 1964; Mohabey, 1996b; Srivastava and Mankar, 2013, 2015a); characteristic lithological features including calcretization in alluvial plain environment, Jabalpur area (Brookfield and Sahni, 1987); pedogenic calcrete formation in sub-aerially exposed, semi arid, low gradient, pre-palustrine alkaline flat alluvial setting, Jabalpur area (Tandon et al. 1990, 1995, 1998; Tandon and Andrews, 2001); fluvial setting based on sedimentological studies of Bokara and Jaripatka area of Nagpur (Soman and Deshpande 1993); field details and petrography of Lameta sandstone of Jabalpur area interpreting Mahakoshal and Jabalpur groups as provenance for sediment supply (Ansari et al. 2008) studied. The other school of thought supporting coastal complex setting is based on the reports of algal structures and glauconite minerals in Green Sandstone lithounit (Chanda, 1963a,b, 1967; Chanda and Bhattacharya, 1966; Singh, 1981; Singh and Srivastava, 1981); facies architecture similar to coastal complex settings including beds having bioturbations and preservation of cylindrical burrows similar to *Thalassinoides* (Kumar and Tandon, 1977, 1978, 1979). Singh et al. (1983) discussed the stratigraphy and palaeoenvironmental set up based on the study of the Green Sandstone of the Jabalpur area and suggested estuarine channel deposit. Recently, Shukla and Srivastava (2008) and Saha et al. (2010) also supported coastal complex setting on the basis of records of lizard eggs and trace fossils of marine affinity. Prasad et al. (2011) reported fossil cuticles and associated phytoliths of the rice tribe in the Cretaceous period. The new fossil of grass suggests the changes in diversification and evolution in the varieties during Cretaceous time. Khosla (2014) described charophyta gyrogonite from the Lameta sediments of Jabalpur and concluded local lacustrine and palustrine depositing conditions. Murkute et al. (2016) made petrological studies including heavy and clay minerals of the Lameta exposures of Nagpur and surrounding areas and suggested lacustrine to fluvial environment of deposition.

In recent decade, many researchers have advocated for marine influence during the deposition of type area succession which is based on preservations of dinosaur/crocodile eggs, trace fossils, lithological architecture and traces of authigenic glauconite. Preservation of lizard egg-nest in the Lower Limestone and architectural setup of lithofacies suggest alkaline lagoon, connected to a marine embayment by channels (Shukla and Srivastava, 2008). However, the identification of eggs as of lizard was further redefined to crocodile affinity (Srivastava et al., 2015) but retained the depositional setup to coastal complex as suggested by Shukla and Srivastava (2008) i.e., near shore, lagoonal and supratidal setting. Trace fossils, specific to marine environment from Lameta Ghat and Chui Hill sections of Jabalpur area and bedding geometry of their host lithounits are suggest of marginal marine condition of deposition (Saha et al., 2010). Recently, Bansal et al. (2018) reported authigenic glauconite from the Green Sandstone lithounit of the Lameta Formation exposed at Phutlibaori area of Madhya Pradesh. They interpreted that the mineral is formed by the replacement of K-feldspar, primarily in the cleavages and fractures of feldspar, along peripheries of feldspar which later evolved as pellets in due course of time. The study is based on detailed geochemical and structure element studies i.e., EPMA, XRD, SEM, Mössbauer spectroscopy, field emission gun-scanning electron microscopy etc. They further interpreted that the glauconite with high concentrations of K, Si, Mg, Al and moderate Fe indicate its formation due to pseudomorphic replacement of K-feldspar in an estuarine environment.

Similar phenomena i.e., marine influence during the deposition of Lameta sediments is also reported from newly established Salbardi-Belkher inland basin. Srivastava et al. (2018) proposed short lived marine incursion on the basis of calcareous algae at Pandhari locality of the new basin. A thin discontinued bed of micritic limestone, preserved in lower argillaceous column having small, fragmentary bones of dinosaur, is marked with abundant calcareous algae. These algal remains are represented by chlorophyta viz. *Clypeina* sp., *Acroporella* sp., *Trinocladusradoicicae*, *Trinocladus* sp., *Dissocladellaundulata*, *Dissocladella* sp., (dasycladalean algae); *Halimedacylindracea*, *Halimeda* sp., (halimedacean); *Ovulites*sp. (ovulites); *Microchara* sp. (charophyta), *Lithoporella* sp., and *Sporolithon* sp. (rhodophyta).

The Bagh Group

The Bagh Group of rocks (Cenomanian-Coniacian) are exposed as small detached outcrops along the north bank of Narmada river in central and western India. Good exposures have been reported from Dhar, Jhabua and Vadodara (Baroda) districts of Madhya Pradesh and Gujarat, however, the type area locality of Bagh, have been explored extensively for sedimentological and palaeobiological details (Fig. 3a, b). These sediments are mostly unmetamorphosed, undeformed, flat bedded and rest unconformably over the Precambrian Bijawar Group. In most of the area, the Deccan Trap volcanics of Late Cretaceous period forms the capping. Stratigraphically, the succession was initially subdivided informally into four lithounits by Blandford (1869) which have been later subjected to refinement and formal classification by many researchers. The recent stratigraphic set-up proposed for the succession includes three formations viz., the Nimar Sandstone, the Nodular Limestone and the Coralline Limestone <u>(Tripathi, 2006; Jatley and Ajane, 2013) which was further revised by Racey et al. (2016) (Table 1).</u>

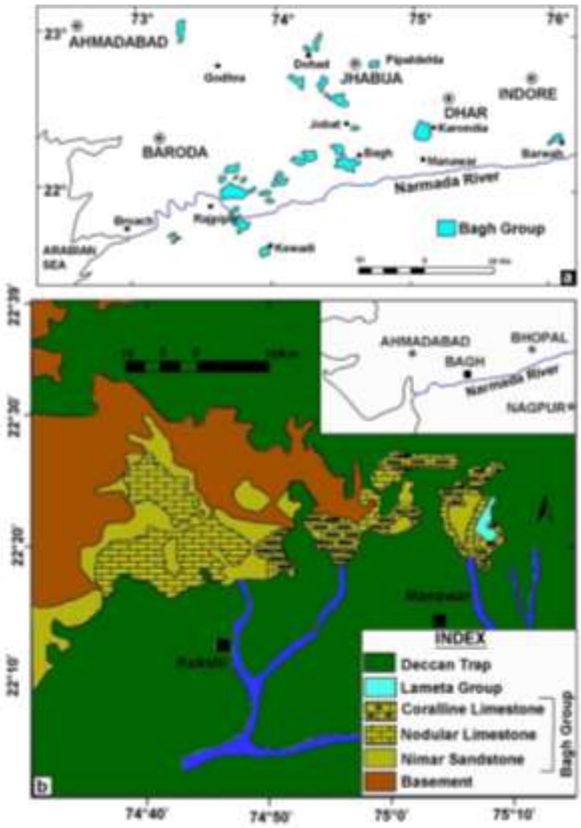

Fig. 3. Geological map showing, a) Bagh Group of rocks at various localities along Naramda river (Kundal and Sanganwar, 1998); b) stratigraphic set-up of Bagh Group of rock at type area (Kumar et al., 2018).

Lameta Group and Deccan Traps			
Group	Formation	Member	Age
Bagh	Coralline Limestone		Coniacian
	Nodular Limestone	Chirakhan	Turonian
		Karondia	
Crystalline rocks			

Table 1. Stratigraphic set-up of Narmada basin (Tripathi, 2006; Jaitly and Ajane, 2013).

Background Information

The depositional environment, fossil content and biogenic structures were the significant aspects of work from decades back (Rode and Chiplonkar, 1935; Roy Chowdhary and Sastri, 1962; Murtyet al., 1963; Poddar, 1964; Sahni and Jain, 1966; Blandford, 1869; Pal, 1971; Dassarma and Sinha, 1975; Bose, 1884; Ramasamy and Madhavaraju, 1993; Taylor and Badve1995; Tripathi, 1995, 2000; Kennedy et al., 2003). Prasad et al. (1998) carried out paleomagnetic studies of Cretaceous Bagh Group from Narmada basin, which revealed reverse polarity for the entire succession with depositional age within the Cretaceous Normal Superchron. They concluded that Bagh Group has been remagnestized by igneous activity of Deccan basalt effusion and suggested counter clockwise rotation by 13$\pm$3°and latitudinal drift of Indian continent northwards by 3+3° during Deccan Volcanism. Vaidhynathan and Ramakrishnan (2008) compiled the available data on depositional environment and concluded that the sedimentation of Bagh Group of rocks started in fresh water fluviatile and estuarine conditions during the deposition of lower part of Nimar Sandstone which was further replaced by marine environment having many transgressive and regressive phases during the deposition of remaining successive lithounit.

Plenty of marine fossils belonging to ammonoids, bivalves, gastropods and echinoids are reported from this group. These fossils serve as a significant tool to redefine the biostratigraphy. Broadly, the age and stratigraphy of the Bagh Group were a matter of discussion. The age connotation of the succession is based on the fossil content i.e., ammonides (Chiplonkar and Ghare, 1976; Badve and Ghare, 1977; Chiplonkaret al., 1977; Bardhanet al., 2002; Kennedy et al., 2003; Jaitly and Ajane, 2013); bivalves (Kumar et al., 2018); echinoderms (Smith, 2010); nannofossils (Jafar, 1982); calcareous algae (Kundal and Sanganwar, 1998); and foraminifers (Raceyet al., 2016).

Trace fossil belonging to shallow marine environment are also reported (Chiplonkar and Badve, 1970, 1972). Fragmentary bones of dinosaurs e.g., humorous, femur, radius and ulna belonging to sauropod from the Nimar Sandstone of Dhar district are reported by Khosla et al. (2003).

Recent Studies in the Bagh Group of rocks

Racey et al. (2016) collected extensive field data from Cretaceous outcrops of North-East India including Narmada basin and provided revised chronostratigraphic framework based on litho-and biostratigraphic data base. They subdivided marine rocks of the Narmada basin into two i.e., the Lower Cretaceous Nimar Group and the Upper Cretaceous Bagh Group. The previous is further subdivided into, i) the Nimar Sandstone (Hauterivian-Albian) of fluvial nature and, ii) the 'Upper Nimars' of fluvial to shallow marine sediments of the (Albian-Cenomanian). Similarly, the Bagh Group of Turonian age has also been subdivided into, i) the Nodular Limestone Formation of deep to shallow shelf environment and, ii) Coralline Limestone Formation of temperate shallow marine condition. They have also provided the index fossil assemblages of various stratigraphic units in support of their stratigraphic divisions. Apart from using earlier reported fossils contents from various lithounits, the validation of the ages particularly for the Nodular Limestone and the Coralline Limestone formations are also supported with new records of foraminifers viz., *Praeglobotruncana stephani, Helvetoglobotruncana helvetica, Gavelinella tourainensis* for the previous, whereas *Rotalia* cf *algeriana* for later.

Bhattacharya and Jha (2014) studied tidalites from Nimar Sandstone which indicates sedimentation in upper subtidal to lower intertidal within fluvio-marine interactive system. The estimated parameter of earth-moon system in late Cretaceous time reveals no changes in last 100 Ma. Jha et al. (2016) reported seismites that are soft sediment deformational structures which were formed due to passing up of earthquake shocks from unconsolidated sediments. These structures, represented by convolute laminae, load and flame structures, pseudo nodules, contorted beddings, syn-sedimentary faults are preserved in middle part of the Nimar Sandstone. Based on the genetic aspects of the same, Jha et al. (2016) have interpreted a new phase of reactivation of Son-Narmada South Fault during the Cenomanian period. They have also made detailed study about various facies associations and interpreted that the lower part of lithounit shows predominantly fluvial setting of the deposition whereas, the middle and upper parts exhibit tide dominated estuarine to tide-wave influenced shoreface environment. Recently, Bansal et al. (2019) investigated glauconitic bed within the Limestone Formation of the Bagh Group in central India. They proposed that glauconites were formed within a shallow marine deposit across the Tethyan belt due to enhanced supply of K, Si, Al, Fe, Mg cations through continental weathering. The interpretation is based on petrography, geochemistry and mineralogy of the glauconite.

The report of dinosaurian remains from the succession was restricted to sauropod only (Khosla et al., 2003).So far, there was no record of theropoda from the Bagh Group. Recently, Prasad et al. (2016) discovered three isolated archosaur teeth from an oyster bearing Green Sandstone lying at the top of the Coralline Limestone at Phutibaori village of Dhar district. They identified two teeth of abelisaurid dinosaur (theropod), which is based on their similarities with premaxillary and maxillary tooth morphologies of *Majungasaurus* and *Indosuchus* and, remaining one is of indeterminate crocodile. These remains are considered it to be of Pre-Late to Late Maastrichtian age which is based on the stratigraphic position and age of host bed in the succession.

Patel et al. (2018) reported trace fossils viz., *Conichnusconicus, Conostichus broadheadi* and *C. stouti* from intercalated micritic sandstone and sandy allochemic limestone shale sequence of Bagh Group exposed in Man river basin at Uchad and Bhekhadiya villages. They have interpreted these ichnospecies as resting/dwelling structures of sea anemone which are preserved in association with Oyster fossils indicating shallow marine environment of deposition.

Ruidas et al. (2018) revisited the stratigraphic set-up including lithological details, fossil contents, trace fossils etc. The work is based on detailed field investigations of various localities including some of the unexplored sections. They proposed that the Nodular Limestone can be subdivided into three subunits equivalent to 'member' and also provided specific details of these subunits including their faunal assemblage and localities of ideal sections. Comments have also been made on their specific preservational attributes related with sea level fluctuations. Further, the nature and origin of modularity in the succession have also been explained. They suggested that the modularity is because of mechanical compaction due to the over burden of the Lameta Formation and Deccan Trap followed by the chemical compaction. Kumar et al. (2018) attempted to redefine the Nodular Limestone Formation of Bagh area on the basis of ammonoid and *Inoceramus* index taxa and assigned Turonian age for the formation. They further identified lower, middle and upper Turonian lithounits of the succession, of which, the age assigned to previous is based on *Spathites* and *Collignoniceras*. The middle is marked by *Collignoniceras* cf. *Carolinum* and *Inoceramus hobetsensis* whereas, the Upper Turonian stage is by an index species of *Inoceramus teshioensis,* preserved in association with *Placenticerasmintoi.*

Gaps in studies and perspective for future research

The literature survey reveals a good data bank on both Lameta Formation and Bagh Group of rocks covering mostly sedimentological and palaeobiological aspects including dinosaurs. However, there is a need for aspect based precise study. The Lameta sediments have been documented largely as fluvial, marginal marine or, of coastal complex, in addition to have marine incursions. This aspect needs a clear picture by reconstructing basin configuration in regional set up and establishment of event stratigraphy based on depositional environments, impacts of faunal and floral contents and determination of depositional ages. Secondly, there is a need to study depositional set up, flora, fauna including dinosaurs in context of revised palaeogeographic set up for Lameta sedimentation based on recent addition of the new Salbardi-Belkher inland basin to earlier identified five basins. Similarly, the Bagh Group still needs a precise stratigraphy that may be redefined by various micro and mega fossils. Here also, identifications of temporal changes in environmental and climatic conditions are requires for which, successions of the Bagh Group offer good scope for work.

Acknowledgement

Certain part of the fieldwork and collection of data in the initial phase have been done/carried out during a major research project (no. F.40/295/2011 SR) by UGC, New Delhi, awarded to AKS, is thankfully acknowledged.

References

Aglawe, V. A. and Bhadran, A. (2014), First report of turtle bones and occurrence of dinosaurian bones from Lameta Formation, Ghorpend village, Salbuldi area, Betul district, Madhya Pradesh: Geological Survey of India (Central region), News v. 30.

Aglawe, V. A. and Lakra, P. (2018), Upper Cretaceous (Maastrichtian) dinosaur eggs *Megaloolithus cylindricus* from Salbardi-Ghorpend area, Betul district, Madhya Pradesh: Journal of the Palaeontological Society of India, v. 63 (2), p. 191-196.

Badve, R. M. and Ghare, M. A. (1977), Palaeoecological aspects of the Bagh Beds: India: In: Recent Researches in Geology 4, Professor G. V. Chiplonkar Commemorative Volume, Hindustan Publishing Corporation, New Delhi, p. 388–402.

Bajpai, S. (2009), Biotic perspective of the Deccan volcanism and India-Asia collision: Recent advances. In: Current Trends in Science, Platinum Jubilee Special Publication, Indian Academy of Sciences, p. 505-516.

Bansal, U. Banerjee, S. Ruidas, D. K. and Pande, K. (2018), Origin and geochemical characterization of the glauconite in the Upper Cretaceous Lameta Formation, Narmada Basin, Central India: Journal of Palaeogeography, v. 7(2), p. 99-116 (00141).

Bansal, U. Banerjee, S. Pande, K. and Ruidas, D. K. (2019), Unusual seawater composition of the Late Cretaceous Tethys imprinted in glauconite of Narmada basin, central India: Geological Magazine, doi.org/10.1017/S0016756819000621.

Bardhan, S. Gangopadhyay, T. K. and Mandal, U. (2002), How far did India drift during the Late Cretaceous? *Placenticeras kaffrarium* Etheridge, 1904 (Ammonoidea) used as a measuring tape: Sedimentary Geology, v. 147, p.193–217.

Bhadran, A. and Aglawe, V. A. (2015), First report of Theropod (Dinosauria) from Upper Cretaceous (Maastrichtian) Lameta Formation of Salbardi basin, Betul district, Madhya Pradesh: Indian Journal of Geosciences, v. 69 (2), p. 421-424.

Bhattacharya, B. and Jha, S. (2014), Late Cretaceous diurnal tidal system: a study from Nimar Sandstone, Bagh Group, Narmada valley, central India: Current Science, v. 107(6), p. 1032-1037.

Blanford, W. T. (1869), On the geology of Tapti and lower Narbada Valley and some adjoining districts: Memoir Geological Survey of India, v. 6 (3), p.163-384.

Bose, P. N. (1884), Geology of Lower Narbada Valley between Nimavar and Kawant: Memoir Geological Survey of India, v. 21, p. 45.

Brookfield, H. E. Sahni, A. (1987), Palaeoenvironments of Lameta Beds (Late Cretaceous) at Jabalpur, Madhya Pradesh, India: soil and biotas of a semi-arid alluvial plain: Cretaceous Research, v. 8, p. 1-14.

Chanda, S. K. (1963a), Cementation and diagenesis of the Lameta Beds, Lameta ghat, India: Journal of Sedimentary Petrology v. 33 (3), p. 728-738.

Chanda, S. K. (1963b), Petrography and origin of Lameta Sandstone, Lameta ghat, Jabalpur, M. P. India: Proceedings of the National Academy of Sciences, v. 29 (A), p. 578- 587.

Chanda, S. K. (1967), Petrogenesis of the calcareous constituents of the Lameta Group around Jabalpur, M. P., India: Journal of Sedimentary Research, v. 37 (2), p. 425-437.

Chanda, S. K. and Bhattacharya, A. (1966), A re-evaluation of the stratigraphy of the Lameta-Jabalpur contact around Jabalpur, M. P.: Journal of the Geological Society of India, v. 7, p. 91-99.

Chiplonkar, G. W. and Badve, R. M. (1970), Trace fossils from the Bagh Beds: Journal of the Paleontological Society of India, v. 14, p. 1-10.

Chiplonkar, G. W. and Badve, R. M. (1972), Trace fossils from the Bagh Beds: Pt. II, Journal of the Paleontological Society of India, v. 15, p. 1-5.

Chiplonkar, G. W. and Ghare, M. A. (1976), Palaeontology of the Bagh Beds–Part VII: ammonoidea: Bulletin Earth Science, v. 4 & 5, p. 1–10.

Chiplonkar, G. W., Badve, R. M. and Ghare, M. A. (1977), On the stratigraphy of Bagh Beds of the Lower Narmada valley. In: Venkatachala, B.S. & Sastri, V.V. (eds) Proceedings of Fourth Indian Colloquium Micropaleontology and Stratigraphy. Institute of Petroleum Exploration, Oil & Natural Gas Commission, Dehradun, p. 209–216.

Das-Gupta, H. C. (1930), On a new theropod dinosaur (*Orthogoniosaurus matleyi*, n. gen. et n. sp.) from the Lameta beds of Jubbulpore: Journal of the Asiatic Society of Bengal, New Series, v. 16, p. 367-369.

Dassarma, D. C. and Sinha, N. K. (1975), Marine Cretaceous formations of Narmada Valley (Bagh Beds), Madhya Pradesh and Gujarat: Geol. Sur. India, Palaeontologia Indica, p. 42.

Fernández, M. S. and Khosla, A. (2015), Parataxonomic review of the Upper Cretaceous dinosaur eggshells belonging to the oofamily Megaloolithidae from India and Argentina: Historical Biology, v. 27 (2), p. 158-180.

GSI. (2001), District Resource Map-Amravati district, Maharashtra. Government of India Publication.

GSI. (2002), District Resource Map-Betul district, Madhya Pradesh. Government of India Publication.

Huene, F. V. and Matley, C. A. (1933), The Cretaceous Saurischia and Ornithischia of the central provinces of India: Memories of Geological Survey of India. Palaeontologia Indica, v. 21(1), p. 1-72.

Hunt, A. P., Lockley, M. G., Lucas, S. G. and Meyer, C. A. (1994), The global sauropod fossil record: Gaia, v. 10, p. 261-279.

Jafar, S. A. (1982), Nannoplankton evidence of Turonian transgression along Narmada Valley India, and Turonian–Coniacian boundary problem: Journal of the Paleontological Society of India, v. 27, p. 17–30.

Jain, S. L. and Bandopadyay, S. (1997), New titanosaurid (Dinosauria: Sauropopda) from the Late Cretaceous of Central India: Journal of Vertebrate Paleontology, v. 17(1), p. 114-136.

Jaitly, A. K. and Ajane, R. (2013), Comments on *Placenticeras mintoi* (Vredenburg, 1906) from the Bagh Beds (Late Cretaceous), Central India with special reference to Turonian Nodular Limestone horizon: Journal of the Geological Society of India, v. 81, p. 565-574.

Jha, S., Bhattacharya, B. and Nandwani, S. (2016), Significance of seismites in the Late Cretaceous transgressive Nimar Sandstone succession, Son-Narmada rift valley, Central India: doi: 10.1002/gj.2839.

Kapur, V. V. and Khosla, A. (2018), Faunal elements from the Deccan volcano-sedimentary sequences of India: A reappraisal of biostratigraphic, palaeoecologic, and palaeobiogeographic aspects: special issue article, Geological Journal, p. 1-32, 10.1002/gj.3379.

Keller, G., Adatte, T., Bajpai, S., Mohabey, D. M., Widdowson, M., Khosla, A., Sharma, R., Khosla, S. C., Gertsch, B., Fleitmann, D. and Sahni, A. (2009), K-T transition in Deccan traps and Intertrappean beds in central India mark major marine seaway across India: Earth Planetary Science Letters, v. 282, p. 10-23.

Kennedy, W. J., Phansalkar, V. G. and Walaszczyk, I. (2003), *Prionocyclus germari* (Reuss, 1845), a Late Turonian marker fossil from the Bagh

Beds of central India: Cretaceous Research, v. 24, p. 433-438.

Khosla, A. (2014) Upper Cretaceous (Maastrichtian) charophyte gyrogonites from the Lameta Formation of Jabalpur, Central India: palaeobiogeographic and palaeoecological implications. Acta geologica polonica, v. 64 (3), p. 311-323.

Khosla, A. and Sahni, A. (1995), Parataxonomic classification of Late Cretaceous dinosaur eggshell from India: Journal of the Paleontological Society of India, v. 40, p. 87-102.

Khosla, A, Kapur, V. V., Sereno, P. C., Wilson, J. A., Wilson, G. P., Dutheil, D., Sahni, A., Singh, M. P., Kumar, S. and Rana, R. S. (2003), First dinosaur remains from the Cenomanian–TuronianNimar Sandstone (Bagh Beds), District-Dhar, Madhya Pradesh, India: Journal of the Paleontological Society of India, v. 48, p.115–127.

Khosla, A., Chin, K., Alimohammadin, H. and Dutta, D. (2015), Ostracods, plant tissues, and other inclusions in coprolites from the Late Cretaceous Lameta Formation at Pisdura, India: Taphonomical and palaeoecological implications: Palaeogeography, Palaeoclimatology, Palaeoecology, v. 418, p. 90–100.

Kumar, S. and Tandon, K. K. (1977), A note on bioturbation in the Lameta beds, Jabalpur area, M.P.: Geophytology, v. 7 (2), p. 135-138.

Kumar, S. and Tandon, K. K. (1978), *Thalassinoides* in the Mottled Nodular Beds, Jabalpur area, M. P.: Current Science, v. 47(2), p. 52-53.

Kumar, S. and Tandon, K. K. (1979), Trace fossils and environment of deposition of the sedimentary succession of Jabalpur, M. P.: Journal of the Geological Society of India, v. 20, p. 103-106.

Kumar, S., Pathak, D. B., Pandey, B., Jaitly, A. K. and Gautam, J. P. (2018), The age of the Nodular Limestone Formation (Late Cretaceous), Narmada Basin, central India: Journal of Earth System Science, p. 127:109, doi.org/10.1007/s12040-018-1017-1.

Kundal, P. and Sanganwar, B. N. (1998), Stratigraphical, palaeogeographical and palaeoenvironmental significance of fossil calcareous algae from Nimar Sandstone Formation, Bagh Group (Cenomanian–Turonian) of Pipaldehla, Jhabua Dt, MP: Current Science, v. 75, p. 702–708.

Lydekker, R. (1877), Note of new and other vertebrate from Indian Tertiary and secondary rocks: Records of Geological Survey of India, v. 10, p. 38-41.

Lydekker, R. (1879), Indian pre-Tertiary vertebrate: Fossils reptilian and batrachian: Memoir of Geological Survey of India, Paleontological Division, v. 4, p. 1-36.

Mankar, R. S. and Srivastava, A. K. (2015), Salbardi–Belkher inland basin: a new site of Lameta sedimentation at the border of districts Amravati, Maharashtra and Betul, Madhya Pradesh, Central India: Current Science, v. 109 (7), p. 1337-1344.

Mankar, R. S. and Srivastava, A. K. (2019), Revised paleogeography of the dinosaur bearing Maastrichtian Lameta Formation, Central and Western India: in the perspective of newly identified Salbardi-Belkher inland basin: Journal of the Sedimentary Environment, v. 4(1), p. 53-71.

Mathur, U. B. and Pant, S. C. (1986), Sauropod dinosaur humeri from Lameta Group (Upper Cretaceous- ? Palaeocene) of Kheda District, Gujarat: Journal of the Paleontological Society of India, v. 31, p. 22-25.

Mathur, U. B. and Srivastava, S. (1987), Dinosaur teeth from Lameta Group (Upper Cretaceous) of Kheda District, Gujarat: Journal of the Geological Society of India, v. 29, p. 554–566.

Matley, C. A. (1939), The coprolites of Pisdura, central province: Records of Geological Survey of India, v. 74, p. 535-547.

Matley, C. A. (1924), Note on an armourd dinosaur from the Lameta Beds of Jabbalpore: Records of Geological Survey of India, v. 53, p. 165-169.

Matley, C. E. (1921), Stratigraphy, fossils and geological relationship of the Lameta beds of Jabalpur, M. P: Journal of the Geological Society of India, v. 53, p. 142-169.

Matthew, T. Carrano, Jeffrey, A. Wilson, and Paul, M. Barrett, (2010), The history of dinosaur collecting in central India, 1828-1947: Geological Society of Landon, Special Publication, v. 343, p. 161-173.

Mohabey, D. M. (1996a), Depositional environments of Lameta Formation (Late Cretaceous) of Nand-Dongargaon inland basin, Maharashtra: the fossil and lithological evidences: Memoir, Journal of the Geological Society of India, v. 37, p. 363-386.

Mohabey, D. M. (1996b), A new oospecies *Megaloolithus matleyi* from the Lameta Formation (Upper Cretaceous) of Chandrapur district, Maharashtra, and general remarks on the palaeoenvironmental and nesting behaviour of dinosaurs: Cretaceous Research, v. 17, p. 183-196.

Murkute, Y. A., Deshpande, R. P. And Soman, G. R. (2016) sedimentological studies of Lameta sediments around Nagpur, Central India: Journal of Geosciences Research, v. 1(2). P. 149-163.

Murty, K. N., Rao, R. P., Dhokarikar, B. G. and Varma, C. P. (1963), On the occurrence of plant fossils in Nimar Sandstones near Umrali District, Jhabua, Madhya Pradesh: Current Science, v. 32, p. 21–23.

Pal, A. K. (1971), A note on the biozonation of the Bagh Group of Madhya Pradesh. In: Proceedings of the Fifty Eighth Session of the Indian Science Congress Association. Part III: Abstracts: Indian Science Congress Association, Kolkata, p. 332.

Pascoe, E. H. (1964), Manual of Geology of India and Burma, Vol. III, 3rd ed., Government of India Publication, New Delhi.

Patel, S. J., Shitole, A. D. and Joseph, J. K. (2018), Plug shaped burrows *Conichnus*- *Conostichus* from the Late Cretaceous of Bagh Group, Gujarat, Western India: Journal of the Geological Society of India, v. 91, p. 41-46.

Poddar, M. C. (1964), Mesozoics of western India – their geology and oil possibilities. In: Proceedings of the 22nd Internat. Geological Congress India, Part 1, p. 126–143.

Prasad, G. V. R., Verma, V., Grover, P., Priyadarshini, R., Sahni, A. and Lourembam, R. S. (2016), Isolated Archosaur teeth from the green sandstone capping the Coralline Limestone (Bagh Group) of the Narmada valley: Evidence for the presence of pre-Late to Late Maastrichtian abelisaurids in India: Island Arc, doi: 10.1111/iar.12142.

Prasad, J. N., Patil, S. K., Venkateshwarlu, M., Saraf, P. D., Tripathi, S. C. and Rao, D. R. K. (1998), Palaeomagnetic results from the Cretaceous Bagh Group in the Narmada Basin, central India: evidence of pervasive Deccan demagnetization and its implications for Deccan volcanism: Geophysical

Journal International, v. 133, p. 519-528.

Prasad, V., Stromberg, C. A. E., Leache, A. D., Samant, B., Patnaik, R., Tang, L., Mohabey, D. M., S, Ge. and Sahni, A. (2011) Late Cretaceous origin of the rice tribe provides evidence for early diversification in Poaceae. Nature Communications, doi: 10.1038/ncomms1482.

Racey, A., Fisher, J., Bailey, H. and Roy, S. K. (2016), The value of fieldwork in making connections between onshore outcrops and offshore models: an example from India: In: The value of outcrop studies in reducing subsurface uncertainty and risk in hydrocarbon exploration and production (eds) Bowman, M., Smyth, H. R., Good, T. R., Passey, S. R., Hirst, J. P. P. and Jordan, C. J.: Geological Society of London, Special Publication p. 436, https://doi.org/10.1144/SP436.9.

Ramasamy, S. and Madhavaraju, J. (1993), Petrographic studies of the Bagh Beds along the Narmada Valley in Madhya Pradesh, India: Gondwana Geological Magazine, v. 4/5, p. 65–79.

Rode, K. P. and Chiplonkar, G. W. (1935), A contribution to the stratigraphy of the Bagh Beds: Current Science, v. 2, p. 322–323.

Roy Chowdhary, M. K. and Sastri, V. V. (1962), On the revised classification of the Cretaceous and associated rocks of the Man River section of lower Narbada Valley: Records Geological Survey of India, v. 91, p. 283–301.

Ruidas, D. K., Paul, S. and Gangopadhyay, T. K. (2018), A reappraisal of stratigraphy of Bagh Group of rocks in Dhar District, Madhya Pradesh with an outline of origin of nodularity of Nodular Limestone Formation: Journal of the Geological Society of India, v. 92, p. 19-26.

Saha, O., Shukla, U. K. and Rani, R. (2010), Trace fossils from the Late Cretaceous Lameta Formation, Jabalpur area, Madhya Pradesh: palaeoenvironmental implications: Journal of the Geological Society of India, v. 76 (6), p. 607-620.

Sahni, M. R. and Jain, S. P. (1966), Note on a revised classification of the Bagh Beds, Madhya Pradesh: Journal of the Paleontological Society of India, v. 11, p. 24–25.

Samant, B. and Mohabey, D. M. (2014), Deccan volcanic eruptions and their impact on flora: Palynological evidence: Geological Society of America Special Papers, v. 505, p. 171-191.

Singh, I. B. (1981), Palaeoenvironment and palaeogeography of the Lameta group sediments, Late Cretaceous in Jabalpur area, India: Journal of the Paleontological Society of India, v. 26, p.38-53.

Singh, I. B. and Srivastava, H. K. (1981), Lithostratigraphy of Bagh Beds and its correlations with Lameta beds: Journal of the Paleontological Society of India, v. 26, p. 77-85.

Singh, I. B., Shekhar, S. and Agarwal, S. C. (1983), Palaeoenvironmental and stratigraphic position of Green Sandstone (Lameta: Late Cretaceous) Jabalpur area: Journal of the Geological Society of India, v. 24, p. 412-420.

Shukla, U. K. and Srivastava, R. (2008), Lizard eggs from Upper Cretaceous Lameta Formation of Jabalpur, Central India, with interpretation of depositional environments of the nest-bearing horizon: Cretaceous Research, v. 29 (4), p. 674-686.

Smith, A. B. (2010), The Cretaceous Bagh Formation, India: a Gondwana window on Turonian shallow-water echinoid faunas: Cretaceous Research, v. 31, p. 368–386.

Soman, G. R. and Deshpande, R. P. (1993), Sedimentological studies of Lameta rocks Nagpur district of Maharashtra: In: Recent Researches in Sedimentology (eds) Jhingran, V., Hindustan Publishing Corporation, New Delhi, p. 173-189.

Sonkusare, H., Samant, B. and Mohabey, D. M. (2016), Microflora from Sauropod Coprolites and Associated Sediments of Late Cretaceous (Maastrichtian) Lameta Formation of Nand-Dongargaon Basin, Maharashtra: Journal of the Geological Society of India, v. 89, p. 391-397.

Srivastava, A. K. and Mankar, R. S. (2012), Record of trace fossils from the Lameta successions of Salbardi and Belkher area, district Amravati, Maharashtra and their palaeoecological and palaeoenvironmental significance: Arabian Journal of Geosciences v. 5, p. 1003-1009.

Srivastava, A. K, and Mankar, R. S. (2013), A dinosaurian ulna from a new locality of Lameta succession, Salbardi area, districts Amravati, Maharashtra and Betul, Madhya

Pradesh: Current Science, v. 105 (7), p. 900-901.

Srivastava, A. K, and Mankar, R. S. (2015a), *Megaloolithus* dinosaur nest from the Lameta Formation of Salbardi area, districts Amravati, Maharashtra and Betul, Madhya Pradesh: Journal of the Geological Society of India, v. 85, p. 457-462.

Srivastava, A. K., Mankar, R. S. (2015b), Lithofacies architecture and depositional environment of Late Cretaceous Lameta sediments, Central India: Arabian Journal of Geoscience, v. 8, p. 207-226.

Srivastava, A. K., Kandwal, N. K., Humane, S. K., Humane, S. S., Kundal, P. and Khare, N. (2018), Record of calcareous algae from the Lameta Formation: a new insight for possible sea incursion during the Maastrichtian time: Arabian Journal of Geoscience, https://doi.org/10.1007/s12517-017-3333-1.

Srivastava, R., Patnaik, R., Shukla, U. K. and Sahni, A. (2015), Crocodilian nest in a Late Cretaceous sauropod hatchery from the type Lameta Ghat locality, Jabalpur, India: PloS ONE 10(12): e0144369.

Tandon, S. K. and Andrews, J. E. (2001), Lithofacies associations and stable isotopes of palustrine and calcrete carbonates: examples from an India Maastrichtian regolith. Sedimentology, v. 48, p. 339-355.

Tandon, S. K., Andrews, J. E. and Dennis, P. F. (1995), Palaeoenvironments of dinosaur bearing Lameta beds (Maastrichtian), Narmada valley, Central India: Palaeogeography, Palaeoclimatology, Palaeoecology, v. 117, p. 153-184.

Tandon, S. K., Andrews, J. E., Sood, A. and Mittal, S. (1998), Shrinkage and sediments supply of multiple calcrete profile development: a case study from the Maastrichtian of Central India: Sedimentary Geology, v. 119, p. 25-45.

Tandon, S. K., Verma, V. K., Jhingran, V., Sood, A., Kumar, S., Kohli, R. P. and Mittal, S. (1990), The Lameta Beds of Jabalpur, Central India: deposits of fluvial and pedogenically modified semi-arid pre-palustrine flat systems. In: Sahni, A., Jolly, A. (eds.), Cretaceous Event Stratigraphy and the Correlation of the Indian Non-marine Strata: Contribution, Symposium-cum Workshop, ICGP-216 and 245, Chandigarh, p. 75-77.

Taylor, P. D. and Badve, R. M. (1995), A new cheilostome bryozoan from the Cretaceous of India and Europe: a cyclostome homeomorph: Palaeontology, v. 38, p. 627–657.

Tripathi, S. C. (1995), Palaeontological and palaeoenvironmental studies of Bagh Group, Madhya Pradesh: Records of the Geological Survey of India, v. 128, p. 104–105.

Tripathi, S. C. (2006), Geology and evolution of the Cretaceous Infratrappean Basins of Lower Narmada Valley, western India: Journal Geological Society of India, v. 67, p.459-468**.**

Vaidyanadhnan, R. and Ramakrishan, A. (2008), Geology of India, Vol II. Geological Society of India Publication, Banglore, p.557-994.

Vianey-Liaud, M., Khosla, A. and Garcia, G. (2003), Relationships between European and Indian dinosaur eggs and eggshells of the oofamily Megaloolithidae: Journal of Vertebrate Palaeontology v. 23, p. 575-585.

Wilson, J. A., Sereno, P. C., Srivastava, S., Batt, D. K., Khosla, A. and Sahni, A. (2003), A new Abelisaurid (Dinosauria-Sauropoda) from the Lameta Formation (Cretaceous: Maastrichtian) of India: Contributions from the Museum of Palaeontology, University of Michigan, 31(1), 1-42.

Wilson, J. A. and Upchurch, P. (2003), A revision of *Titanosaurus lydekker* (Dinosauria-Sauropoda), the first dinosaur genus with Gondwana distribution: Journal of Systematic Palaeontology, v. 1(3), p. 125-160.

Wright, V. P. (1992), A revised classification of limestones: Sedimentary Geology, v. 76, p. 177-185.

Wright, V. P. and Tucker, M. E. (1991), Calcretes: an introduction. In: Wright, V. P., Tucker, M. E. (eds.), Calcretes: IAS Reprint series 2. Blackwell, Oxford, p. 1-22.

Jour. Indian Association of Sedimentologists, Vol. 36, No. 2 (2019), pp.64-85
ISSN Online 2582 – 2020
ISSN Print 0970 – 3268

Heavy Mineral Distribution and Provenance Studies of Coastal Sediments of Visakhapatnam Coast – Statistical Approach

G. Appa Rao and T. Karuna Karudu
Delta Studies Institute, Andhra University, Visakhapatnam - 530 017
E-mail: apparao.gundabattula@gmail.com

Abstract: The present work aims to address the heavy mineral studies of coastal sediments. There are three different environments that are studied in the present investigation. They include beach sediments from VUDA Park to Bheemili, coastal red sediments at INS Kalinga area and sediments from Gosthani estuary sub-environments. The interpretation of heavy mineral data sets indicates that the nature and presence of similar heavy mineral assemblage in a beach sub-environments, coastal red sediments, and Gosthani estuary sub-environments suggests that the study area heavy minerals have been derived from the same source of lithologies. The heavy mineral assemblages and their concentrations of heavy minerals in different sub-environments of coastal sediments are derived mainly from metamorphic suite of rocks i.e., Eastern Ghats group of rocks of khondalites and charnockites etc.

The results of the cluster analysis have clearly brought about the importance of variations in the heavy mineral percentages in forming clusters. Application of cluster analysis on the heavy minerals variations resulted in two main clusters. Cluster-1 consists of nine sub-clusters and cluster-2 consists of eight sub-clusters. Beach environment and Gosthani estuary sediments fall under the cluster-1 category. The predominance of coastal red sediments is fall under the cluster-2 category. The clusters and sub-clusters have certain distinct characteristics which make them different from others and hence they have formed separate groups.

Keywords: Heavy minerals, Coastal red sediments, Beach Sands, Gosthani Estuary sediments, Cluster analysis.

INTRODUCTION

The coastline of Andhra Pradesh is situated on the Southeast coast of Indian Peninsula with waters of Bay of Bengal and length of the coastline is 974 kilometers. The coastline endowed with huge recent sediments. These have been attracting the attention of geologists for research in many aspects. The coastal region contains heavy minerals like ilmenite, magnetite, garnet, sillimanite, rutile, zircon, monazite and epidote etc. Each heavy mineral grain is a unique messenger of coded data, carrying the detail of its ancestry and the vicissitudes of its sedimentary history (Maria and David, 2007). The study area situated between the Latitudes 17° 72' and 17° 89' N, Longitudes 83° 34' and 83° 45' E, and covers beach sediments from VUDA park to Bheemili, coastal red sediments at INS Kalinga area and Gosthani estuary sub-environments. The location map of the study area is given in Fig. 1. The geological formations of the study area belong to Archean and Quaternary periods. The Archean rocks comprise mainly khondalites, charnockites, leptynites, pegmatites and quartz veins. Quaternary sediments include laterite and surficial soils and coastal sand deposits.

The coastal red sediments with bad land topography and an area comprising deeply gullied nature abundantly occur near to the INS Kalinga area. It is bounded by streams Chittigadda in the North-West and Peddagadda in the South-West. These sediments are in general loosely packed and are separated from the sea by the modern beach and dune sands. During the Holocene period the heavy winds blown particularly during the monsoon period lot of sediment blown to the interior of the present coast to the edge of Eastern Ghats. This activity promotes the accumulation of huge sands and later the sands became as coastal red sediments. Today, the coastal red sediments are one of the only three such existing formations in South East Asia, the other two being in Tamil Nadu (Teri Sands), India, and Sri Lanka. The rare natural wonder near INS Kalinga area, which took lot of time to produce these sediments, is about 10 km^2 from the backshore zone to 2.5 km inland and elevation is up to 90 m above Mean Sea Level (MSL). Nature, the great artist has gifted these sublimely beautiful formations. They are geologically important and are classified as "Heritage" since they hold prominent features of geological history of the late Quaternary period and carry the imprints of the fall of sea level and its subsequent rise, the impact of climate, and geological processes of the sediments. That is why it is even more important that these coastal red sediments must be preserved in its original form for future generations to understand the myths of nature. In July 2014, this unique natural heritage site was declared a "Scientifically significant Geo-heritage site" by the Geological Survey of India (GSI), following the efforts of the Geo-Heritage Cell of INTACH (Indian National Trust for Art and Cultural Heritage).

The Gosthani River is an East-flowing river which flows across the southern India state of Andhra Pradesh. This river originates from the Ananthagiri Hills at Borra caves region which is situated in the Eastern Ghats and eventually flows into the Bay of Bengal, forming an estuary at Bheemunipatnam. The river follows a dendritic pattern. This river basin is a tiny one which occupies an area measuring about 2000 km^2. A major portion of this basin is covered the Eastern Ghat rocks. Gosthani River is fed by rainfalls and it is said to enjoy about 110 cm of rainfall, which arrives from the Southwest monsoon. The Gosthani estuary situated 30 km North of Visakhapatnam city on the East coast of India. The estuary includes different sub-environments of swash bar, barrier bar, estuary bar and back barrier etc. has been included in the present study.

PREVIOUS WORK AND OBJECTIVE OF THE STUDY

Several workers have been made to their attempts to study the heavy minerals occurrences along the East Coast of India. The monazite and other black sand concentrations of heavy minerals at Bay of Bengal Coast have been described by Mahadevan and Sriramdas (1948), Mahadevan and Nateswararao (1950) and Sriramdas (1951). In the East Coast, heavy mineral variation in the delta and shelf sediments between Visakhapatnam and the Penner River was reported by Mallik (1968). Detailed studies of zircons in the beach sands along East Coast of India have been made (Venkataratnam and Rao, 1968). Concentration of garnet in the sands along Visakhapatnam-Bheemunipatnam Coast was reported by Sastry, et. al., (1981, 1987) have reported the energy conditions and heavy mineral concentration along Visakhapatnam-Bheemunipatnam Coast and Ramamohana Rao, et al., (1982) have reported the occurrence of thin layers of black sand in the inland stream channels along Visakhapatnam-Bheemunipatnam Coastal areas. In Kalingapatnam-Baruva Coast, cheralite was reported by Reddy and Prasad (1997) and heavy mineral distributions in different size fractions and variables were also explained by Reddy and Prasad, (1998). Rajasekhara Reddy, et al., (2009a & 2009b) studied the heavy mineral distribution in different distributaries of the Mahanadi delta of the East Coast of India. Murali Krishna, et al., (2016) studied heavy mineral distribution in Coastal red sediments of Bhimunipatnam. Rajasekhar Reddy (1990) applied cluster analysis to heavy mineral data of shelf sediments off cannanore-Calicut, West coast of India.

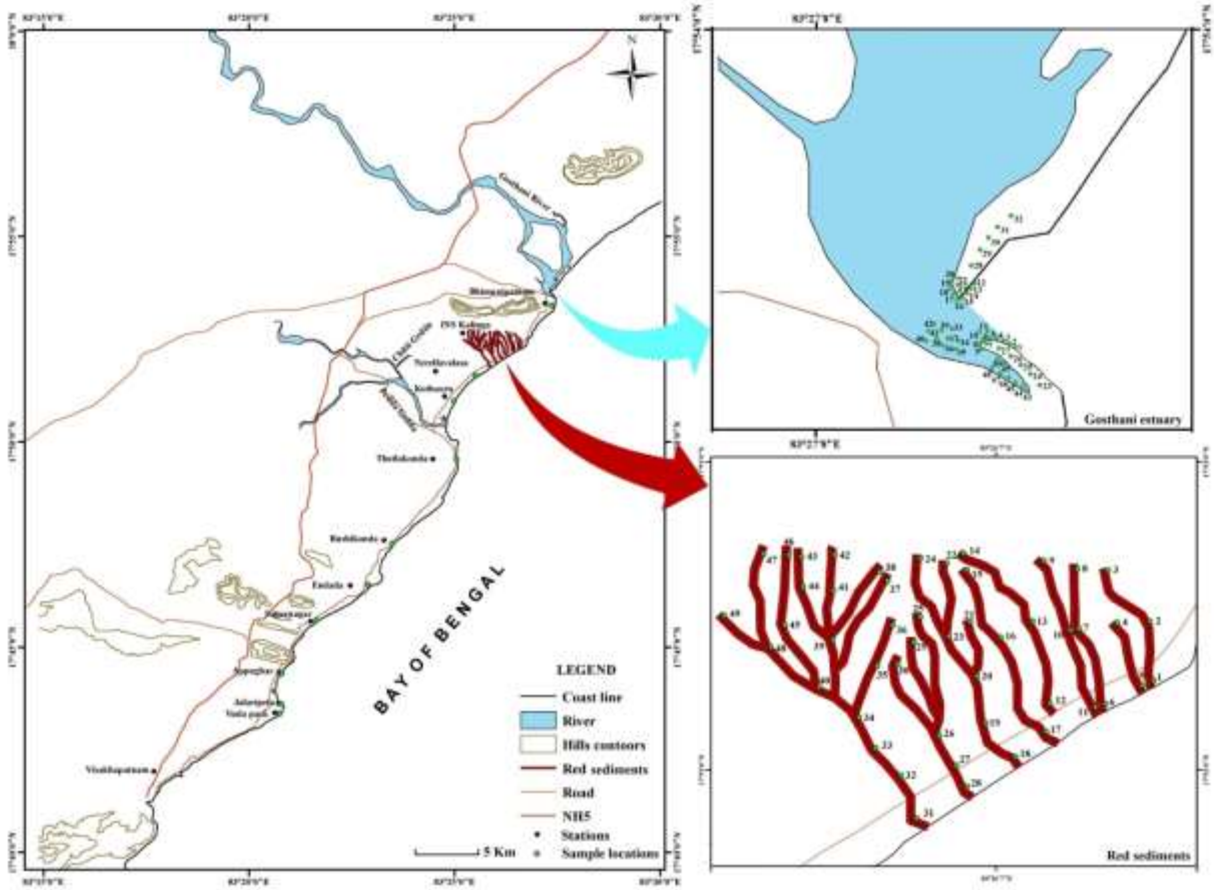

Figure 1: Sample location of the study area.

Karuna karudu (2012) applied cluster analysis to heavy mineral data of different sub-environments of Mahanadi delta, East Coast of India. The present paper is the continuation of this work and deals with the results of detailed studies, carried out on heavy mineral studies in order to throw light on the provenance.

METHODOLOGY

A total of ninety-six sediment samples were used for heavy mineral analysis, in which twenty-nine sediment samples from beach environments, forty-nine sediment samples from coastal red sediments and eighteen sediment samples from Gosthani estuary sub-environments. The following procedure has been adopted for heavy mineral analysis. The samples were thoroughly washed through 230 ASTM mesh sieve with water to remove clay and silt material. The washed samples were treated with a few ml of dilute hydrochloric acid to remove any carbonate shell. The addition of small amount of stannous chloride accelerates the removal of the iron coating. Then the samples were dried and sieved into three ASTM size fractions viz. +60 (+0.25 mm), -60 to +120 (-0.25 to +0.125 mm) and -120 to +230 (-

0.125 to +0.063 mm). Heavy minerals from the sand fractions have been separated using bromoform (sp. gr. 2.89). After separation, the heavy and light fractions were weighed and their weight percentages were calculated. The heavies were mounted on a glass slide with Canada balsam. About 300-400 grains in each slide were identified using by petrological microscope and counted for determination of individual number percentages and nature, origin, and distribution of heavy mineral of coastal sediments were interpreted. Cluster analysis is done using Statistica software.

RESULTS AND DISCUSSION

Range and average values of heavy mineral composition by weight percentage of different sub-environments of coastal sediments in +60, +120 and +230 fractions are present in table 1. Cluster analysis is carried out on the heavy mineral data of beach environment (foreshore, backshore, and dune), coastal red sediments and Gosthani estuary sediments (swash bar, barrier bar, estuary bar and back barrier) are presented in table 2 and Average heavy mineral percentages of different clusters are present in table 3.

+60 Fraction								
Environment	**Range**	**Sillimanite**	**Garnet**	**Epidote**	**Zircon**	**Monazite**	**Rutile**	**Opaques**
Foreshore	Min.	10.79	11.65	0.57	0.00	0.85	0.50	28.43
	Max.	44.49	38.63	1.32	1.84	10.82	13.31	55.67
	Av.	24.66	26.75	0.88	1.29	3.66	3.21	38.34
Backshore	Min.	10.60	20.87	1.13	1.58	0.78	0.00	14.35
	Max.	50.92	49.25	3.20	7.62	12.10	2.81	35.17
	Av.	32.01	29.16	1.76	3.64	4.67	1.70	25.38
Dune	Min.	8.13	24.62	0.45	1.20	0.00	0.00	15.08
	Max.	35.48	46.92	2.60	9.18	9.31	8.35	43.83
	Av.	22.56	34.09	1.52	4.37	3.40	4.01	27.98
Coastal red sediments	Min.	2.24	0.00	0.00	0.00	0.00	0.00	27.67
	Max.	70.26	2.97	0.00	4.97	8.58	3.03	88.34
	Av.	20.70	0.19	0.00	1.55	1.14	0.30	69.22
Swash bar	Min.	3.93	10.21	0.07	0.00	0.00	0.00	33.83
	Max.	36.08	31.26	1.55	2.01	2.99	2.45	74.64
	Av.	18.21	22.23	0.72	0.69	1.07	1.11	51.76
Barrier bar	Min.	8.22	13.12	0.49	0.13	1.34	0.80	55.05
	Max.	14.78	23.02	1.18	1.66	2.36	1.43	71.81
	Av.	10.78	16.75	0.72	0.97	1.81	1.11	65.97

Estuary bar	Min.	14.77	17.82	0.46	0.41	0.93	0.56	33.84
	Max.	25.80	26.94	1.29	1.24	1.56	0.98	62.16
	Av.	21.08	22.82	0.84	0.94	1.17	0.82	47.61
Back barrier	Min.	18.45	14.88	1.07	0.06	0.05	0.04	39.61
	Max.	23.81	25.30	1.32	1.61	1.40	1.13	48.94
	Av.	21.42	19.27	1.22	0.58	0.50	0.42	44.38
+120 Fraction								
Foreshore	Min.	9.84	7.19	0.63	0.85	0.83	0.54	29.99
	Max.	47.61	43.29	1.56	3.15	10.82	13.31	55.67
	Av.	25.17	22.18	1.13	1.62	3.51	3.11	42.45
Backshore	Min.	14.35	1.97	1.32	1.74	0.86	0.48	22.04
	Max.	35.51	34.09	2.17	7.62	11.08	8.35	62.28
	Av.	29.00	16.04	1.70	3.36	3.63	3.80	41.01
Dune	Min.	24.17	13.12	1.57	1.76	0.84	0.59	15.08
	Max.	43.83	38.77	2.35	9.18	9.31	2.81	44.93
	Av.	31.58	25.55	1.89	4.35	3.54	1.55	29.84
Coastal red sediments	Min.	0.00	0.00	0.00	0.00	0.00	0.00	37.63
	Max.	32.77	6.46	0.00	4.57	7.99	2.10	88.57
	Av.	15.65	0.24	0.00	1.85	1.88	0.64	74.73
Swash bar	Min.	4.57	10.62	0.37	0.36	0.12	0.77	30.24
	Max.	49.21	22.11	3.23	3.55	2.72	3.21	74.95
	Av.	19.97	16.85	0.89	1.46	1.33	1.80	54.97
Barrier bar	Min.	5.30	4.49	0.40	1.88	1.93	1.50	70.28
	Max.	8.49	11.71	1.11	3.03	4.31	2.10	80.02
	Av.	7.01	9.25	0.71	2.60	3.23	1.87	73.64
Estuary bar	Min.	4.99	7.49	0.20	1.31	1.88	1.97	52.28
	Max.	16.94	19.40	1.28	4.15	2.13	3.62	80.57
	Av.	12.74	13.86	0.71	2.46	2.00	2.65	64.02
Back barrier	Min.	23.99	16.44	0.41	0.22	0.19	0.42	40.09
	Max.	29.86	25.95	1.04	0.64	0.84	0.90	50.22
	Av.	27.57	20.27	0.76	0.41	0.43	0.73	45.94
+230 Fraction								
Foreshore	Min.	0.00	0.00	0.00	0.00	0.00	0.00	0.00
	Max.	14.72	7.44	1.37	5.05	0.52	0.68	99.13
	Av.	5.17	3.41	0.48	1.19	0.10	0.26	77.66
Backshore	Min.	0.00	0.00	0.00	0.00	0.00	0.00	0.00
	Max.	16.69	5.74	1.39	4.78	1.09	1.10	89.90
	Av.	5.48	1.71	0.55	1.44	0.30	0.33	55.88
Dune	Min.	0.39	0.35	0.00	0.56	0.00	0.00	84.23

	Max.	6.65	6.41	0.55	4.91	0.52	1.19	91.34
	Av.	2.97	2.88	0.09	2.54	0.13	0.64	88.94
Coastal red sediments	Min.	0.00	0.00	0.00	0.00	0.00	0.00	0.00
	Max.	21.19	3.21	0.00	5.60	4.51	1.36	90.48
	Av.	5.75	0.13	0.00	1.34	1.22	0.30	42.45
Swash bar	Min.	2.59	3.81	0.00	0.00	0.00	0.00	35.85
	Max.	25.17	41.86	2.71	9.20	5.71	3.52	79.68
	Av.	12.06	17.20	0.82	2.16	1.79	1.58	59.93
Barrier bar	Min.	2.00	4.10	0.12	1.56	5.22	0.81	76.89
	Max.	2.69	4.47	0.66	6.73	6.01	2.28	83.43
	Av.	2.44	4.26	0.33	4.99	5.53	1.76	79.43
Estuary bar	Min.	4.43	4.81	0.44	3.16	1.59	1.08	59.20
	Max.	7.09	8.00	0.91	5.96	3.41	2.30	77.51
	Av.	5.40	6.78	0.66	4.51	2.72	1.74	70.98
Back barrier	Min.	20.15	16.13	0.32	0.28	1.00	0.83	36.69
	Max.	25.58	18.35	2.16	1.56	1.75	1.67	54.64
	Av.	23.37	17.02	1.53	0.76	1.30	1.16	43.20

Table 1: Range and average values of heavy mineral composition by weight percentage of different sub-environments of coastal sediments in +60, +120 and +230 fractions.

Description and distribution pattern of individual heavy minerals of fraction wise variations of different sub-environments.

Sillimanite: The sillimanite grains in the present study area are found as prismatic and acicular in nature, and these grains are showing perfect cleavage, elongated, angular edges sometimes rounded at termination. They show moderate relief, non-pleochroic and straight extinction.

In **+60** fraction (Table 1), the concentration of sillimanite is higher in backshore with range 10.60 to 50.92 %, av. 32.01 % then in foreshore with range 10.79 to 44.49 %, av. 24.66 %, dune with range 8.13 to 35.48 %, av. 22.56 %, back barrier with range 18.45 to 23.81 %, av. 21.42 %, estuary bar with range 14.77 to 25.80 %, av. 21.08 %, coastal red sediments with range 2.24 to 70.26 %, av. 20.70 %, swash bar with range 3.93 to 36.0 %, av. 18.21 %, barrier bar with range 8.22 to 14.78 %, av.10.78 %.

In **+120** fraction (Table 1), the concentration of sillimanite are higher in dune with range 24.17 to 43.83 %, av. 31.58 % then in backshore with range 14.35 to 35.51 %, av. 29.00 %, back barrier with range 23.99 to 29.86 %, av. 27.57 %, foreshore with range 9.84 to 47.61 %, av.

25.17 %, swash bar with range 4.57 to 49.21 %, av. 19.97 %, coastal red sediments with range 0 to 32.77 %, av.15.65 %, estuary bar with range 4.99 to 16.94%, av.12.74%, barrier bar with range 5.30 to 8.49 %, av. 7.01 %.

In **+230** fraction (Table 1), the concentration of sillimanite are higher in back barrier with range 20.15 to 25.58 %, av. 23.37 % then in swash bar with range 2.59 to 25.17 %, av. 12.06 %, coastal red sediments with range 0 to 21.19 %, av.5.75 %, backshore with range 0 to 16.69 %, av.5.48 %, estuary bar with range 4.43 to 7.09 %, av.5.40 %, foreshore with range 0 to 14.72 %, av.5.17 %, dune with range 0.39 to 6.65 %, av.2.97 %, barrier bar with range 2 to 2.69 %, av.2.44 %.

Garnet: Garnet grains are generally pale pink in colour and the shape of the garnets is rounded or sub-rounded and occasionally sub-spherical. They are usually identified by their high relief, isotropic nature and inclusions of iron oxides are seen occasionally

In **+60** fraction (Table 1), the concentrations of garnet are higher in dune with range 24.2 to 46.92 %, av. 34.09 % then in backshore with range 20.87 to 49.25 %, av. 29.16 %, foreshore with range 11.65 to 38.63 %, av.26.75 %, estuary bar with range 17.82 to 26.94 %, av. 22.82 %, swash bar with range 10.21 to 32.26 %, av. 22.23 %, back barrier with range 14.88 to 25.30 %, av.19.27 %, barrier bar with range 13.12 to 23.02 %, av.16.75 %, coastal red sediments with range 0 to 2.97 %, av. 0.19 %.

In **+120** fraction (Table 1), the concentration of garnet are higher in dune with range 13.12 to 38.77 %, av. 25.55 % then in foreshore with range 7.19 to 43.29 %, av. 22.18 %, back barrier with range 16.44 to 25.95 %, av. 20.27 %, swash bar with range 10.62 to 22.11 %, av. 16.85 %, backshore with range 1.97 to 34.09 %, av.16.04 %, estuary bar with range 7.49 to 19.40 %, av. 13.86 %, barrier bar with range 4.49 to 11.71%, av. 9.25%, coastal red sediments with range 0 to 6.46 %, av. 0.24 %.

In **+230** fraction (Table 1) the concentration of garnet are higher in swash bar with range 3.81 to 41.86 %, av. 17.20 %, then in back barrier with range 16.13 to 18.35 %, av. 17.02 %, estuary bar with range 4.81 to 8.00 %, av. 6.78 %, barrier bar with range 4.10 to 4.47 %, av. 4.26 %, foreshore with range 0 to 7.7.44 %, av. 3.41 %, dune with range 0.35 to 6.41 %, av. 2.88 %, backshore with range 0 to 5.74 %, av. 1.71 %, coastal red sediments with range 0 to 3.21 %, av. 0.13%.

Epidote: Epidote is also one of the minor constituents of heavy minerals. Most of the grains are in colourless and some are yellow, greenish in colour with subrounded in shape and they show pleochroism.

In **+60** fraction (Table 1), the concentration of epidote are higher in backshore with range 1.13 to 3.20 %, av. 1.76 % then in dune with range 0.45 to 2.60 %, av. 1.52 %, back barrier with range 1.07 to 1.32 %, av. 1.22 %, foreshore with range 0.57 to 1.32 %, av. 0.88 %, estuary bar with range 0.46 to 1.29 %, av. 0.84 %, swash bar with range 0.07 to 1.55%, av. 0.72 %, barrier bar with range 0.49 to 1.88 % av. 0.72 %.

In **+120** fraction (Table 1), the concentration of epidote are higher in dune with range 1.57 to 2.35 %, av. 1.89 % then in backshore with range 1.32 to 2.17 %, av. 1.70 %, foreshore with range 0.63 to 1.56 %, av. 1.13 %, swash bar with range 0.37 to 3.23 %, av. 0.89 %, back barrier with range 0.41 to 1.04 %, av. 0.76 %, estuary bar with range 0.20 to 1.28 %, av. 0.71 %, barrier bar with range 0.40 to 1.11%, av. 0.71 % .

In **+230** fraction (Table 1), the concentration of epidote are higher in back barrier with range 0.32 to 2.16 %, av. 1.53 % then in swash bar with range 0 to 2.71 %, av. 0.82 %, estuary bar with range 0.44 to 0.91 %, av. 0.66 %, backshore with range 0 to 1.39 %, av. 0.55 %, foreshore with range 0 to 1.37 %, av. 0.48 %, barrier bar with range 0.12 to 0.66 %, av. 0.33 %, dune with range 0 to 0.55 %, av. 0.09 %.

Zircon: Morphologically zircon grains varies from sharp euhedral crystals through prismatic and anhedral fragments, grains with gently rounded terminations to well-rounded forms and complete spheres sometimes. In the present study, most of the zircon grains are rounded and subrounded with thick borders and colourless, but a few shows yellowish colour. The refractive index is fairly high, strong birefringence and uniaxial positive. Zoning is a characteristic feature of these grains.

In **+60** fraction (Table 1), the concentration of zircon are higher in dune with range 1.20 to 9.18 %, av. 4.37 % then in backshore with range 1.58 to 7.62 %, av. 3.64 %, coastal red sediments with range 0 to 4.97 %, av. 1.55 %, foreshore with range 0 to 1.84 %, av. 1.29 %, barrier bar with range 0.13 to 1.66 %, av. 0.97 %, estuary bar with range 0.41 to 1.24 %, av. 0.94 %, swash bar with range 0 to 2.01 %, av. 0.69 %, back barrier with range 0.06 to 1.61 %, av. 0.58 %.

In **+120** fraction (Table 1), the concentration of zircon are higher in dune with range 1.76 to 9.18 %, av. 4.35 % then in backshore with range 1.74 to 7.62 %, av. 3.36 %, barrier bar with range 1.88 to 3.03 %, av. 2.60 %, estuary bar with range 1.31 to 4.15 %, av. 2.46 %, coastal red sediments with range 0 to 4.57 %, av. 1.85 %, foreshore with range 0.85 to 3.15 %, av.

1.62 %, swash bar with range 0.36 to 3.55 %, av. 1.46 %, back barrier with range 0.22 to 0.64 %, av. 0.41 %.

In **+230** fraction (Table 1), the concentration of zircon are higher in barrier bar with range 1.56 to 6.76 %, av. 4.99 % then in estuary bar with range 3.16 to 5.96 %, av. 4.51 %, dune with range 0.56 to 4.91 %, av. 2.54 %, in swash bar with range 0 to 9.20 %, av. 2.16 %, backshore with range 0 to 4.78 %, av. 1.44 %, coastal red sediments with range 0 to 5.60 %, av. 1.34 %, foreshore with range 0 to 5.05%, av. 1.19 %, back barrier with range 0.28 to 1.56 %, av. 0.76 %.

Monazite: The most of the monazite grains are rounded. The light yellow colour is the characteristic property of this mineral. They show high relief with distinct borders. A few grains are faintly pleochroic with moderate birefringence.

In **+60** fraction (Table 1), the concentration of monazite are higher in backshore with range 0.78 to 12.10 %, av. 4.67 % then in foreshore with range 0.85 to 10.82 %, av. 3.66 %, dune with range 0 to 9.31 %, av. 3.40 %, in barrier bar with range 1.34 to 2.36 %, av. 1.81 %, estuary bar with range 0.93 to 1.56 %, av. 1.17 %, coastal red sediments with range 0 to 8.58 %, av. 1.14 %, swash bar with range 0 to 2.99 %, av. 1.07%, back barrier with range 0.05 to 1.40 %, av. 0.50 %.

In **+120** fraction (Table 1) the concentration of monazite are higher in backshore with range 0.86 to 11.08 %, av. 3.63 % then in dune with range 0.84 to 9.31 %, av. 3.54 %, foreshore with range 0.83 to 10.82 %, av. 3.51 %, barrier bar with range 1.93 to 4.31 %, av. 3.23 %, estuary bar with range 1.88 to 2.13 %, av. 2.00 %, coastal red sediments with range 0 to 7.99 %, av. 1.88 %, swash bar with range 0.12 to 2.72 %, av. 1.33 %, back barrier with range 0.19 to 0.84 %, av. 0.43 %.

In **+230** fraction (Table 1), the concentration of monazite are higher in barrier bar with range 5.22 to 6.01 %, av. 5.53 % then in estuary bar with range 1.59 to 3.41 %, av. 2.72 %, swash bar with range 0 to 5.71 %, av. 1.79 %, back barrier with range 1.00 to 1.75 %, av. 1.30 %, coastal red sediments with range 0 to 4.51 %, av. 1.22 %, back shore with range 0 to 1.09 %, av. 0.30 %, dune with range 0 to 0.52 %, av. 0.13 %, foreshore with range 0 to 0.52 %, av. 0.10 %.

Rutile: Most of the rutile grains are shades of red, such as deep blood red and brownish red in colour, showing prismatic and pyramidal terminations. In some samples grains showing irregular or conchoidal breakage patterns. 'Knee-shaped' twins and parallel crystal growths are encountered in some samples. They show high relief, deep colours, pleochroic and straight extinction.

In **+60** fraction (Table 1), the concentration of rutile are higher in dune with range 0 to 8.35 %, av. 4.01 % then in foreshore with range 0.50 to 13.31 %, av. 3.21 %, backshore with range 0 to 2.81 %, av. 1.70 %, swash bar with range 0 to 2.45 %, av. 1.11 %, barrier bar with range 0.80 to 1.43 %, av. 1.11 %, estuary bar with range 0.56 to 0.98 %, av. 0.82 %, back barrier with range 0.04 to 1.13 %, av. 0.42 %, coastal red sediments with range 0 to 3.03 %, av. 0.30 %.

In **+120** fraction (Table 1), the concentration of rutile are higher in backshore with range 0.48 to 8.35 %, av. 3.80 % then in foreshore with range 0.54 to 13.31 %, av. 3.11 %, estuary bar with range1.97 to 3.62 %, av.2.65 %, barrier bar with range 1.50 to 2.10 %, av. 1.87 %, swash bar with range 0.77 to 3.21 %, av. 1.80 %, dune with range 0.59 to 2.81 %, av. 1.55 %, back barrier with range 0.42 to 0.90 %, av. 0.73 %, coastal red sediments with range 0 to 2.10 %, av. 0.64 %.

In **+230** fraction (Table 1), the concentration of rutile are higher in barrier bar with range 0.81 to 2.28 %, av. 1.76 % then in estuary bar with range 1.08 to 2.30 %, av. 1.74 %, swash bar with range 0 to 3.52 %, av. 1.58 %, in back barrier with range 0.83 to 1.67 %, av. 1.16 %, dune with range 0 to 1.19 %, av. 0.64 %, back shore with range 0 to 1.10 %, av. 0.33 %, coastal red sediments with range 0 to 0.36 %, av. 0.30 %, foreshore with range 0 to 0.68 %, av. 0.26 %.

Opaques: The opaques consist of magnetite and ilmenite, the ilmenite being dominant. Opaques are present in a good proportion and are rounded, subrounded and sub-angular in the shape and black in colour. It has been observed that a few grains show a dull grey luster in patches, under the reflected light ilmenite will look like its altered product leucoxene.

In **+60** fraction (Table 1), the concentration of opaques are higher in coastal red sediments with range 27.67 to 88.34 %, av. 69.22 % then in barrier bar with range 55.05 to 71.81 %, av. 65.97 %, swash bar with range 33.83 to 74.64 %, av. 51.76 %, estuary bar with range 33.84 to 62.16 %, av. 47.61 %, back barrier with range 39.61 to 48.94 %, av. 44.38 %, foreshore with range 28.43 to 55.67 %, av. 38.34 %, dune with range 15.08 to 43.83 %, av. 27.98 %, backshore with range 14.35 to 35.17 %, av. 25.38 %.

In **+120** fraction (Table 1), the concentration of opaques are higher in coastal red sediments with range 37.63 to 88.57 %, av. 74.73 % compared to barrier bar with range 70.28 to 80.02 %, av. 73.64 %, in estuary bar with range 52.28 to 80.57 %, av. 64.02 %, in swash bar with range 30.24 to 74.95 %, av. 54.97 %, in back barrier with range 40.09 to 50.22 %, av. 45.94 %, in foreshore with range 29.99 to

55.67 %, av. 42.45 %, in backshore with range 22.04 to 62.28 %, av. 41.01 %, in dune with range 15.08 to 44.93 %, av. 29.84 %.

In **+230** fraction (Table 1), the concentration of opaques are higher in dune with range 84.23 to 91.34 %, av. 88.94 % then in barrier bar with range 76.89 to 83.43 %, av. 79.43 %, foreshore with range 0 to 99.13 %, av. 77.66 %, in estuary bar with range 59.20 to 77.51 %, av. 70.98 %, swash bar with range 35.85 to 79.68 %, av. 59.93 %, back shore with range 0 to 89.90 %, av. 55.88 %, back barrier with range 36.69 to 54.64 %, av. 43.20 %, coastal red sediments with range 0 to 90.48 %, av. 42.45 %.

Heavy mineral distribution in different sub-environments of Beach environment, Coastal red sediments and Gosthani estuary sub-environments:

Beach environment: Sillimanite, Monazite and Rutile are abundant in coarse (+60), medium (+120) size fractions and show decrease towards fine size (+230) in foreshore, backshore and dune. Opaques are concentrated more in finer fraction (+230) than in the coarser (+60), medium (+120) fractions and increasing gradually from <+60 to +230 in beach environments. Epidote and zircon are concentrated more in coarse size (+60) and medium size (+120) than in the finer fraction and decrease gradually from <+60 to +230 in backshore and dune whereas epidote and zircon are concentrated more in fine fraction (+230 ASTM) and increasing gradually from <+60 to +230 ASTM in foreshore sediments.

Coastal red sediments: Sillimanite, Monazite and Rutile are concentrated more in coarse fraction (+60), than in the finer fraction (+230) and decreases gradually from <+60 to +230. Opaques are concentrated more in finer fraction (+230) than in the coarser fraction and increases gradually from <+60 to +230.

The garnet concentrations are low in coastal red sediments compared to beach and Gosthani sub-environments and the grains of garnets are insignificant and found to be occurring in highly altered state and show leached and pitted surfaces, which indicates that garnets might have been undergone chemical decomposition under acidic conditions which led to produce iron oxides (Hematite) causes for red colorization of the sediment. The stability of members of the garnet group varies according to their chemistry. Dana, (1985) and Allen, (1948) observed that garnets with high ferrous iron content were particularly prone to disintegration in their investigation.

Gosthani estuary sub-environments: Garnets are concentrated more in coarse fraction (+60), than in the fine fraction (+230) in barrier bar, estuary bar and back barrier and in swash bar concentration more in (+230) fraction compared to coarse fraction (+60). Sillimanite concentration more in (+60) fraction than in the finer fraction (+230) in swash bar, barrier bar and estuary bar. Zircons are concentrated more in finer fractions (+230) than in the coarser fraction and increases gradually from <+60 to +230 in swash bar, barrier bar and estuary bar. Opaques are concentrated more in finer fraction (+230) than in coarse fraction and increases gradually from <+60 to +230 in swash bar, barrier bar and back barrier. Monazite and rutile are concentrated more in (+230) fraction compared to other fractions in swash bar, barrier bar and back barrier.

CLUSTER ANALYSIS OF HEAVY MINERAL DATA

'Cluster' is "a number of things of the same kind growing or joined together', or a group of homogeneous things. The term cluster analysis was first used by (Tryon, 1939) actually, encompasses a number of different classification algorithms. According to Kaufman and Rousseeuw (2005) objects in the same group are similar to each other and objects in different groups are as dissimilar as possible. The use of cluster methods has increased dramatically in the last 30 years, nowadays clustering methods are applied in many domains, including artificial intelligence and pattern recognition, ecology, economics, the geosciences, and much more. Clustering methods are useful whenever the researcher is interested in grouping together objects based on multivariate similarity.

The heavy minerals considered for the present study are sillimanite, garnet, epidote, zircon, monazite, rutile, opaques. The results of cluster analysis show that there are two major clusters. Cluster-1 contains nine sub-clusters and cluster-2 contains eight sub-clusters. The clusters and sub-clusters have certain distinct characteristics which make them different from others and hence they have formed separate groups.

Cluster-1: Beach environments (foreshore, backshore, and dune) and Gosthani estuary sediments (swash bar, barrier bar, estuary bar and back barrier) are falls under the cluster-1 category. The average heavy mineral percentages of different clusters are presented in table 3. The cluster-1 is characterized by high opaques, sillimanite, and garnet. Within the cluster-1 there are nine sub-clusters. Sillimanite percentage is low at sub cluster-1G and high at sub cluster-1A; garnet percentage is low at sub cluster-1H and high at sub cluster-1I; epidote percentage is low at sub cluster-1G and high at sub cluster-1C; zircon percentage is low at sub cluster-1D and high at sub cluster-1I;

monazite percentage is low at sub cluster-1A and high at sub cluster-1I; Rutile percentage is low at sub cluster-1A and high at sub cluster-1I; opaques percentage is low at sub cluster-1I and high at sub cluster-1F.

Cluster-2: The predominance of coastal red sediments is fall under the cluster-2 category. The cluster-2 is characterized by high opaques and sillimanite. Within the cluster-2 there are eight sub-clusters. Sillimanite percentage is low at sub cluster-2B and high at sub cluster-2G; garnet percentage is low at sub cluster-2E and high at sub cluster-2A; epidote percentage high at sub cluster-2A and remaining all sub-clusters are indicated low; zircon percentage is low at sub cluster-2B and high at sub cluster-2F; monazite percentage is low at sub cluster-2G and high at sub cluster-2D; rutile percentage is low at sub cluster-2D and high at sub cluster-2A; opaques percentage is low at sub cluster-2G and high at sub cluster-2B.

S. No.	Sillimanite	Garnet	Epidote	Zircon	Monazite	Rutile	Opaques
1-F/V	31.08	22.91	1.28	1.64	1.29	1.07	39.92
2-F/J	17.25	18.21	1.32	2.75	6.29	0.63	52.52
3-F/A	33.11	13.41	1.07	1.57	0.80	0.74	48.57
4-F/S	18.14	17.81	0.82	1.32	7.27	0.86	53.06
5-F/R	23.16	10.06	0.90	1.81	1.92	0.64	60.63
6-F/E	18.55	13.30	0.50	0.68	0.92	9.05	56.03
7-F/T	7.44	18.20	0.48	0.84	0.78	0.97	70.16
8-F/K	12.70	28.39	0.85	1.43	1.15	0.63	54.02
9-F/N	13.94	22.35	0.69	0.78	1.80	5.50	53.73
10-B/V	30.24	15.88	2.02	2.27	1.31	1.23	45.39
11-B/J	24.03	10.17	2.01	2.26	1.44	0.74	57.67
12-B/A	21.93	11.25	1.67	2.58	7.44	2.55	50.83
13-B/S	22.66	11.47	1.34	2.81	0.72	3.66	55.51
14-B/R	23.44	12.95	1.35	4.23	2.77	2.10	51.68
15-B/E	33.65	28.35	1.31	4.38	0.83	5.41	24.72
16-B/T	23.06	36.75	1.42	7.62	6.95	0.68	22.04
17-B/K	25.77	16.74	1.20	1.11	4.73	3.01	46.27
18-B/N	23.70	24.17	1.31	2.85	2.66	0.53	43.39
19-D/V	20.44	15.16	1.65	5.27	4.70	0.73	50.24
20-D/J	16.74	20.31	1.59	6.50	1.52	0.99	50.39
21-D/A	21.26	15.82	1.69	2.18	2.76	2.49	51.82
22-D/S	18.13	20.11	1.35	2.33	2.37	1.05	52.66
23-D/R	16.85	16.27	1.05	3.11	1.87	3.89	55.24

24-D/E	21.42	21.38	0.77	4.93	0.76	2.44	46.46
25-D/T	13.38	27.07	0.96	2.10	0.45	3.79	50.48
26-D/K	20.71	28.62	0.78	2.31	0.42	2.69	42.54
27-D/N	22.40	22.84	0.67	5.04	6.38	0.55	40.46
28-CR	12.35	0.69	0.00	2.50	2.04	0.39	78.43
29-CR	13.50	0.09	0.00	1.54	2.28	0.34	80.36
30-CR	14.82	0.04	0.00	0.79	1.95	0.52	80.61
31-CR	17.47	3.51	0.00	1.89	1.17	0.30	70.22
32-CR	32.29	0.82	0.00	1.37	0.00	0.36	61.81
33-CR	15.24	0.06	0.00	2.57	1.21	0.18	78.01
34-CR	15.31	0.09	0.00	1.46	0.66	0.25	78.67
35-CR	20.24	0.00	0.00	0.74	0.24	0.00	75.38
36-CR	23.88	1.06	0.00	1.41	0.80	0.53	61.11
37-CR	13.40	0.21	0.00	1.76	1.48	0.80	76.43
38-CR	16.71	0.06	0.00	1.75	0.33	0.51	76.05
39-CR	13.72	0.00	0.00	2.44	0.77	0.65	77.30
40-CR	24.03	0.00	0.00	1.06	0.41	0.33	62.77
41-CR	13.07	0.00	0.00	2.37	0.99	0.84	78.28
42-CR	19.70	0.00	0.00	1.68	0.85	1.05	73.14
43-CR	16.52	0.00	0.00	2.37	1.44	0.90	75.55
44-CR	18.83	0.00	0.00	2.72	0.78	0.63	70.30
45-CR	21.42	0.12	0.00	2.99	0.00	0.45	70.28
46-CR	17.94	0.00	0.00	3.71	1.14	0.75	71.70
47-CR	19.88	0.00	0.00	3.22	0.00	0.35	72.22
48-CR	30.83	0.00	0.00	2.49	0.00	0.66	57.62
49-CR	25.10	0.00	0.00	3.03	0.99	0.47	64.38
50-CR	17.81	0.22	0.00	2.22	1.06	0.56	71.62
51-CR	20.94	0.00	0.00	2.50	0.43	0.52	69.26
52-CR	14.30	0.00	0.00	1.39	0.00	0.70	81.31
53-CR	21.18	0.00	0.00	3.45	2.29	0.54	67.17
54-CR	19.73	0.00	0.00	1.94	0.59	0.39	72.74
55-CR	20.79	0.00	0.00	1.78	0.40	0.00	73.63
56-CR	18.75	0.00	0.00	2.79	2.24	1.01	73.70
57-CR	18.84	0.23	0.00	3.54	1.55	1.70	67.27
58-CR	10.32	0.33	0.00	0.94	5.82	0.89	79.24
59-CR	8.77	0.00	0.00	0.23	4.97	0.11	82.43
60-CR	13.78	0.00	0.00	1.07	4.85	0.00	76.46
61-CR	20.07	0.00	0.00	2.05	2.27	0.30	66.66
62-CR	17.56	0.00	0.00	0.65	1.41	0.24	74.20

63-CR	15.05	0.49	0.00	1.88	4.32	0.17	73.39
64-CR	18.36	0.00	0.00	1.06	2.22	0.19	74.77
65-CR	14.35	0.21	0.00	0.91	1.22	0.57	78.51
66-CR	5.05	0.00	0.00	1.15	0.60	0.84	72.08
67-CR	13.19	0.25	0.00	2.18	3.21	0.19	59.34
68-CR	8.58	0.99	0.00	0.76	1.45	0.00	83.32
69-CR	16.57	0.00	0.00	0.76	6.38	0.69	60.17
70-CR	3.42	0.24	0.00	2.43	1.18	1.08	78.83
71-CR	3.24	0.00	0.00	1.91	4.31	0.34	88.46
72-CR	2.06	0.00	0.00	1.85	2.72	0.56	82.22
73-CR	16.18	0.00	0.00	0.75	0.85	0.00	75.34
74-CR	13.85	0.00	0.00	1.72	2.95	0.54	74.65
75-CR	28.48	0.00	0.00	1.15	0.00	0.00	66.48
76-G/SB	31.86	27.25	0.49	0.25	0.16	0.40	34.20
77-G/SB	22.64	24.37	1.50	0.64	0.09	0.58	43.02
78-G/SB	23.89	17.07	1.61	0.30	0.40	0.62	41.88
79-G/SB	15.75	20.18	0.70	1.20	1.11	1.25	57.75
80-G/SB	17.09	14.96	1.13	2.50	1.44	2.27	57.95
81-G/SB	17.91	20.18	0.90	0.93	0.79	1.82	53.46
82-G/SB	15.39	20.43	0.51	1.28	1.64	2.34	56.01
83-G/SB	13.37	20.53	0.76	1.26	2.80	1.68	58.05
84-G/SB	18.59	26.10	0.54	0.87	0.70	0.93	49.69
85-G/SB	3.70	8.43	0.41	4.70	3.67	2.48	74.45
86-G/SB	13.14	14.33	0.67	1.13	1.37	1.83	66.04
87-G/SB	16.48	19.67	0.56	0.76	1.17	1.46	57.96
88-G/SB	7.93	10.36	0.72	2.81	2.82	1.76	71.74
89-G/BB	8.21	13.01	0.82	1.57	3.96	1.25	69.59
90-G/BB	5.77	7.27	0.37	3.56	3.73	1.67	76.24
91-G/BB	6.24	9.97	0.57	3.42	2.88	1.83	73.21
92-G/EB	8.06	10.04	0.37	3.04	2.28	1.34	73.41
93-G/EB	15.60	18.11	0.69	2.99	2.11	2.16	48.44
94-G/EB	15.56	15.31	1.16	1.88	1.50	1.70	60.76
95-G/BB	22.48	23.20	0.81	1.27	1.33	1.22	47.89
96-G/BB	25.41	15.96	1.26	0.19	0.49	0.48	43.46
97-G/BB	24.46	17.39	1.43	0.29	0.41	0.61	42.17

Table 2: Percentages of heavy mineral data of the study area.

(S. No. 1-27: Beach sediments (Foreshore, Backshore and Dune); S. No. 28-75: Coastal red sediments; S. No. 76-97: Gosthani estuary sediments (swash bar, barrier bar, estuary bar and back barrier)

Cluster-1	**Sillimanite**	**Garnet**	**Epidote**	**Zircon**	**Monazite**	**Rutile**	**Opaques**	**Others**
1A	31.47	25.08	0.88	0.94	0.73	0.74	37.06	3.11
1B	22.22	24.10	0.97	2.84	1.94	1.33	43.96	2.63
1C	29.71	15.34	1.43	1.65	2.28	1.66	46.74	1.19
1D	22.34	17.13	1.25	0.94	0.85	0.97	43.99	12.53
1E	17.63	19.32	1.20	2.76	3.65	1.07	52.42	1.95
1F	15.55	18.71	0.82	1.60	1.67	2.51	57.18	1.96
1G	14.89	27.19	0.78	1.47	0.76	1.79	51.40	1.73
1H	21.94	12.52	1.39	2.73	2.83	2.74	54.30	1.54
1I	28.35	32.55	1.37	6.00	3.89	3.04	23.38	1.43
1(A+B+C+D+E+F +G+H+I)	22.68	21.33	1.12	2.33	2.07	1.76	45.60	3.12
Cluster-2	**Sillimanite**	**Garnet**	**Epidote**	**Zircon**	**Monazite**	**Rutile**	**Opaques**	**Others**
2A	7.56	11.45	0.55	2.63	2.69	1.64	71.85	1.62
2B	6.06	0.26	0.00	1.35	3.41	0.50	82.42	6.00
2C	14.01	0.14	0.00	1.77	1.26	0.52	78.79	3.50
2D	14.22	0.16	0.00	1.56	4.04	0.24	74.83	4.95
2E	18.58	0.01	0.00	1.70	0.96	0.42	74.25	4.22
2F	19.39	0.45	0.00	2.79	1.19	0.64	69.39	6.16
2G	27.44	0.31	0.00	1.75	0.37	0.39	62.36	7.38
2H	11.60	0.08	0.00	1.36	3.40	0.57	63.86	19.11
2(A+B+C+D+E+F +G+H)	14.86	1.61	0.07	1.86	2.17	0.62	72.22	6.62

Table 3: Average heavy mineral percentages of different clusters

Provenance

INS Kalinga area (coastal red sediments) is bounded by small streams Chittigadda in the North-West and Peddagadda in the South-West. An ephemeral river Gosthani flows on the Northern side of the INS Kalinga area and further north of this study area ephemeral rivers like Nagavali, Vamsadhara (originates in the Eastern Ghats Mobile Belt). In the Southern side of the study area, ephemeral rivers like Sarada, Varaha and Tandava originated in the Eastern

Ghats and rocks consisting mainly khondalite and charnockites.

Above stated all the rivers predominantly traversed by the Eastern Ghats Mobile Belt (EGMB). The Eastern Ghats are made up of khondalites and charnockites. Khondalites well foliated with garnet-sillimanite-biotite-feldspathic gneisses. They are mainly derived from metamorphosed products or pelitic sediments and occur in various shades of brown, buff, red, pink and grey. Mineral assemblages in khondalites are garnet ± sillimanite ± potash feldspar +quartz, garnet + biotite + sillimanite + potash feldspar + plagioclase + quartz, garnet + biotite + cordierite + sillimanite + plagioclase + quartz and garnet + biotite + cordierite + plagioclase + quartz (Murthy and Divakara Rao, (1999)). Khondalites are relatively less competent as compared to charnockites, medium to coarse grained and are highly weathered (Chetty, 1999). Excessive leaching of garnets in the rock imparts a dark reddish colour to the rock. The Charnockitic group of rocks includes basic charnockites, acid to intermediate charnockites and hypersthene-gneisses. Basic charnockites (pyroxene granulites) consists of hypersthene, augite/diopside and calcic plagioclase. Acid to intermediate charnockites are consists of potash and sodic feldspar, hypersthene, quartz and garnet are the main constituent minerals. Opaques, apatite, zircon and sphene occur as accessories.

The interpretation of heavy mineral data sets indicates that the nature and presence of similar heavy mineral assemblage in a beach sub-environments, coastal red sediments, and Gosthani estuary sub-environments suggests that the study area heavy minerals have been derived from the same source of lithologies.

From the above, it is clear that the sillimanite comes from khondalite series of Eastern Ghats. The prismatic character of the sillimanite minerals also suggests their derivation from khondalitic rocks. The provenance of garnets is related to Khondalite suite (Garnet – sillimanite – graphite gneisses and schist) of Eastern Ghats, occasionally dark pink garnets are derived from charnockitic rocks (Mallik, 1968). Particularly the grains of garnets in coastal red sediments are highly altered and show leached and pitted surfaces, which indicates that these garnets might have been giving rise to the red colour to the sediments. The Eastern Ghats are considered to be the “home” of well-rounded monazite. This is based on the occurrence of monazite in pegmatites (Mahadevan and Sathapathi, 1948) and charnockites (Murty, 1958) of the Eastern Ghats. The sub-angular grains of magnetite and ilmenite indicates that they might have been derived from nearby sources, i.e.

mainly Eastern Group of rocks (Venkat Ram Reddy, 2015). Zircons are mostly rounded and sometimes euhedral in shape. These euhedral grains are mostly from granitic rocks and to a less extent from charnockites whereas the rounded ones are mainly from khondalites (Rajasekhara Reddy, et. al., 2009a). Epidote is derived from low-grade metamorphic rocks like khondalites (Mallik, 1968) and pyroxene granulites.

Weighted pair-group average Euclidean distances

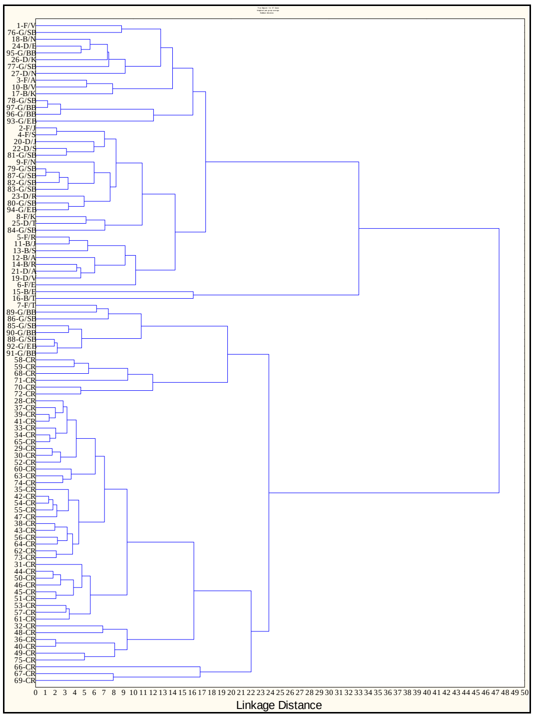

Figure 2: Dendogram

Conclusions

The heavy mineral suite predominantly consists of opaque minerals, sillimanite and garnet followed by minor amounts of zircon, monazite, rutile, and epidote etc.

Heavies are concentrated more in medium fractions (+120) than in coarser and finer fractions in the Gosthani estuary sub-environments, coastal red and dune sediments, whereas heavies are concentrated more in finer fraction (+230) than in the coarser fraction in foreshore and backshore sediments.

Garnets are concentrated more in coarser (+60) than in the finer fraction and decreases gradually from <+60 to +230 ASTM in all sub-environments, except coastal red sediments and swash bar. Opaques are concentrated more in finer fraction (+230) compared to other fractions in all sub-environments, except estuary bar. Sillimanite are concentrated more in medium fraction (+120) fraction compared to other fractions in foreshore, dune, swash bar and back barrier environments whereas sillimanite increases gradually from <+60 to +230 ASTM in back shore, coastal red sediments, barrier bar, and estuary bar.

The garnet concentrations are low in coastal red sediments compared to beach and Gosthani sub-environments and the grains of garnets are insignificant and found to be occurring in highly altered state and show leached and pitted surfaces, which indicates that garnets might have been undergone chemical decomposition under acidic conditions which led to produce iron oxides causes for red colorization of the sediment. The stability of members of the garnet group varies according to their chemistry. Dana, (1985) and Allen, (1948) observed that garnets with high ferrous iron content were particularly prone to disintegration in their investigation.

The interpretation of heavy mineral data sets indicates that the nature and presence of similar heavy mineral assemblage in a beach sub-environments, coastal red sediments, and Gosthani estuary sub-environments suggests that the study area heavy minerals have been derived from the same source of lithologies. The heavy mineral assemblages and their concentrations of heavy minerals in different sub-environments of coastal sediments are derived mainly from metamorphic suite of rocks i.e., Eastern Ghats group of rocks of khondalites and charnockites.

The results of the cluster analysis have clearly brought about the importance of variations in the heavy mineral percentages in forming clusters. Application of cluster analysis on the heavy minerals variations resulted in two main clusters. Cluster-1 consists of nine sub-clusters and cluster-2 consists of eight sub-clusters. Beach environment (foreshore, backshore, and dune) and Gosthani estuary sediments (swash bar, barrier bar, estuary bar and back barrier) fall under the cluster-1 category. The predominance of coastal red sediments is fall under the cluster-2 category. The cluster-1 is characterized by high opaques, sillimanite, and garnet whereas cluster-2 is characterized by high opaques and sillimanite. The sub-clusters that formed within the major clusters represent the small variations in their characteristics minerals.

Acknowledgement

Authors are thankful to Prof. C.V. Raman, former Director, Delta Studies Institute and former principal, College of Science and Technology, Andhra University for valuable guidance and extending the lab facilities to carry out this research work.

References

Allen, V.T., (1948). Weathering and heavy minerals. Jour. Sedim. Petrol., 18, 38-42.

Chetty, T.R.K., (1999). Evolution of the Eastern Ghats granulite belt (Phase I), Terminal Report, NGRI, Hyderabad.

Dana, E.S., (1985). The system of mineralogy of James Dwight Dana, 6th edn. New York: Wiley, 1134.

Karuna Karudu, T., (2012). Textural and heavy mineral characteristics of different sub-environments of Mahanadi delta, East coast of India. Ph.D. Thesis submitted to Andhra University.

Kaufman. L. and Rousseeuw, P.J (2005). Finding groups in data. An introduction to cluster analysis. Wiley, Hoboken, NY.

Mahadevan. C. and Nateswararao, B. (1950). Black sand concentrates in Vizagpatnam coast. Curr. Sci., 19, 48-49.

Mahadevan, C. and Sathapati, N. (1948). The home of Monozites in the Vizagapatnam area. Curr. Sci., 17, 297.

Mahadevan, C. and Sriramdas, A. (1948). Monazites in the beach sands of Vizagapatam District. Proc. Ind. Acad. Sci., 27, 275-27.

Mallik, T.K., (1968). Heavy minerals of shelf sediments between Vishakhapatnam and the Penner delta, eastern coast of India. Bull. Nat. Inst. Sci. India., 38, 502-512.

Mange, Maria A. and Wright, David T. (2008). Heavy Mineral in Use, Development in Sedimentology, Elsevier, New York. 58, XXVII.

Murali Krishna, K.N., Reddy, K.S.N., Ravi Sekhar, Ch., Bangaku Naidu, K., Ganapathi Rao, P. and Reddy, G.V.R. (2016). Heavy Mineral Studies on Late Quaternary Red Sediments of Bhimunipatnam, Andhra Pradesh, East Coast of India. Jour. of the Geol. Soc. of Ind., 90, 111-117.

Murty, M.S., (1958). Occurrence of monazite in the charnockites of Visakhapatnam. Current Science., 27, 347-348

Murthy, N.N. and Divakara Rao, V. (1999). Geochemistry, Provenance and Depositional Environment of the Khondalites from the Eastern Ghats Mobile Belt. Gondwana Research Group Memoir No.5. Eastern Ghats Granulites. 15-30.

Rajasekhar Reddy, D., (1990). Sedimentology and geochemistry of shelf sediments off cannanore-Calicut, West coast of India. Ph.D. Thesis submitted to Andhra University.

Rajasekhara Reddy. D., Karuna Karudu, T., and Deva Varma, D. (2009a). Textural Characteristics and Heavy Mineral Distribution in the Sediments of Kathjodi-Debi River, Mahanadi Delta, East Coast of India. Jour. of Indi. Ass. of Sedi., 28(1), 17-30.

Rajasekhara Reddy. D., Karuna Karudu, T., and Deva Varma D. (2009b). Heavy mineral distribution in different distributaries of Mahanadi Delta, Abstracts volume: XXVI Annual convention of Ind. Ass. of Sed. & National Seminar on Deltas and Other Sedimentary Basins of India: Their Resource Potential, 16 -18th Dec.09, 23.

Ramamohana Rao, T., Shanmukha Rao, CH. and Sanyasi Rao, K. (1982). Textural analysis and mineralogy of the black sand deposits of Visakhapatnam-Bhimunipatnam coast, A.P., India. Jour. Geol. Soc. of India, 23, 284-289.

Reddy, R.D. and Prasad, V.S.S. (1997). Thorium-rich monazites from the beach sands of Kalingapatnam-Baruva coast, Andhra Pradesh, East coast of India. Curr. Sci., 73, 880-882.

Sastry, A.V.R., Swamy, A.S.R. and Prasada Rao. (1981). Distribution of sands along Visakhapatnam-Bheemunipatnam beach. Ind. Jour. Mar. Sci., 10, 369-370.

Sastry, A.V.R., Swamy, A.S.R. and Vasudev, K. (1987). Heavy minerals of beach sands along Visakhapatnam-Bhimunipatnam, East coast of India. Ind. Jour. Mar. Sci., 16, 39-42.

Sri Ramdas A., (1951). The black sand concentrations of Vizagapatam Beach. The Quarterly Jour. of the Geol, Min. and Metall. Soc. of India. 23, 169-180.

Tryon R. C. (1939). Cluster Analysis. Ann Arbor, MI: Edwards Brothers.

Venkata Ram Reddy. G., (2015). Textural and heavy mineral studies of late Quaternary Red Sediments of Bhimunipatnam, Andhra Pradesh, East coast of India. Ph.D. Thesis submitted to Andhra University.

Venkataratnam. K., and Rao A.T. (1968). Zircons from beach sands along East Coast of India. Ind. Mine., 20-29.

Jour. Indian Association of Sedimentologists, Vol. 36, No. 1 & 2 (2019), pp.186-204
ISSN Online 2582 – 2020
ISSN Print 0970 – 3268

Statistical Approach to Study the Lithostratigraphic Sequence in the Proterozoic Kolhans

Rohini Das
Department of Geology and Geophysics, IITKharagpur. PIN: 721301
romiyadas@gmail.com

Abstract: Lithofacies succession in the Proterozoic Kolhan Group has been studied statistically using modified Cross-Association Analysis, Markov chain model and Entropy function. The lithofacies analysis based on the field descriptions and their vertical packaging has been done for assessing the sediment depositional framework and the environment of deposition. Six lithofacies arranged in two genetic sequences have been recognized within the succession. The result of Markov chain and cross-association analysis indicates that the deposition of the lithofacies is in NonMarkovian and non cyclic process and represents asymmetric fining- upward. The chi-square test has been done to test randomness in hypotheses for lithofacies transition at confidence level of 95%. The entropy analysis has been done to evaluate the randomness of occurrence of lithofacies in a succession. Two types of entropies are related to every state: one is relevant to the Markov matrix expressing the upward transitions (entropy after deposition), and the other, relevant to the matrix expressing the downward transitions (entropy before deposition). The total energy regime calculated from the entropy analysis showing maximum randomness suggests that changing pattern in deposition has been a result of rapid to steady flow. This resulted a change in the depositional pattern from deltaic to lacustrine bypassing that finally generated non-cyclicity in the sequence.
Keywords: - *cyclicity, assymetricity, fan-delta, braided-ephemeral*

Introduction

The Kolhan Group is preserved as linear belt extending for 80-100 km with an average width of 10-12 km revealing deposition of Kolhan sediments in narrow and elongated troughs. The Kolhan Group lying unconformably above the Singhbhum granite is bounded by the Jagannathpur lavas on the southeast & south and the Iron Ore Group on the west. The western contact of the basin is faulted against the Iron Ore Group. The Kolhan Group of sediments are found in four detached sub-basins - Chaibasa-Noamundi basin, Chamakpur-

Keonjhargarh basin, Mankarchua basin and Sarapalli-Kamakhyanagar basin (Saha, 1994). Interpreting the depositional environment of the Proterozoic Kolhan sequence was difficult because of (a) the absence of zoo-fossils,(b) the absence of land vegetation, which has profound influence on precipitation, run-off, and sediment yield and (c) scarcity of exposures. Vertical variations of lithofacies within a given sequence play an important role in the recognition of depositional environment and their lateral dispersal (Walker, 1963). In order to determine the depositional architecture and its regional variations, a check of the results obtained so far (Tewari and Singh, 2009) by mathematical means seems desirable. Markov chain is one of the statistical methods that can be used to study the probability of occurrence and repetition of different rock units during deposition (Hota, 2000).

Study Area

The Kolhan Group in general (Fig.1) displays low (5˚-10˚) westerly dip. It unconformably overlies the Singhbhum granite to the east and with a faulted contact on the Iron Ore Group of rocks to the west (Saha, 1994). A pyrophyllitic shale layer (10 m thick) is locally present in between the Singhbhum granite and the Kolhans (Saha, 1994). The Chaibasa-Noamundi basin extends from Chaibasa (Long. 85^0 48'E: Lat. 22^0 33'N) in the north to Noamundi (Long. 85^0 28′ E: Lat. 22^0 09′N) in the south (length: 60-80 km; width: 8-10 km). The Chamakpur - Keonjhargarh (Long. 85°20'-85°35' E ; Lat. 21°35'-22°10' N) on the other hand covers an area approximately 375 km^2

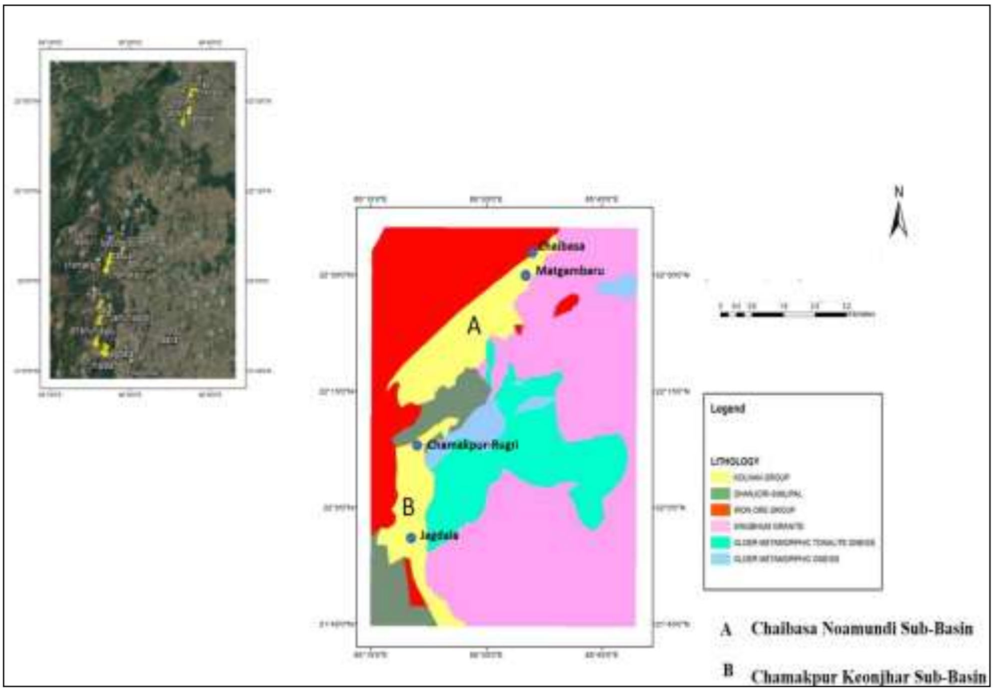

Fig. 1The geological map of Kolhan basin showing the two sub-basins (After Saha, 1994) with location index from Google earth.

(length : 50-55 km ; width : 6-8 km).

Methodology

Fieldworks were carried out to describe and characterize the lithounits of the Kolhan basin from Chaibasa to Chamkpur. At each exposure, the different lithounits were studied and identified on the basis of their bed geometries, gross lithologies, and sedimentary structures. The textural and the structural aspects of the lithounits observed in the outcrops were then clubbed into six lithofacies for better representation. The identity of each lithofacies was based on the presence of a set of primary textures and structures (Selley, 1970, 1976). Six lithofacies identified are:

(a) Granular lag facies (GLA),
(b) Granular sandstone facies (GSD),
(c) Sheet sandstone facies (SSD),
(d) Plane laminated sandstone facies (PLSD),
(e) Rippled sandstone facies (RSD), and
(f) Thin laminated siltstone-sandstone facies (TLSD)

Software package used for the statistical analyses and graphical representations was STATISTICA 8.0. Vertical sedimentary logs are prepared using software Sedlog. Only the representative sections required for the statistical analysis are shown. Programming of algorithm for Markov chain analysis and entropy analysis is carried out in Matlab and R.

Cross Association Analysis

Cross association detects the similarity between correlated geological vertical sections. Cross association is used to compare several geological vertical sections which are arbitrarily selected from different localities. Tracing the beds from section to section finally leads to what is known as lithological correlation. Lithological correlation meets with difficulties due to: 1) Lateral variation in bed thickness, 2) Lithology and 3) Missing of strata by erosion, lack of fossils, and tilting of strata The present paper confirms the validity of the geostatistical cross association method in facilitating the correlation between different geological sections which have great variation in litholog, thickness and obscurity in a single sedimentary succession.

Structuring Data for Cross Association Analysis

Lithounits	GLA	GSD	RSD	SSD	TLSD	PLSD
Gangabasha	1	2	1	0	0	4
Behind IT college	0	1	1	0	2	2
Rajanbasha	0	1	1	0	1	1
Gumuagara	0	4	0	0	2	4
Arjunbasha	2	1	1	2	3	4
Tunglai	0	3	2	0	0	3
Gutuhatu	0	1	1	0	2	0
Bingtopang	0	0	1	2	4	3
Bistampur	1	2	0	1	2	2
Diliamarcha	0	3	4	0	0	0
Matgamburu	1	1	2	0	0	1
Rajanka	1	2	2	0	0	3

Name of the Location	Numerical value of lithofacies present												
Gangabasha	6	3	5	3	5	3	4	3					
Behind IT college	5	2	3	4	3	2							
Rajanbasha	5	3	2	4									
Gumuagara	2	3	5	3	5	3	5	2	5	3			
Arjunbasha	2	3	1	4	1	5	2	6	3	6	3	2	3
Tunglai	3	5	3	5	4	5	4	3					
Gutuhatu	5	2	4	2									
Bingtopang	3	2	3	2	4	1	2	3	2	1			
Bistampur	2	5	2	5	3	6	3	1					
Diliamarcha	4	5	4	5	4	5	4						
Matgamburu	6	4	3	4	5								
Rajanka	6	5	3	4	3	5	3	4					

Table 2: Summary Statistics of different litho-columns of the study area

Analytical Procedure

To assess the degree of similarity between two sequences (sections), the nominal values in a given sequence are moved stepwise past the nominal values of a second sequence.

Δ = Number of comparisons (the length of the overlapped segments) and

t= the number of matches

The **Cross Association Index (CAI**) = the ratio of the number of matches to the length of the two overlapping segments.

Assuming that the number of matches at position *i*, then **CAI** is **CAI (I) = t/Δ.** The results of cross association analysis are described in Table.4.

X= Number of observations in the $\mathbf{k^{th}}$ state of the chain

Y=Number of observations in the $\mathbf{k^{th}}$ state of the chain.

XY=Product of **X** and **Y**.

M=Match position

P=Probability of match at any position of comparison

For any two random sequence of the same composition.

1- P= Probability of mismatch at any position of comparison for any two random sequence of the same composition...

E= Expected number of matches =**PΔ**

E'=Expected number of mismatches =**Δ-E**

O=Observed number of matches = **t**

O' = Observed number of mismatches =**Δ -O** Let the values of **1st** sequence be $\mathbf{a_1}$**, a2, a3, AK**.

then $\sum \mathbf{a_i}$**=n** where ai denotes the total number of occurrences of state **i**.

similarly, for **2nd** sequence of values are denoted by **b_1, b2, b3,......., b_k** then **$\sum b_i=m$** where bi denotes the total number of occurrences of state **i**. Using some counting method, the total number of possible ways of filling any match position is **m*n,** with 2 different values of **k**. While the same is **$\sum a_ib_i$** for identical values of **k**.

Thus the probability of match position of comparison for any two random sequence of the same composition is **$P = \sum a_ib_i /mn$**. The chi square test used as an approximation test.

χ 2 ={ (O-E) 2 /E }+ {(O'-E')2/E' }………equation (1)

Yates correction may be applied in statistics especially when the expected number of matches is small. This correction calls for subtraction of 0.05 from the absolute difference of expected and observed number of matches for a given significant level of 5%. the corresponding critical value is 3.84.. Thus, the equation (1) becomes,

χ 2 ={ (O-E-0.05) 2 /E }+ {(O'-E'-0.05)2/E' } When **Gangabasha** section is moved by **Behind ITI college** section one position at a time and is compared at each match position, it is observed that the best match position is at **10^{th}** with **3** matches and **Δ=3/5**. When the last state of Gangabasha section (plane laminated sandstone) matches with 5^{th} state of Behind ITI college section (plane laminated sandstone).

Null hypothesis,

H_0: Two sequence are not similar

H_1: H_0 is not true

The p-value is a probability that measures the evidence against the null hypothesis. Lower probabilities provide stronger evidence against the null hypothesis. It is used to determine whether to reject or fail to reject the null hypothesis, which states that the variables are independent. The p value calculated is 0.007 for r (degrees of freedom) varying from 0 to 5 from the chi-swuare table which is less than 0.05(5% significant level) and strongly support that H_0 is not true.

Match position 1 : 6 3 5 3 5 3 4 3 5 2 3 4 3 2 In this case *t = 0 and CAI(1) = 0,*

Match position 2: 6 3 5 3 5 3 4 3 5 2 3 4 3 2 In this case *t = 0 and CAI(2) = 0,*

Match position 3: 6 3 5 3 5 3 4 3 5 2 3 4 3 2 In this case *t = 1 and CAI(3) = 1/3.*

Match position 4: 6 3 5 3 5 3 4 3 5 2 3 4 3 2 In this case *t = 0 and CAI(4) = O*

Match position 5 : 6 3 5 3 5 3 4 3 5 2 3 4 3 2 In this case *t = 2 and CAI(5) =2/5,*

Match position 6: 6 3 5 3 5 3 4 3 5 2 3 4 3 2 In this case *t = 0and CAI(6) = 0,*

Match position 7: 6 3 5 3 5 3 4 3 5 2 3 4 3 2 In this case *t = 2and CAI(7) = 2/6=1/3.*

Match position 8: 6 3 5 3 5 3 4 3 5 2 3 4

3 2 In this case *t = 1 and CAI(8) = 1/6*
Match position 9: 6 3 5 3 5 3 4 3 5 2 3 4 3 2 In this case *t = 3 and CAI(9) = 3/5,*
Match position 10: 6 3 5 3 5 3 4 3 5 2 3 4 3 2 In this case *t = 1 and CAI(10) = 1/4,*
Match position 11: 6 3 5 3 5 3 4 3 5 2 3 4 3 2 In this case *t = 1 and CAI(11) = 1/3.*
Match position 12: 6 3 5 3 5 3 4 3 5 2 3 4 3 2 In this case *t = 0 and CAI(12) = 0.*
Match position 13: 6 3 5 3 5 3 4 3 5 2 3 4 3 2 In this case *t = 0 and CAI(12) = 0.*

m*n= **∑Xi∑Yi** =6*8 =48
∑XiYi =2+1+8=11

Thus, **p= ($\sum X_iY_i$ /m*n)** =11/48=.2291
E=Δp=.2291*5=1.145 **{asΔ= 5 from match num 10}**
E'=Δ-E=5-1.1872=3.855 And **O=t**=3
O'=Δ-O=5-3=2

χ 2Y ={ (O-E-0.5) 2 /E }+ {(O'-E'-0.5)2/E' } ={(3-1.145-0.5)2/1.145}+{(2-3.855-0.5)2/3.855}

= 1.5+1.44 =**2.9** < **3.84** hence null hypothesis can't be rejected. **Correlation is not significant at 5%** significant level**.**

Markov Chain Analysis

In the field it is observed that there is gross lithological asymmetricity present between various lithofacies. There is marked difference in the sandstone and shale thickness, with shale thickness very high as compared to sandstone. It is difficult to prove in the field the presence of time independent depositional relation, if any, between the two facies as there is absence of unconformity. To prove cyclic arrangement in the lithofacies in the study area, the Markov property was applied (Gingerich,1969;Miall, 1973; Powers and Easterling,1982). Cyclic sedimentation defines cyclic or rhythmic sedimentation as a series of lithologic elements repeated through time. Alternatively, two types of observable cyclicity may be noteworthy: one in which there exists an order of sequence only, and another in which there is a certain order of repetition along the vertical scale of the sedimentary succession. In this study it is considered to ignore thickness altogether. Markov process, named after the Russian mathematician Andrey Markov, is a stochastic process that satisfies the Markovian property. It can be used to model a random system that changes states according to a transition rule that only depends on the current state. In a first-order Markov process, a lithologic unit or a facies state, F_j observed at a point n depends upon the facies state F_i observed at point (n-1). In other words, the geologic situation at point (n-1) governs the event that will happen at n. The transition probability of a facies being in the state F_j at n given that the facies is in state F_i at (n-1) is denoted by

$P_{ij}(n-1, n)$, i.e. for discrete-time Markov chains,

$$P_{ij}(n-1, n) = P[(Fn_j)|(F(n-1)_i)]$$

Structuring Data for Markov Chain Analysis

The data used in the study is vertical sedimentary log successions of lithological members coded into a limited number of states for the Markov chain and Entropy analysis (Fig. 2). No account has been taken of the thickness of each member and no multistory lithologies are recognized. Thus, it is not considered possible for a given lithological state to pass upward into the same lithological state. In the present study only discrete lithofacies transitions regardless of individual bed thickness are counted, therefore, focus is on the evolution of the depositional process. In order to prevent transition tendencies from being too diffused throughout the count matrix, only six lithofacies, which are distinctly marked in each sedimentary log as well as in outcrop sections, are used in this study. To analyse cyclic characters through space and time, the lithofacies transitions are analyzed together in all sedimentary logs, and by pooling the data for four sectors as well as for the entire area. Seventeen lithological sections (Fig. 2) were considered for studying the vertical and areal distributions of the lithofacies within the Kolhan basin.

Analytical procedure

Frequency count matrix (F): Frequency count matrix is calculated from the vertical sequence profile of sedimentary logs shown in Fig. 2. Since markov chain is used which has memory less property i.e. the geologic situation at point (n-1) governs the event that will happen at n. That's why all seventeen sedimentary logs can be used to calculate matrix F without loss of information. Subsequently, data for all logs are added and a bulk matrix is structured at Basin level. Number of transition from facies i to j is represented in row i and column j of matrix F (Table 4a), which signifies number of times state j followed immediately after state i in the sedimentary logs. The frequency count matrix is structured into embedded Markov chain considering only transition lithologies and not their thickness as stated elsewhere. Since a transition is supposed to occur only when it results in a different lithology, the diagonal elements are all zeros in the resulting tally matrix.

The modified Markov process model used in this study incorporates structuring of one step embedded tally count matrix (F_{ij}), where i, j corresponds to row and column number. It will be noticed that where i = j, zeros are present

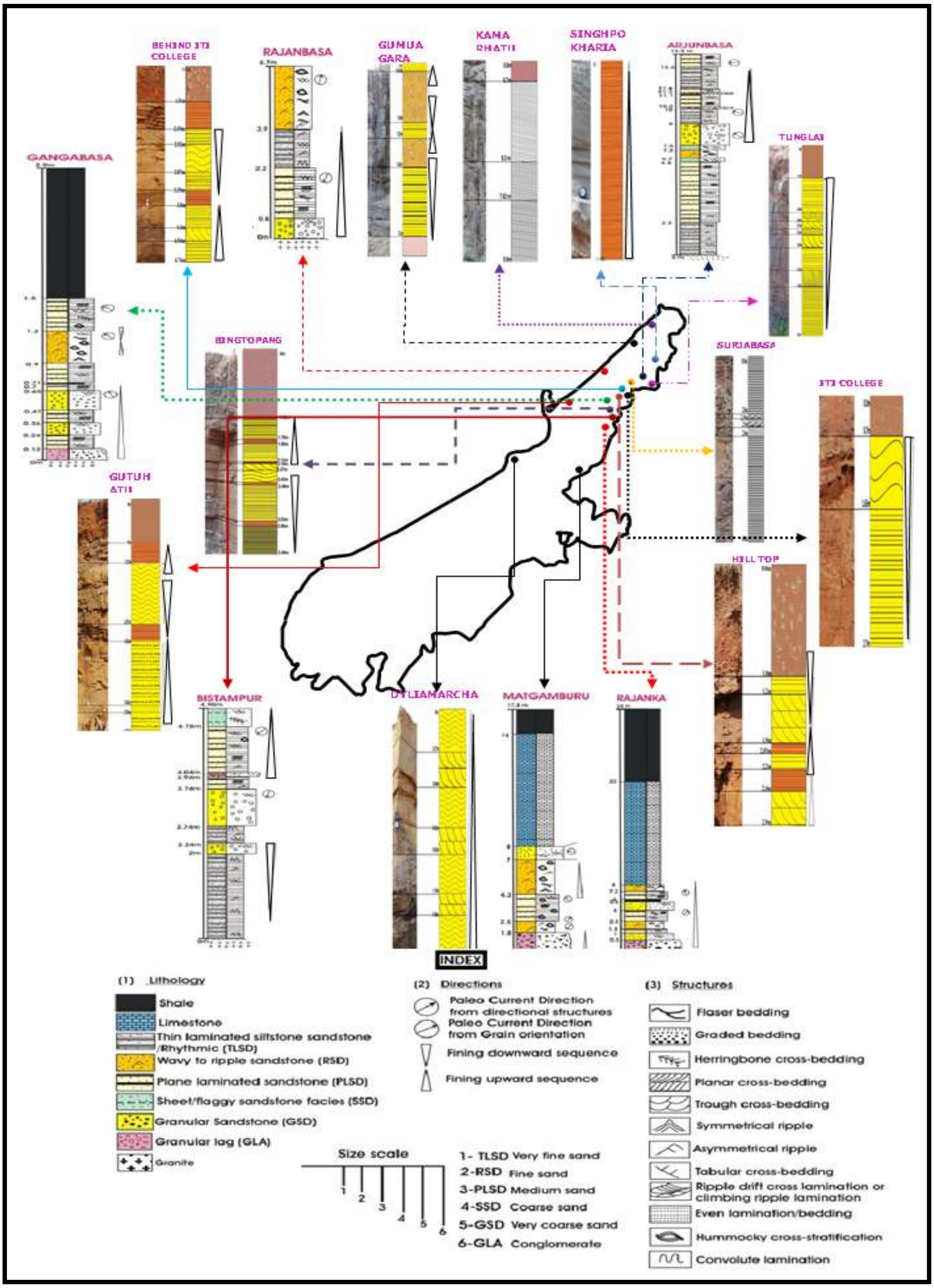

Fig. 2 Location of Lithologs showing the vertical distribution of the lithofacies in the study area

in the matrix, i.e., probability of moving from one state to another state has only been recorded where the lithofacies shows an abrupt change in character, regardless of the thickness of the individual bed.

Transition Frequency Matrix (F)

As mentioned above, a first order embedded chain matrix is structured by counting transition from one facies to another, and the resulting frequency matrix will contain zeros along the principal diagonal (F_{ij} =0)(Table 4a). This is a two dimensional array which records the frequency of the vertical transitions that occur between the different lithofacies in a given stratigraphic succession. The lower bed / facies of each transition couplet are given by the row numbers of the matrix, and the upper bed / facies by the column numbers. Each lithofacies is coded with column numbers or capital letters. The transition count matrix is expressed as F_{ij}, where i = row number and j = column number. When i=j, the transition between same lithofacies are denoted by zeros. In other words, transitions are only recorded when the lithofacies shows abrupt changes in character in spite of the thickness of the individual lithofacies.

Upward Transition Probability Matrix (P)

The upward transition probability matrix pertains to the upward ordering of lithologies in a succession and is calculated in the following manner: $P_{ij} = F_{ij} / SR_i$ Where, SR_i is the corresponding row total (Table 4b). The transition probability matrix represents the actual probabilities of the transition between one lithofacies to another in a vertical section. This array is obtained by taking the number of transitions of one facies to another and dividing by the total number of transitions involving the first facies.

Downward Transition Probability Matrix (Q)

Similar to the upward transition probability of lithologies a downward transition probability (Q matrix) can also be determined by dividing each element of the transition frequency matrix by the corresponding column total, i.e., $Q_{ji} = F_{ij} / SC_j$ Where, SC_j is the column total (Table 4c).

Independent Random Matrix (R)

Assuming that the sequence of rock types was determined randomly an independent trials matrix can be prepared in the following manner: $R_{ij} = C_j / (T – C_i)$ Where, C_i is the column total of facies state F_i, C_j is the column total of facies state F_j, N is the total number of transitions in the system (Table 4d). The diagonal cells are filled with zeros. This matrix represents the probability of the given transition that occur in a random manner. If t=total number of lithofacies, n=rank of the matrix (the total number of rows and columns used), T= n, k=0 F_{ij}, where Fij =number of transition from facies A to facies A-F.

Difference Matrix (D)

A difference matrix (Table 4e) is calculated which highlights those transitions that have a probability of occurring greater than if the sequence were random. By linking positive values of the difference matrix, a preferred upward path of facies transitions can be constructed which can be interpreted in terms of depositional processes that led to this particular arrangement of facies (Miall, 1973). $D_{ij} = P_{ij} - R_{ij}$ A positive value in difference matrix indicates that a particular transition occurs more frequently and a negative value indicates that it occurs less frequently. In difference matrix the values in each rows of the matrix sum to zero. If the values are close to zero, a vertical succession with little or no memory indicates independent nature of deposition of facies in a basin.

Expected Frequency Matrix (E)

It is necessary to construct an expected frequency matrix, since a statistician"s rule of thumb states that chi – square tests should only be applied when the minimum expected frequency in any cell not exceeds 5. The matrix of expected values is given by $E_{ij} = R_{ij} * SR_i$ (Table 4f).

Test of Significance

Non-parametric chi-square ($\chi 2$) test has been applied to ascertain whether the given sequence has a Markovian memory or no memory. To test null hypothesis, chi-square ($\chi 2$) values are calculated for vertical successions (Table 4g).

$$\chi^2 = \sum_{i=0}^{n} \sum_{j=0}^{n} (Fij - Eij)^2/Eij$$

F_{ij} = transition count matrix or observed frequency of elements in the transition count matrix; Eij = Expected frequency matrix

ν = degree of freedom given by the number of non-zero entries in the $[r_{ij}]$ matrix minus the rank of the matrix=n2–2n, where n denotes rank of the matrix If the computed values of chi-square exceed the limiting values at the 5% significance level suggests the Markovity and cyclic arrangement of facies states.

Entropy Analysis

Hattori (1976) applied the concept of entropy to sedimentary successions possessing Markov property to determine the degree of random occurrence of lithologies in the succession. Methods of calculation of entropy as suggested by Hattori (1976) have been largely followed in the present study. Hattori (1976) recognized two types of entropies with respect to each lithological state; one is post–depositional entropy corresponding to matrix P and the other, pre-depositional entropy, corresponding to matrix Q. Hattori (1976) defined post-depositional entropy with respect to lithological state i as

$$E_i^{(post)} = -\sum_{j=0}^{n} P_{ij} * \log(P_{ij}) \quad \text{....eq1}$$

If E_i (post)= 0.0, state i is always succeeded by state j in the sequence. If E_i (post)>0, state i is likely to be overlain by different states. Hattori (1976) defined pre – depositional entropy with respect to state i as

$$E_i^{(pre)} = -\sum_{j=0}^{n} Q_{ij} * \log(Q_{ij}) \quad \text{...eq2}$$

Large E_i (pre) signifies that i occur independent of the preceding state. E_i (post) and E_i (pre) together

Form an entropy set for state i, and serves as indicators of the variety of lithological transitions immediately after and before the occurrence of i, respectively. Hattori (1976) used the interrelationships of E_i (post) and E_i (pre) to classify various cyclic patterns into asymmetric, symmetric and random cycles. The values of E_i (pre) and E_i (pre)calculated by equations (1) and (2) increases with the number of lithological states recognized. To eliminate this influence, Hattori (1976) normalized the entropies by the following equation:

$$R = E/E_{max}, \text{ where, } E_{max} = -\log 2 \frac{1}{n-1}$$

Where R is the normalized entropy, E is either post–depositional entropy or pre–depositional entropy, and Emax is the maximum entropy possible in a system where n state variable operates Table6.

RESULTS

The results of cross association analysis displays associatograms showing the position of maximum match between the widely separated stratal associations of litho sections (Fig. 3; Table 3).

Gangabasha Vs Behind ITI College

The maximum match at 10^{th} position with 3 matches and 2 mismatches for 5 set of comparisons. The probability of matches is .30 and the expected number of matches and mismatches are 1.15 and 3.86 respectively. The computed value of χ^2 (2.90) does not exceed the critical value (3.84) for 1 degree of freedom at 5% significant level. This leads to the acceptance of null hypothesis (H_0) and rejection of the alternative hypothesis (H_1) at 5% level of significance.

Behind ITI college Vs Rajanbasha

The maximum match at 7th position with 2 matches and 1 mismatches for 3 set of comparisons. The probability of matches is .25 and the expected number of matches and mismatches are .75 and 2.25 respectively. The computed value of $\chi 2$ (2.11) does not exceed the critical value (3.84) for 1 degree of freedom at 5% significant level. This leads to the acceptance of null hypothesis (H_0) and rejection of the alternative hypothesis (H_1) at 5% level of significance.

Rajanbasha Vs Gumuagara

The maximum match at 2nd position with 2 matches and 0 mismatches for 2 set of comparisons. The probability of matches is .25 and the expected number of matches and mismatches are .50 and 1.50 respectively. The computed value of χ^2 (4.60) exceed the critical value (3.84) for 1 degree of freedom at 5% significant level. This leads to the rejection of null hypothesis (H_0) and acceptance of the alternative hypothesis (H_1) at 5% level of significance.

Gumuagara Vs Arjunbasha

The maximum match at 2nd position with 2 matches and 0 mismatches for 2 set of comparisons. The probability of matches is .20 and the expected number of matches and mismatches are .4 and 1.6 respectively. The computed value of $\chi 2$ (5.75) exceed the critical value (3.84) for 1 degree of freedom at 5% significant level. This leads to the rejection of null hypothesis (H_0) and acceptance of the alternative hypothesis (H_1) at 5% level of significance.

Arjunbasha Vs Tunglai

The maximum match at 20th position with 1 matches and 0 mismatches for 5 set of comparisons. The probability of matches is .16 and the expected number of matches and mismatches are .15 and .85 respectively. The computed value of $\chi 2$ (2.94) does not exceed the critical value (3.84) for 1 degree of freedom at 5% significant level. This leads to the acceptance of null hypothesis (H_0) and rejection of the alternative hypothesis (H_1) at 5% level of significance.

Tunglai Vs Gutuhatu

The maximum match at 9th position with 1 matches and 2 mismatches for 3 set of comparisons. The probability of matches is .16 and the expected number of matches and mismatches are .47 and 2.5 respectively. The computed value of $\chi 2$ (.42) does not exceed the critical value (3.84) for 1 degree of freedom at 5% significant level. This leads to the acceptance of null hypothesis (H_0) and rejection of the alternative hypothesis (H_1) at 5% level of significance.

Gutuhatu Vs Bingtopang

The maximum match at 5th position with 3 matches and 1 mismatch for 4 set of comparisons. The probability of matches is .25 and the expected number of matches and mismatches are 1 and 3 respectively. The computed value of $\chi 2$ (4.3) exceed the critical value (3.84) for 1 degree of freedom at 5% significant level. This leads to the rejection of null hypothesis (H_0) and acceptance of the alternative hypothesis (H_1) at 5% level of significance.

Bingtopang Vs Bistampur

The maximum match at 2nd position with 1 matches and 1 mismatches for 2 set of comparisons. The probability of matches is .2 and the expected number of matches and mismatches are .4 and 1.6 respectively. The computed value of $\chi 2$ (.75) does not exceed the critical value (3.84) for 1 degree of freedom at 5% significant level. This leads to the acceptance of null hypothesis (H_0) and rejection of the alternative hypothesis (H_1) at 5% level of significance.

Bistampur Vs Dyliamircha

The maximum match at 5th position with 2 matches and 3 mismatches for 5 set of comparisons. The probability of matches is .14 and the expected number of matches and mismatches are .71 and 4.29 respectively. The computed value of $\chi 2$ (1.61) exceed the critical value (3.84) for 1 degree of freedom at 5% significant level. This leads to the rejection of null hypothesis (H_0) and acceptance of the alternative hypothesis (H_1) at 5% level of significance.

Dyliamircha Vs Matgamburu

The maximum match at 2nd position with 2 matches and 0 mismatches for 2 set of comparisons. The probability of matches is .31 and the expected number of matches and mismatches are .63 and 1.37 respectively. The computed

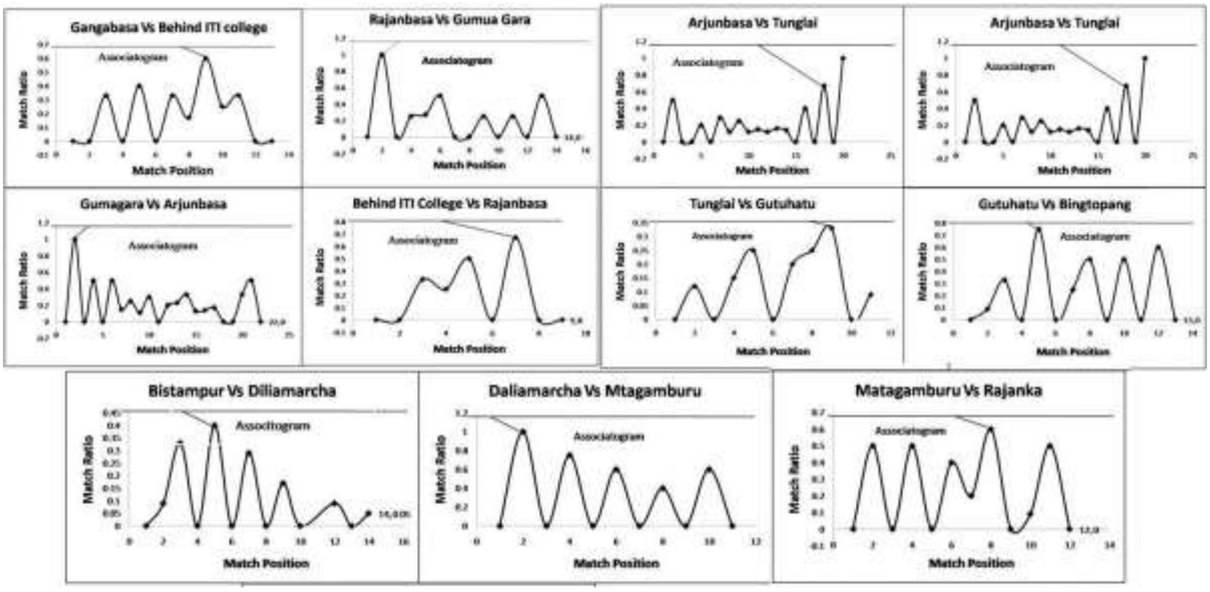

Fig.3Associatogram showing the position of maximum match between the widely separated strata associations.

Value of $\chi 2$ (3.75) exceed the critical value (3.84) for 1 degree of freedom at 5% significant level. This leads to the rejection of null hypothesis (H_0) and acceptance of the alternative hypothesis (H_1) at 5% level of significance.

Comparision Between logs	lithofacies	X	Y	$\sum X_i \sum Y_i$	M	P	1-P	O	O'	E	E'	$\chi^2 Y$	Conclusion
Gangabasha Vs Behind IT college	GLA	1	0	0	10	.3	.7	3	2	1.15	3.86	2.9	Correlation is not significant
	GSD	2	1	2									
	SSD	1	1	1									
	PLSD	0	0	0									
	RSD	0	2	0									
	TLSD	4	2	8									
	TOTAL	8	6	11									
Behind IT college Vs Rajanbasha	GLA	0	0	0	7	.25	.75	2	1	.75	2.25	2.11	Correlation is not significant
	GSD	1	1	1									
	SSD	1	1	1									
	PLSD	0	0	0									
	RSD	2	1	2									
	TLSD	2	1	2									
	TOTAL	6	4	6									

Matgamburu Vs Rajanka

The maximum match at 8th position with 3 matches and 2 mismatches for 5 set of comparisons. The probability of matches is .23 and the expected number of matches and mismatches are 1.13 and 3.88 respectively. The computed value of χ^2 (2.65) does not exceed the critical value (3.84) for 1 degree of freedom at 5% significant level. This leads to the acceptance of null hypothesis (H_0) and rejection of the alternative hypothesis (H_1) at 5% level of significance.

Comparision Between logs	lithofacies	X	Y	$\sum X_i \sum Y_i$	M	P	1-P	O	O'	E	E'	$\chi^2 Y$	Conclusion
Rajanbasha Vs Gumagara	GLA	0	0	0	2	.25	.75	2	0	.50	1.50	4.8	Correlation is significant
	GSD	1	4	4									
	SSD	1	0	0									
	PLSD	0	0	0									
	RSD	1	2	2									
	TLSD	1	4	4									
	TOTAL	4	10	10									
Gumagara Vs Arjunbasa	GLA	0	2	0	2	.2	.8	2	0	.4	1.6	5.75	Correlation is significant
	GSD	4	1	4									
	SSD	0	1	0									
	PLSD	0	2	0									
	RSD	2	3	6									
	TLSD	4	4	16									
	TOTAL	10	13	26									
Arjunbasha Vs Tunglai	GLA	2	0	0	20	.16	.84	1	0	.15	.85	2.94	Correlation not significant
	GSD	1	3	3									
	SSD	1	2	2									
	PLSD	2	0	0									
	RSD	3	0	0									
	TLSD	4	3	12									
	TOTAL	13	8	17									
Tunglai Vs Gutuhatu	GLA	0	0	0	9	.16	.84	1	2	.47	2.5	.42	Correlation not significant
	GSD	3	1	3									
	SSD	2	1	2									
	PLSD	0	0	0									
	RSD	0	2	0									
	TLSD	3	0	0									
	TOTAL	8	4	5									

Comparision Between logs	lithofacies	X	Y	$\sum X_i \sum Y_i$	M	P	1-P	O	O'	E	E'	$\chi^2 Y$	Conclution
Gutuhatu Vs Bingtopang	GLA	0	0	0	5	.25	.75	3	1	1	3	4.3	Correlation is significant
	GSD	1	0	0									
	SSD	1	1	1									
	PLSD	0	2	0									
	RSD	2	4	8									
	TLSD	0	3	0									
	TOTAL	4	10	9									
Bingtopang Vs Bistampur	GLA	0	1	0	2	.2	.8	1	1	.4	1.6	.75	Correlation is not significant
	GSD	0	2	0									
	SSD	1	0	0									
	PLSD	2	1	2									
	RSD	4	2	8									
	TLSD	3	2	6									
	TOTAL	10	8	16									
Bistampur Vs Dalianmarcha	GLA	1	0	0	5	.14	.86	2	3	.71	4.29	1.61	Correlation is not significant
	GSD	2	3	6									
	SSD	0	4	4									
	PLSD	1	0	0									
	RSD	2	0	0									
	TLSD	2	0	0									
	TOTAL	8	7	10									

Comparision Between logs	lithofacies	X	Y	$\sum X_i \sum Y_i$	M	P	1-P	O	O'	E	E'	$\chi^2 Y$	Conclution
Matgandharu Vs Rajanka	GLA	1	1	1	8	.23	.77	3	2	1.13	3.88	2.65	Correlation is not significant
	GSD	1	2	2									
	SSD	2	2	4									
	PLSD	0	0	0									
	RSD	0	0	0									
	TLSD	1	3	3									
	TOTAL	5	8	10									
Daltamarcha Vs Matgandharu	GLA	0	1	0	2	.31	.69	2	0	.63	1.37	3.75	Correlation not significant
	GSD	3	1	3									
	SSD	4	2	8									
	PLSD	0	0	0									
	RSD	0	0	0									
	TLSD	0	1	0									
	TOTAL	7	5	11									

Table 3: Results of Cross Association Analysis in the Kolhan Group

In the listed below tables (Table4a-f) A= GLA; B= GSD; C= SSD; D= PLSD; E= RSD; F= TLSD; SRi= Sum of ith row of the count matrix SC_j= Sum of jth column of the count matrix T= Total number of transition.

Discussion

Markov Chain and Cross Association Analysis

In the interpretation of significant facies transitions it is important to note that the calculated significant transitions

a) Transition Count Matrix (F)

	A	B	C	D	E	F	SR_i	$T\text{-}SR_i$
A	0	1	1	3	0	1	6	33
B	3	0	1	1	1	1	7	32
C	0	1	0	0	0	1	2	37
D	1	2	0	0	1	1	5	34
E	0	2	0	0	0	0	2	37
F	2	1	0	1	0	0	4	35
SCj	6	7	2	5	2	4	Total=26	

b) Upward Transition Probability Matrix(P)

	A	B	C	D	E	F
A	0	0.35	0.1	0.25	0.1	0.2
B	0.316	0	0.105	0.263	0.105	0.21
C	0.25	0.292	0	0.208	0.083	0.167
D	0.286	0.333	0.095	0	0.095	0.19
E	0.25	0.292	0.083	0.208	0	0.166
F	0.273	0.318	0.091	0.227	0.091	0

c) Downward Transition Probability Matrix(Q)

	A	B	C	D	E	F
A	0	0.142	0.5	0.6	0	0.25
B	0.5	0	0.5	0.2	0.5	0.25
C	0	0.142	0	0	0	0.25
D	0.1667	0.285	0	0	0.5	0.25
E	0	0.285	0	0	0	0
F	0.333	.145	0	0.2	0	0

d) Independent Trails Probability Matrix(R)

	A	B	C	D	E	F
A	0	0.167	0.167	0.5	0	0.167
B	0.428	0	0.143	0.143	0.143	0.143
C	0	0.5	0	0	0	0.5
D	0.2	0.4	0	0	0.2	0.2
E	0	1	0	0	0	0
F	0.5	0.25	0	0.25	0	0

e) Difference Matrix (D)

	A	B	C	D	E	F
A	0	-0.183	0.67	0.25	-0.1	-0.033
B	0.113	0	0.37	-0.12	0.037	0.067
C	-0.25	0.208	0	-0.208	-0.083	0.334
D	-0.086	0.067	-0.095	0	0.105	0.009
E	-0.25	0.708	-0.083	0.208	0	-0.167
F	0.227	-0.68	-0.091	0.023	-0.091	0

f) Expected Frequency Matrix (E)

	A	B	C	D	E	F
A	0	2.1	0.6	1.5	0.6	1.2
B	2.212	0	0.735	1.841	0.735	1.47
C	0.5	0.584	0	0.416	0.166	0.334
D	1.43	1.665	0.475	0	0.475	0.95
E	0.5	0.584	0.166	0.416	0	0.332
F	1.092	1.272	0.364	0.908	0.364	0

g)Test Of Significance

Test of Equation	Computed value of	Limiting value at 0.5% significance level	Degree of freedom
Billingslay	14.343	30.14	19

Table 4: Matrices used to analyse transitions of lithofacies in the Kolhan Group

.

Represent the most probable facies transitions, but not their frequency in the studied sedimentary sequences. The real Frequencies of facies transitions are written down in the matrix of observed facies transitions (Table 4). Therefore, when interpreting sedimentary successions it is useful to consider both statistically significant and real facies transitions in order to better understand their significance and real occurrence in the studied sedimentary record. The highest values of <P> and the positive entries of <D> were analyzed to determine the cyclic processes.The computed values of chi-square is lower than the limiting values at the 5% significance level (Tables 4g) this means that the null hypothesis is false, suggesting the deposition of sediments is not by Markovian process and non-cyclic arrangement of facies states in Kolhan Group.The facies relationship diagram (Fig 4) is constructed from the difference matrix results (Table 4e) Relationship diagrams showing upward transition of facies states of Kolhan group in Fig 4.

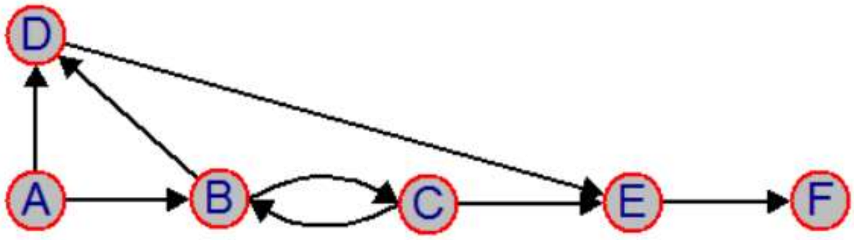

Fig. 4 Facies relationship diagrams showing upward transition of facies states of Kolhan group. A-GLA; B-GSD; C-SSD; D-PLSD; E-RDS; F-TLSD.

The preferred upward transition path for the lithofacies is GLA GSD SSD PLSD RSD TLSD.

The transition between GLA GSD, GSD SSD, SSD PLSD and RSD TLSD is non-Markovian and the lineage is non-repetitive in nature. The obvious aim of such approach was to detect and define cyclic relationships, if any. In the present case the cyclicity is absent or very weak. This information can greatly assist in environmental interpretation.

Entropy Analysis

Both E_{pre} and E_{post} are larger than 0.0 implies all six lithofacies (GLA, GSD, SSD, PLSD, RSD, and TLSD) overlies and also is overlain by more than one state (Hattori, 1976). E_{pre} and E_{post} are larger in number for GSD (Table 5), and it is deduced that the influx of pebbly sandstone into the basin was the most random event. For RSD and PLSD, $E_{pre} > E_{post}$. This relation indicates that rippled sandstones formed in shallow environment, though grainsize and hydrodynamic conditions may change the depth variations to some extent. So this type of findings need critical interpretation.

Large difference in E_{pre} and E_{post} and with $E_{pre} < E_{post}$ relationship in case of facies F indicates its strong dependence on its precursor which is visualised from the Markov metrics (Table 5 and Fig. 4). The depositional pattern in the TSLD facies is indicative of a low energy, suspension fall out during the waning phase of the sedimentation. In other words, these facies accumulated in environment located in the distal part of the basin in preference to other areas. The E (pre) and E (post) plots for coarse to medium-grained sandstone, interbedded fine grained sandstone/shale, shale fall far from the diagonal line (Fig 5). Energy regime related to the total entropy suggests that the shale in distal part of basin and is not of marine origin. The flow pattern overall changes from the deltaic environment to lacustrine environment. Fig 6 is well comparable with the type C cyclic pattern of Hattori, which signifies random lithologic series, as deduced independently by improved Markov process model. The cycles Kolhan basin belongs to the maximum entropy indicated by black dot (Fig.6) (Hattori, 1976).

	E(Post)	E(Pre)	R(Post)	R(Pre)
A	1.793	1.643	0.772	0.707885
B	2.128	2.4643	0.9167	1.061741
C	1	0.9010	0.4306	0.388195
D	1.921	2.1474	0.8279	0.925205
E	0.009	0.5167	0.002	0.22262
F	1.5	0.6937	0.6423	0.250474

Table 5: Matrix used to analyse entropy value of lithofacies

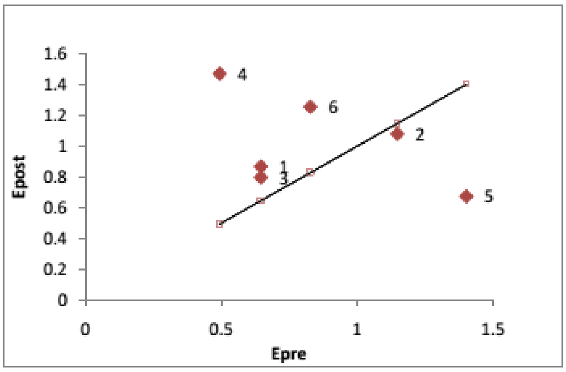

Fig. 5 Entropy set derived from Kolhan basin.1-GLA; 2-GSD; 3-SSD; 4-PLSD; 5-RDS; 6-TLSD.

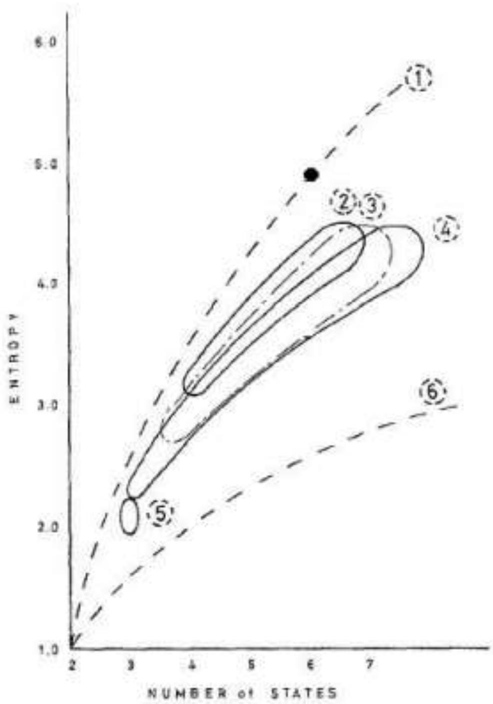

Fig. 6: Relationship between entropy and depositional environment of lithological sequences (after Hattori, 1976). 1-maximum entropy; 2-etropies for coal measure succession; 3-entropies for fluvial-alluvial successions; 4-entropies for neritic successions; 5-entropies for flysch sediments; 6-minimum entropy; Black dot indicate entropy of basin under study.

Conclusion

The application of the cross association analysis on the vertical sections shows that there is no significant correlation in between different lithofacies. The energy level of the deposition during the entire process shows a considerable fluctuation. Lack of correlation suggests lateral facies variation and existence of different environment at different places. The application of the first order Markov Chain analysis on the vertical, sections shows that there is a preferred fining upward transition path in the lithofacies. The operative geological processes were non-Markovian or independent in nature. The energy level during the entire process of sedimentation shows a considerable, fluctuation reflected by the Entropy analysis. Entropy analysis also proves type “C” cyclic pattern of Hattori, which signifies random lithologic series, as deduced independently by improved Markov process model. The cycles of Kolhan basin belongs to the maximum entropy. Asymmetric sequence can be well explained by sediment bypassing. The thinning upward sequences represent lacustrine deposits, while the thickening upward sequences represent point bar-sand flat deposits. Variation in layer thickness is suggestive of deposition by unsteady flow in a fluvial, regime within the channel. The flow was suddenly impeded, and as a result there was a quick fall in the energy of the solid-fluid system that resulted in rapid deposition. It appears that the GLA and the GSD facies represent the channel lag deposits of a braided river and the SSD, RSD, PLSD, and TLSD facies represent the portions of a fining upward sequence complex of a channel bar or possibly the longitudinal bartransverse bar-cross-channel bar complex in a fluvial environment. The result of this study described that the basin was non-cyclic, fining upward asymmetric sedimentary sequence of sandstone, shale with patches of carbonate.

Acknowledgement

The author is grateful to Department of Geology and Geophysics, IIT Kharagpur for giving the opportunity to carry out the research work.

References

Gingerich, P. (1969). Entropy in Markov chain and discrimination of cyclic pattern in lithologic successions. Journal of Sedimentary Research, 39(1), pp.330-497.

Hattori, I. (1976). Entropy in Markov chain and discrimination of cyclic pattern in lithologic successions. Mathematical. Geology, 8(4), pp.477-497.

Hota, R.N. (2000). Quantitative stratigraphic correlation-a case study from two borehole sections of Barakar Formation, Talchir coalfield, Jharkhand. Journal of Geological Society of India, 56, pp.517-524.

Miall, A.D. (1973). Markov chain analysis applied to an ancient alluvial plain succession. Sedimentology, 20, pp.347-364.

Powers, D. W. and Easterling, R. G. (1982). Improved methodology for using embedded Markov chains to describe cyclical sediments. Journal of Sedimentary Petrology, 52, pp.913-923.

Saha, A.K. (1994). Crustal evolution of Singhbhum North Orissa, Eastern India. Memoir Geological Society of India, 27, pp.341.

Selley, R.C. (1970). Ancient Sedimentary Environments and Their Sub-surface Diagnosis (2nd Edn). Routledge**,** Taylor and Francis, London, 320p.

Selley, R.C. (1976). Subsurface environmental analysis of North Sea sediments. Bulletin American Association of Petroleum Geology, 60, pp.184-195.

Tewari, R.C., Singh, D.P., Khan, Z.A. (2009). Application of Markov chain and Entropy analysis to lithologic succession – an example from early Permian Barakar Formation, Bellampalli coalfield, Andhra Pradesh, India. Journal Earth System Science, 18 (5) (2009), pp.583–596.

Walker, R.G. (1963). Distinctive types of ripple drift cross-lamination. Sedimentology, 2, pp.173-188.

Jour. Indian Association of Sedimentologists, Vol. 36, No. 2 (2019), pp.105-110
ISSN Online 2582 – 2020
ISSN Print 0970 – 3268

Connection between climate and tectonics: implication to Kolhan basin

Kasturi Bhattacharyya
Indian Institute of Technology, Kharagpur 721302, India
Email - bhattacharyya.kasturi@gmail.com

Abstract: A simple model for the development and evolution of the Kolhan Basin is proposed. The first event consists of a rapid stretching of the continental lithosphere, which produced thinning and passive upwelling of hot asthenosphere. This stage is connected with block faulting and subsidence. This is synchronous to the existence of the Columbia supercontinent. There was no glaciation during the existence of Columbia. This indicates moderate weathering rate during which the Kolhan Basin formed. This simplistic logical conclusion is supported by the predominance of quartz arenite in the sandstone of the basin. The paucity of feldspars in the thin-sections supports the above findings. The main shallow elongated basin of the Kolhan Formation extends from Chaibasa (85° 48’, 22° 33’) to Noamundi (85°28’, 22° 09’) covering about 34 miles in length and maximum 10 miles in width along the western extremity of the Singhbhum Granite. The petrography and geochemistry of the basin concludes an intracratonic rift tectonic setting in Proterozoic time. This indicate a granitoid source with moderate chemical weathering. High Al2O3/SiO2 and K2O/Na2O ratios reflect a derivation of all the sediments from stable cratons during tectonic quiescences. These alumina ratio indicates that the clastics were deposited in a passive margin or cratonic margin. The existence of Columbia supercontinent during the life of Kolhan Basin indicates no glaciation during that time. This scenario is well supported by findings of petrography and geochemistry of the basin.

Keywords: quartz arenite, intracratonic, passive margin, Kolhan.

Introduction

The Kolhan Basin in Singhbhum District is unique in Its narrow strip-like outcrop pattern, controlled by the of the much older Iron-Ore Formation synclinorium abuts against the Singhbhum Granite in the east of a greater portion of its trend. A part of eastern and entire western boundary is in contact (fault contact) with the Iron-Ore Formation rocks. The Kolhan

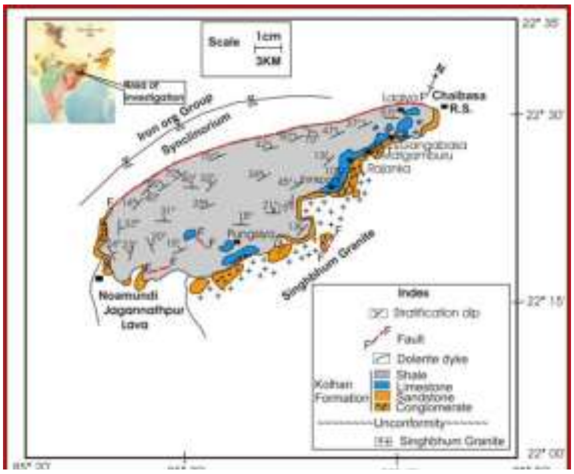

Fig. 1. Geological and structural map of Chaibasa-Noamundi Basin showing the different lithounits (after Chatterjee and Bhattacharya 1969)

Shale Formation is definitely younger than the Iron-Ore Formation as originally suggested by Dunn (1940). The Kolhan Basin is set in a diversified lithological provenance, so that it exhibits the development of a rudaceous, arenaceous, calcareous and an argillaceous facies.

Geology

The main shallow elongated basin of the Kolhan Formation extends from Chaibasa to Noamundi covering about 56km in length and maximum 19 km in width along the western extremity of the Singhbhum Granite (Fig 1). The Kolhan Formation lies over the Iron -Ore Formation and Singhbhum Granite and consists of the basal conglomerate, sandstone, impersistent limestone and with a general westerly. The total thickness of this formation is approximately 100 meters.

Petrography

The Kolhan sandstones are composed mainly of an aggregate of subangular to subrounded quartz embedded in an illitic-clay matrix, with subordinate amounts of feldspar, rock fragments, chert and muscovite, while biotite and chlorite are rare. Table 1 shows the modal analysis of the various constituents in the representative sandstone samples.

Quartz is clearly the dominant detrital mineral constituent with a modal variation from 60.59 % to 82.56 %. Rarely its proportion decreases to 48.77 %. The grains are mostly subangular to subrounded with grain size from 0.06 mm to 1 mm in general. The quartz is dominantly a common unit, slightly vein quartz and strongly undulose quartz are very subordinate in occurrence in the rock. The grains are mostly coated with iron oxide and exhibit authigenic overgrowths which produce euhedral out line in rare cases.

Such overgrowths have replaced the primary hematite coating leaving behind scattered relics of the latter. It is further observed that these overgrowths are rare on that side of the grain which is in contact with the clay.

Recycled quartz grains with abraded outgrowths are occasionally formed. The contacts between the grains are generally plane and rarely sutured and stylolitic. Inclusions of minute apatite, zircon and rutile are rare. They sometimes show gas vacuoles rarely arranged in trails.

The detrital mineral grain next in order of abundance is feldspar which varies in modal proportions from practically nil to about 3%. The grain size variation is from 0.09 to 1 mm and the grains are mostly sub angular and coated with hematite. They are usually altered and show all stages from nearly fresh to almost completely, seriticized in which few fresh relics are present. The feldspar is dominantly detrital

(1) Sample No.	(2) Quartz	(3) Illite-clay matrix.	(4) Silica cement	(5) Hemati-te Cement	(6) Cal-cite Cement	(7) Rock frag-ments	(8) Chert	(9) Felds-pars	(10) Chlorite and Musco-vite	(11) Authi-genic constituents.
1	72.06	13.52	5.84	6.05	-	0.52	1.99	-	-	-
2	67.79	15.37	7.26	7.47	-	0.26	1.42	tr	0.10	0.33
3	69.05	2.84	8.35	15.09	-	1.53	2.37	-	0.76	-
4	70.18	11.89	13.4	1.92	-	-	0.42	2.17	-	-
5	63.16	16.61	7.37	8.44	-	0.66	3.82	-	-	-
6	70.51	13.56	6.12	7.5	-	1.67	0.63	-	-	-
7	70.49	15.04	7.77	5	-	0.49	1.18	-	-	-
8	71.92	8.44	16.43	1.64	-	0.25	1.29	-	-	-
9	60.63	19.86	12.14	5.26	-	-	1	1.10	-	
10	82.31	9.04	5.39	1.61	-	0.05	1.58	-	-	-
11	63.72	19.95	7.91	5.72	-	1.76	0.93	-	-	-
12	71.93	10.53	7.53	5.42	-	1.00	1.61	2.55	-	0.42
13	69.43	1.00	3.98	11.10	12.43	0.56	1.46	-	-	0.04
14	62.03	22.57	5.36	8.19	-	1.84	-	-	-	
15	65.81	0.50	1.25	5.98	23.08	0.02	1.60	1.14	0.27	0.32
16	67.43	5.04	5.16	20.46	-	-	0.39	1.23	tr	0.28
17	65.43	15.73	5.96	10.59	-	0.23	0.26	tr	1.25	0.52
18	69.68	17.37	8.54	2.25	-	0.64	1.17	-	-	0.33
19	63.71	15.28	6.12	11.34	-	0.62	1.39	0.52	0.60	0.40
20	70.90	tr	6.00	17.36	-	3.48	1.76	-	-	0.50
21	68.37	tr	3.5	24.84	-	2.00	1.28	-	-	
22	72.59	6.86	19.5	tr	-	1.00	0.04	-	-	
23	72.33	8.97	11.91	1.62	-	3.50	0.18	1.00	tr	-
24	61.14	19.62	5.72	10.73	-	1.9	0.58	0.25	-	0.2
25	67.44	15.00	7.42	5.47	-	3.32	1.34	-	-	-
26	78.05	tr	7.50	14.45	-	0.63	0.36	-	-	-
27	81.30	2.63	7.01	2.53	-	0.64	4.57	0.40	0.45	0.44
28	52.31	46.85	-	-	-	tr	0.83	-	-	-
29	48.77	40.04	tr	9.00	-	2.19	-	tr	-	-
30	79.11	3.53	7.65	1.08	-	6.52	2.08	-	-	-
31	82.56	12.50	3.98	0.37	-	0.57	-	-	-	-
32	68.24	2.82	7.61	18.84	-	0.65	0.8	0.44	0.27	0.3
33	79.87	0.76	6.79	10.41	-	0.49	1.67	-	-	-
34	70.19	18.39	9.0	1.0	-	-	1.41	-	-	-
35	67.46	1.5	7.5	18.11	-	3.0	2.46	-	-	-
36	67.11	17.37	12.5	-	-	1.01	2.0	-	-	-
37	71.93	tr	15.5	10.45	-	1.9	0.21	-	-	
38	50.94	46.67	-	0.38	-	0.25	0.75	-	1.0	-
39	70.43	23.73	5.5	-	-	-	0.33	-	-	
40	72.94	10.99	11.55	tr	-	2.51	2.00	-	-	
41	63.56	1.0	10.5	19.04	-	2.4	3.48	-	-	
42	63.65	tr	4.0	30.75	-	1.43	0.17	-	-	-
43	79.64	4.94	15.0	tr	-	-	0.42	-	-	
44	68.64	24.56	4.5	tr	-	0.44	1.85	-	-	-
45	73.9	16.91	2.5	2.0	-	1.65	3.0	-	-	-
46	78.31	1.0	10.5	7.73	-	0.9	1.0	-	-	
47	72.94	4.13	9.5	10.0	-	1.41	1.82	-	-	-
48	79.48	1.0	14.5	1.37	-	2.5	1.10	-	-	-
49	60.59	-	tr	35.68	-	2.38	1.12	0.22	-	
50	73.94	2.74	14.5	2.16	-	3.21	2.25	1.19	-	-
51	70.45	3.23	14.65	4.0	-	3.23	2.92	1.52	-	-

52	71.11	3.03	23.5	-	-	1.0	1.35	-	-	tr
53	71.31	1.0	5.65	16.75	-	3.0	1.81	-	-	tr
54	77.28	1.78	18.5	-	-	1.0	1.43	-	-	tr

Table 1. Modal analysis of the Kolhan Sandstones

and includes sodic plagioclase, perthite, microcline and untwinned varieties. Patchy zoning is rare. Microfaulting and bending of the twin lamellae are other features rarely observed in thin sections. Such detrital feldspars show evidence of having been replaced by the slightly recrystallized illite-clay matrix in the rock. In other cases all stages of replacement by muscovite along cleavages are also observed. Authigenic overgrowths on detrital plagioclase are extremely rare.

Turbidity in some detrital feldspar grains appears to be due to a swarm of minute vacuoles. Authigenic feldspars are usually angular, small in size, absolutely fresh and show perfect twin lamellae.

Rock fragments – The clastic constituents which form the rock fragments vary in modal analysis from trace amount to 3.5 % and exhibit a size variation of 0.18 mm to 2 mm. They are mostly sub-angular and include in order of abundance the following: micro-granite, meta-quartzite, shale and phyllite, jasper and banded hematite jasper, quartz schist and angular sandstone.

Sample Nos	Sand size fraction		Silt Clay Fraction		Total Bulk Sample	
	SiO_2%	Al_2O_3%	SiO_2%	Al_2O_3%	SiO_2%	Al_2O_3%
10	63.80	13.80	69.20	9.20	68.52	9.64
11	66.50	13.80	69.20	13.20	68.70	12.96
12	63.39	15.15	78.40	10.20	73.52	11.31
13	55.60	14.20	42.39	13.22	43.33	13.25
16	66.50	12.20	67.40	15.10	66.92	16.09
19	72.28	10.96	67.20	12.64	43.35	
20	66.50	10.50	60.22	27.02	68.71	

Table 2: Partial chemical analysis of the Kolhan Shale

Geochemistry

The results of a of seven specimens of represented in Table 2 which also contains the partial analyses of sand size as well as silt clay size particles separated from the same samples. The SiO_2 content in the five samples of the shale analyzed varies from 43.33% to 73.52%. Silicification is indicated by the high percentage of silica. The Al_2O_3 content varies between 9.64 to 16.09%. The colour of the wet sediment signifies presence of iron rich mineralsX-ray diffraction studies result shows as follows. The preliminary X-ray investigation of the (<2 microns) of a revealed the presence of and certain mixed layer clay minerals while that of quartz (clay-size). The high alumina content of the silt clay fraction is in agreement with the results of X-ray analysis.

Conclusion

Sediment eroded from these sources typically consist of the sand, feldspar with high ratios of potash feldspar to plagioclase feldspar, metamorphic and sedimentary rock fragments. Sediment eroded from continental sources may be transported off the continent into adjacent marginal ocean basins, or it may be deposited in local basins within the continent. The main shallow elongated basin of the Kolhan Formation extends from Chaibasa (85° 48', 22° 33') to Noamundi (85°28', 22° 09') covering about in width along the western extremity of the Singhbhum Granite. The occurrence of detached outliers of the Kolhan rocks east of the unconformity on Singhbhum Granite and north of Chiabasa suggests the wide extent of the Kolhan basin in the past. High Al_2O_3/SiO_2 and K_2O/Na_2O ratios reflect a derivation of all the sediments from stable cratons during tectonic quiescences. These alumina ratio indicates that the clastics were deposited in a passive margin or cratonic margin. There was no glaciation during the existence of the Kolhan Basin.

Reference

Bandopadhyay, P.C., Sengupta, S. 2004. Paleoproterozoic supracrustal Kolhan Group in Singhbhum craton, India and the Indo-African Supercontinent. Gondwana Research. 7(4) 1228-1235.

Bhattacharyya, K. and Das,S. 2015. Sanstone Petrography and Geochemistry of the Kolhan basin, eastern India: Implication for Basin Tectonics. Geology and Geosciences.4 (2) 1-6.

Bhattacharyya,K. and Das, S. 2016. Shale Geochemistry from Kolhan Basin: Tectonic implication. International Journal of Scientific Research 5(8) 629-631.

Bhattacharyya, K. 2017. Clues for the age of Kolhan Basin: tectonic implications. Global Journal of Technology and Optimization, 8(1) 1-4.

Bhattacharyya, K.2017b.Implications of Kolhan Basin:constraints from microscopy. Nature Conference on Electron Microscopy.China. 27-29 May 2017.

Chatterjee, BK Bhattacharya, AK. 1969. Tectonics and sedimentation in a Precambrian shallow intracratonic basin.Journal Sedimentary Petrology.39 (4) 1566-1572.

Das,S. and Bhattacharyya, K. 2013. Evolutionary History Vis-a Vis Depositional Architecture of the Proterozoic Kolhan basin….a discussion. Journal Indian Association of Sedimentologists.32 (1and2) 59-63.

Dickinson, W.R. and Sucrek,R.A. 1979. Plate tectonics and sandstone compositions. Bull. Amer. Assoc. Petrol. Geol. 63 2163-2182.

Dickinson, W.R 1985. Interpretating provenance relation from detrital modes of sandstone. In GG Zuffa Ed. Provenance of Arenites. Dordretch. D Reidal.333-363.

Dunn, J.A., 1940. The Stratigraphy of South Singhbhum: Mem. Geol. Surv. India. 63(3) 303-369

Grant M. Young. 2013. Precambrian Supercontinent, glaciations,atmospheric oxygenation,metazoan evolution and an impact that may have changed the second half of Earth history. Geoscience Frontiers.247-261.

Kent R.1991. Lithospheric uplift in eastern Gondwana: evidence for a long-lived mantle plume system? Geology.19 19 – 23.

Roy A, Sarkar A, Jeyakumar S, Aggrawal SK, Ebihara M.2002. Mid-Proterozoic Plume-related thermal event in Eastern Indian Craton: evidence from trace elements, REE geochemistry and Sr–Nd isotope systematics of basic–ultrabasic intrusives from Dalma Volcanic Belt. Gondwana Research.5 133– 46.

Saha, A. K. 1994. Crustal evolution of Singhbhum-North Orissa. Eastern India. Memoir Geological Society of India. 27-338